

Generation of Gravitational Radiation in Dusty Plasmas and Supernovae[¶]

G. Brodin^{1,2}, M. Marklund^{1,2}, and P. K. Shukla^{1,2,3}

¹ Department of Physics, Umeå University, SE-901 87 Umeå, Sweden

² Centre for Fundamental Physics, Rutherford Appleton Laboratory, Chilton Didcot, Oxfordshire,
OX11 0QX, United Kingdom

³ Institut für Theoretische Physik IV, Fakultät für Physik und Astronomie, Ruhr-Universität Bochum,
D-44780 Bochum, Germany

Received December 22, 2004; in final form, January 24, 2005

We present a novel nonlinear mechanism for exciting a gravitational radiation pulse (or a gravitational wave) by dust magnetohydrodynamic (DMHD) waves in dusty astrophysical plasmas. We derive the relevant equations governing the dynamics of nonlinearly coupled DMHD waves and a gravitational wave (GW). The system of equations is used to investigate the generation of a GW by compressional Alfvén waves in a type II supernova. The growth rate of our nonlinear process is estimated, and the results are discussed in the context of the gravitational radiation accompanying supernova explosions. © 2005 Pleiades Publishing, Inc.

PACS numbers: 04.30.Db, 97.60.Bw, 98.62.En

It is well known that there exist numerous mechanisms for the conversion between gravitational waves (GWs) and electromagnetic waves [1–19]. For example, the propagation of GWs across an external magnetic field gives rise to a linear coupling to the electromagnetic field [1], which may lead to the gravitational wave excitation of ordinary electromagnetic waves in vacuum, or of magnetohydrodynamic (MHD) waves in a plasma [2–4]. Furthermore, various nonlinear coupling mechanisms give rise to three-wave couplings between GWs and electromagnetic waves in matters. We also note that four-wave processes may cause graviton–photon conversion even in the absence of external matters or fields [5]. Moreover, GWs can couple to other types of waves, e.g., sound waves, also in neutral media [6]. There are numerous motives for considering wave couplings involving GWs. In some cases, the emphasis is on the basic theory [5–10]. In other works, the focus is on GW detectors [11–13], on cosmology [14–16], or on astrophysical applications such as binary mergers [17], gamma-ray bursts [18], or pulsars [19]. Here, supernovae and neutron star formation, giving rise to GWs as considered in, e.g., [20, 21], will be of special interest, since the possibility of dust formation in supernova remnants is of current astrophysical interest [22, 23]. Many of the previous works have concentrated on the conversion from GWs to electromagnetic waves, which can be analyzed within a test matter approach, which neglects the back reaction on the gravitational field. We note that such an approach can be justified if the background energy density is low.

In this letter, we consider the three-wave coupling between two dust magnetohydrodynamic (DMHD) waves and a GW, including the effects of dust particles [24] in a dense medium such as the supernova where electrons, protons, and charged dust macroparticles are abundant. For this purpose, we derive the dust Hall MHD equations [24], i.e., equations describing the dust MHD waves, including the effect of a GW. We emphasize that, for a low-beta plasma, the system of equations has a structure, which can describe both a dust-dominated plasma, as well as an ordinary Hall-MHD plasma (if we replace the dust mass density by the ion mass density). Using the normal mode approach [25], the three-wave coupling equations are derived, including the back reaction on a GW from the Einstein equations. The system is shown to fulfill the Manley–Rowe relations [25] (which means that the interaction process can be viewed quantum-mechanically) and to be energy-conserving. The three-wave equations are then used to analyze the generation of a GW by the compressional Alfvén waves in the iron core of the type II supernova [26, 27]. It turns out that the characteristic timescale for the Alfvén–GW conversion can be less than a millisecond, which implies that the mechanism is potentially relevant for the high-frequency part (>1 MHz) of the supernova GW spectrum.

The plasma dynamics, due to the response to a gravitational wave

$$ds^2 = -dt^2 + (1 + h_+)dx^2 + (1 - h_+)dy^2 + 2h_\times dx dy + dz^2 \quad (1)$$

[¶]This article was submitted by the authors in English.

can be formulated according to

$$\partial_t n_s + \nabla \cdot (n_s \mathbf{v}_s) = 0, \quad (2)$$

and

$$\begin{aligned} & m_s n_s (\partial_t + \mathbf{v} \cdot \nabla) \mathbf{v} \\ &= -\nabla p_s + q_s n_s (\mathbf{E} + \mathbf{v} \times \mathbf{B}) + m_s n_s \mathbf{g}_s, \end{aligned} \quad (3)$$

where we have introduced the tetrad $\mathbf{e}_0 = \partial_t$, $\mathbf{e}_1 = (1 - h_+/2)\partial_x - h_\times/2\partial_y$, $\mathbf{e}_2 = (1 + h_+/2)\partial_y - h_\times/2\partial_x$, $\mathbf{e}_3 = \partial_z$, and $\nabla = (\mathbf{e}_1, \mathbf{e}_2, \mathbf{e}_3)$. Moreover,

$$\begin{aligned} \mathbf{g}_s &= -\frac{1}{2}(1 - v_{sz})(v_{sx}\partial_t h_+ + v_{sy}\partial_t h_\times)\mathbf{e}_1 \\ &\quad - \frac{1}{2}(1 - v_{sz})(v_{sx}\partial_t h_\times - v_{sy}\partial_t h_+)\mathbf{e}_2 \\ &\quad - \frac{1}{2}[(v_{sx}^2 - v_{sy}^2)\partial_t h_+ + 2v_{sx}v_{sy}\partial_t h_\times]\mathbf{e}_3, \end{aligned} \quad (4)$$

represents the gravitational acceleration of the particle species s due to the GWs. We have assumed that $\partial_z \approx -\partial_t$ holds for the GWs.

The electromagnetic field is determined through the gravity-modified Maxwell's equations. Using the same notation as above, they take the form

$$\partial_t \mathbf{E} = \nabla \times \mathbf{B} - \sum_s q_s n_s \mathbf{v}_s - \mathbf{j}_E, \quad (5)$$

$$\partial_t \mathbf{B} = -\nabla \times \mathbf{E} - \mathbf{j}_B, \quad (6)$$

with the constraints $\nabla \cdot \mathbf{E} = \sum_s q_s n_s$ and $\nabla \cdot \mathbf{B} = 0$. Here, the effects of the GWs (1) are represented by the effective currents

$$\begin{aligned} \mathbf{j}_E &= -\frac{1}{2}[(E_x - B_y)\partial_t h_+ + (E_y + B_x)\partial_t h_\times]\mathbf{e}_1 \\ &\quad - \frac{1}{2}[-(E_y + B_x)\partial_t h_+ - (E_x - B_y)\partial_t h_\times]\mathbf{e}_2, \end{aligned} \quad (7)$$

and

$$\begin{aligned} \mathbf{j}_B &= -\frac{1}{2}[(E_y + B_x)\partial_t h_+ - (E_x - B_y)\partial_t h_\times]\mathbf{e}_1 \\ &\quad - \frac{1}{2}[(E_x - B_y)\partial_t h_+ + (E_y + B_x)\partial_t h_\times]\mathbf{e}_2. \end{aligned} \quad (8)$$

With the general setting established above, we will from now on focus on the case of a three-component dusty plasma, for which we have the equation of state $p_s = k_B T_s n_s$. Thus, the plasma is composed of electrons (e), ions (i), and dust particles (d). The mass m_d of the dust particles is assumed to be much larger than the electron and ion masses, viz. m_e and m_i , respectively. We will assume that the plasma is approximately quasineutral, i.e., $q_i n_i = en_e - q_d n_d$. Moreover, the waves under consideration are supposed to propagate with phase velocities much smaller than the speed of light c .

Thus, we may neglect the displacement current in Ampere's law (5), i.e.,

$$\nabla \times \mathbf{B} = \sum_s q_s n_s \mathbf{v}_s + \mathbf{j}_E. \quad (9)$$

Due to the constraint $m_e, m_i \ll m_d$, the momentum conservation equation (3) for the inertialess electrons and ions becomes

$$0 = -k_B T_e \nabla n_e - en_e (\mathbf{E} + \mathbf{v}_e \times \mathbf{B}) + m_e n_e \mathbf{g}_e, \quad (10)$$

and

$$0 = -k_B T_i \nabla n_i + q_i n_i (\mathbf{E} + \mathbf{v}_i \times \mathbf{B}) + m_i n_i \mathbf{g}_i, \quad (11)$$

respectively. Adding Eqs. (10) and (11), using the quasineutrality condition, assuming that the number densities of the electrons and ions are not much larger than the number density of the dust, and using the heavy dust approximation, the dust momentum equation takes the form

$$\begin{aligned} \rho_d (\partial_t + \mathbf{v}_d \cdot \nabla) \mathbf{v}_d &= -k_B \left(T_d - \frac{q_d}{q_i} T_i \right) \nabla n_d \\ &\quad + (\nabla \times \mathbf{B}) \times \mathbf{B} - \mathbf{j}_E \times \mathbf{B} + \rho_d \mathbf{g}_d \end{aligned} \quad (12)$$

where $\rho_d = m_d n_d$. In Eq. (12), we have also used the approximation $[T_e + (e/q_i)T_i]n_e \ll [T_d - (q_d/q_i)T_i]n_d$.

Again, using Eqs. (10) and (11) to eliminate the electric field, Faraday's law (6) becomes

$$\begin{aligned} \partial_t \mathbf{B} &= \nabla \times (\mathbf{v}_d \times \mathbf{B}) \\ &\quad - \frac{m_d}{q_d} \nabla \times [(\partial_t + \mathbf{v}_d \cdot \nabla) \mathbf{v}_d - \mathbf{g}_d] - \mathbf{j}_B, \end{aligned} \quad (13)$$

where we have used the dust momentum equation (12).

Thus, Eqs. (12) and (13), together with the dust continuity equation

$$\partial_t \rho_d + \nabla \cdot (\rho_d \mathbf{v}_d) = 0, \quad (14)$$

constitute the dust MHD equations in the presence of a GW. For a low-beta plasma, the pressure term in (12) is negligible, which means that the structure of equations (12)–(14) is the same as in an ordinary Hall-MHD plasma without dust. Henceforth, we will consider a low-beta plasma, drop the index d on all quantities, and, thus, let q/m be either the ion charge-to-mass ratio or the considerably smaller charge-to-mass ratio of the dust particles. As a result, our mathematical analysis below will then apply either to a dust Hall-MHD plasma, or to an ordinary Hall-MHD plasma without dust.

To simplify the problem, we consider the case when the dust-acoustic speed $c_s = k_B T/m$ is much smaller than the dust Alfvén velocity $C_A = (B_0^2/\mu_0 \rho)^{1/2}$ such that the pressure term in (12) can be neglected. As a prerequisite for the nonlinear calculations, we first study the linear modes of the system (12)–(14) omitting the gravita-

tional contributions. Letting $B = B_0 \hat{\mathbf{z}} + \mathbf{B}_1$, $\rho = \rho_0 + \rho_1$, where the index 1 denotes the perturbation of the equilibrium part, and linearizing Eqs. (12)–(14) and Fourier analyzing, we readily obtain the dispersion relation

$$(\omega^2 - k_z^2 C_A^2)(\omega^2 - k^2 C_A^2) - \frac{\omega^2 k_z^2 k^2 C_A^2}{\omega_c^2} = 0, \quad (15)$$

where $\omega_c = qB_0/m$ is the gyrofrequency. For frequencies much smaller than the gyrofrequency, we note that the modes separate into the shear Alfvén wave, $\omega^2 - k_z^2 C_A^2 \approx 0$, and the compressional Alfvén wave, $\omega^2 - k^2 C_A^2 \approx 0$. Below, we will consider the more general case described by (15), however. For later applications, it is convenient to use the linear equations to express all quantities in terms of a single variable. Thus, we let the wavevector of the dust MHD waves lie in the x - z -plane, and write

$$v_y = i \frac{\omega}{\omega_c} \frac{k_z^2 C_A^2}{(\omega^2 - k_z^2 C_A^2)} v_x, \quad (16)$$

$$v_z = 0, \quad \rho_1 = \rho_0 \frac{k_x v_x}{\omega},$$

$$B_x = -B_0 \frac{\omega k_z}{k^2 C_A^2} v_x, \quad (17)$$

$$B_y = -i B_0 \frac{\omega^2}{\omega_c (\omega^2 - k_z^2 C_A^2)} \frac{k_z}{k_x} v_x, \quad (18)$$

$$B_z = B_0 \frac{\omega k_x}{k^2 C_A^2} v_x. \quad (19)$$

Next, we consider a system of three weakly interacting waves. Two dust MHD waves with frequencies and wavenumbers (ω_1, \mathbf{k}_1) and (ω_2, \mathbf{k}_2) , respectively, and an arbitrarily polarized gravitational wave propagating along the z -direction with the frequency and wavenumber $(\omega_g, k_g \hat{\mathbf{z}})$. Noting that the gravitational dispersion relation reads $\omega_g = k_g c$ and that $C_A \ll c$, the frequency and wavenumber matchings (energy and momentum conservation) can be approximated:

$$\omega_g = \omega_1 + \omega_2, \quad \mathbf{k}_g = \mathbf{k}_1 + \mathbf{k}_2 \Rightarrow 0 \approx \mathbf{k}_1 + \mathbf{k}_2. \quad (20)$$

We will thus use $\mathbf{k}_1 \approx -\mathbf{k}_2$ below, and we define $k_{1x} = -k_{2x} \equiv k_x$ as well as $k_{1z} = -k_{2z} \equiv k_z$ (letting $k_y = 0$ for convenience). All quantities are now assumed to be superpositions of two dust MHD waves whose amplitudes are weakly varying functions of time, i.e., $\rho = \rho_0 + \sum_{j=1}^2 \rho_j(t) \exp[i(\mathbf{k}_j \cdot \mathbf{r} - \omega \mathbf{t})] + \text{c.c.}$, where c.c. stands for the complex conjugate. In principle, the gravitational wave should also contribute, but we note that, within a fluid model, the gravitational wave contribution to all plasma perturbations (velocity, magnetic

field, and density) are second-order in the gravitational wave amplitudes, provided that the GW propagates parallel to \mathbf{B}_0 , as we have assumed. Thus, the only linear perturbations due to the gravitational wave are those of the metric as described by Eq. (1).

Next, in order to simplify the algebra, we introduce the normal mode a_j defined by

$$a_j = \frac{\omega_j}{k_{xj}} v_{xj} - i \frac{\omega_j^2 k_{zj}^2 C_A^2}{\omega_c (\omega_j^2 - k_{zj}^2 C_A^2) k_{xj}} v_{yj} - \frac{\omega_j^2 k_{zj} C_A^2}{k_j^2 k_{xj} B_0} B_{xj} + \frac{\omega_j^2 k_{zj}^2 C_A^2}{\omega_c^2 (\omega_j^2 - k_{zj}^2 C_A^2) B_0} C_A^2 B_{zj} + i \frac{(\omega_j^2 - k_{zj}^2 C_A^2) \omega_c^2 - k_j^2 C_A^2 \omega_j^2}{k_j^2 \omega_j} \frac{k_{zj}}{\omega_c k_{xj} B_0} B_{yj}. \quad (21)$$

Returning to Eqs. (12)–(14) and including the nonlinear terms,¹ we can, by keeping the part varying as $\exp[i(\mathbf{k}_1 \cdot \mathbf{r} - \omega_1 \mathbf{t})]$, derive

$$\begin{aligned} \frac{\partial a_1}{\partial t} = & -\frac{\omega_1}{2k_x} (v_{2x}^* h_+ + v_{2y}^* h_x) \\ & - i \frac{\omega_1^2 k_z^2 C_A^2 (v_{2x}^* h_x - v_{2y}^* h_+)}{2\omega_c (\omega_1^2 - k_z^2 C_A^2) k_x} \\ & - \frac{\omega_1^2}{2k^2 k_x B_0} (B_{2x}^* h_+ - B_{2y}^* h_x) \\ & + i \frac{k_z [(\omega_1^2 - k^2 C_A^2) \omega_c^2 - k^2 C_A^2 \omega_1^2]}{k^2 \omega_1 \omega_c k_x B_0} \\ & \times (B_{2x}^* h_x - B_{2y}^* h_+), \end{aligned} \quad (22)$$

and we obtain a similar result for $\partial a_2 / \partial t$ by letting $1 \leftrightarrow 2$. After some algebra, using Eqs. (16)–(19) and (21), we find that Eq. (22) reduces to

$$\frac{d v_{x1}}{dt} = \frac{\rho_0 \omega_1}{W_1} v_{x2}^* (V_+ h_+ + V_x h_x), \quad (23)$$

and similarly, for mode 2,

$$\frac{d v_{x2}}{dt} = \frac{\rho_0 \omega_2}{W_2} v_{x1}^* (V_+ h_+ + V_x h_x), \quad (24)$$

¹ When including the nonlinear GW-coupling, it is, in principle, important to separate the coordinate components (indices x, y, z) from the tetrad components (indices 1, 2, 3), since the difference is first order in h_+, h_x . However, for notational convenience, we let indices x, y, z denote tetrad components 1, 2, 3 in equation (22) and henceforth.

where

$$W_{1,2} = \frac{\rho_0}{2} \left[1 + \frac{\omega_{1,2}^2}{k_{1,2}^2 C_A^2} + \frac{\omega_{1,2}^2 k_{z1,2}^4 C_A^2}{\omega_c^2 (\omega_{1,2}^2 - k_{z1,2}^2 C_A^2)^2} \left(1 + \frac{\omega_{1,2}^2}{k_{z1,2}^2 C_A^2} \right) \right], \quad (25)$$

$$V_{\times} = i \left[\frac{\omega_1 k_z^2 C_A^2 k^2 - \omega_2 \omega_1 k_z^2}{\omega_c (\omega_1^2 - k_{z1}^2 C_A^2) k^2} + 1 \leftrightarrow 2 \right], \quad (26)$$

and

$$V_{+} = i \left[1 + \frac{\omega_1 \omega_2}{\omega_c^2} \frac{k_z^2 C_A^2 (k_z^2 C_A^2 + \omega_1 \omega_2)}{(\omega_1^2 - k_z^2 C_A^2)(\omega_2^2 - k_z^2 C_A^2)} + \frac{\omega_1 \omega_2 k_z^2}{k^4 C_A^2} \right]. \quad (27)$$

Next, using the Einstein equations, linearized in h_{+} , h_{\times} , keeping only the resonantly varying part of $T^{\mu\nu}$, we obtain for the \times - and $+$ -polarization, respectively,

$$i\omega_g \frac{dh_{\times}}{dt} = \kappa \left[\rho_0 v_{x1} v_{y2} + \frac{B_{x2} B_{y1}}{\mu_0} \right], \quad (28)$$

and

$$i\omega_g \frac{dh_{+}}{dt} = \frac{\kappa}{2} \left[\rho_0 (v_{x1} v_{x2} - v_{y1} v_{y2}) + \frac{B_{x1} B_{x2} - B_{y1} B_{y2}}{\mu_0} \right], \quad (29)$$

which is reduced to

$$\frac{dh_{\times}}{dt} = -\frac{\rho_0 \omega_g}{W_g} V_{\times} v_{x1} v_{x2}, \quad (30)$$

and

$$\frac{dh_{+}}{dt} = -\frac{\rho_0 \omega_g}{W_g} V_{+} v_{x1} v_{x2}, \quad (31)$$

where $W_g = \omega_g^2 / 2\kappa$. The total wave energy is $W_{\text{tot}} = W_1 |v_{x1}|^2 + W_2 |v_{x2}|^2 + W_g (|h_{\times}|^2 + |h_{+}|^2)$, and it is easily verified from (23), (24) together with (30), (31) that W_{tot} is conserved. Furthermore, the appearance of the same coupling coefficients V_{\times} , V_{+} in Eqs. (23), (24) as well as in (30), (31) assures that the Manley–Rowe relations are fulfilled, which implies that each mode changes energy in direct proportion to its frequency, i.e., $(dW_1/dt)/(dW_2/dt) = \omega_1/\omega_2$, etc. The system of (23), (24) together with (30), (31) describing the energy conversion between DMHD waves and GWs is one of the main results of the present letter. A more elaborate cal-

culational scheme, including effects such as inhomogeneity and background curvature, is a project for future research.

We now apply our results to the gravitational radiation arising from the iron core of a type II supernova where the densities can be of the order 10^{17} kg/m³ [27]. The large neutrino outflow (which can reach powers of 10^{33} W/cm²; see, e.g., [26]) can generate MHD waves described by (15). From the flux conservation, we expect the iron core to be strongly magnetized (comparable to pulsars), and for magnetic field strengths $B_0 \sim 10^8$ T, the gyrofrequency will be much larger than all other frequencies of the problem. The dispersion relation then separate into the shear Alfvén waves $\omega^2 - k_z^2 C_A^2 \approx 0$ and the compressional Alfvén waves $\omega^2 - k^2 C_A^2 \approx 0$. Assuming that the pump MHD wave is a compressional mode with a frequency 5 MHz, the matching conditions (20) can be fulfilled for a GW with a typical frequency 3 MHz and a shear Alfvén wave with the frequency 2 MHz.² For the assumed geometry, the MHD waves couple only to the h_{\times} -polarization (to a good approximation), and by combining (24) and (30), we obtain

$$\frac{d^2 h_{\times}}{dt^2} = -h_{\times} \frac{\omega_2 |V_{\times}|^2 16\pi G}{\omega_g W_2 c^2} \rho_0 |v_{x1}|^2. \quad (32)$$

Thus, noting that the factor $\omega_2 |V_{\times}|^2 / \omega_g W_2$ is negative² and has a magnitude of order unity³ for the given parameters, the growth rate is

$$\gamma \sim \sqrt{16\pi G \rho_0} \frac{|v_{x1}|}{c}, \quad (33)$$

which, for a weakly relativistic pump quiver speed, $|v_{x1}|/c \sim 1/10$, implies $\gamma \sim 10$ kHz. Thus, we deduce that excitation of a GW by MHD waves is a reasonably fast process in a dense medium such as the supernova iron core. It would be of interest to quantitatively estimate the energy that can be converted to GWs through this process. Clearly, the growth rate is fast enough, such that the time available for conversion is not a limiting factor. However, eventually the MHD wave source will be depleted, which give an upper limit for the energy available through this mechanism. How large fraction

² Note that, from the Manley–Rowe relations, the pump wave must have the highest frequency for the growth rates to become real and positive. Thus, using the matching condition (20), we see that the shear Alfvén mode formally has a negative frequency. Furthermore, we note that the dispersion relations, together with the matching conditions, means that the pump mode cannot propagate purely along the magnetic field. Specifically, the wavevector matching implies $k_x C_A \approx 4.6$ MHz, where $C_A \approx 300$ m/s for the given parameters.

³ This can be seen by taking the limit $\omega_c \rightarrow \infty$ of the expression, noting that $(\omega_2^2 - k_{z2}^2 C_A^2)$ scales as $1/\omega_c^2$ from the dispersion relation (15).

of the MHD wave source that can be converted to GWs depend on the influence from competing processes, for example, excitation of other MHD waves by the MHD pump wave and/or wave particle interaction. Thus, further research is necessary before a definite estimate of the GW energy levels due to the present mechanism can be given. However, we emphasize that the present process can give rise to GWs of higher frequencies than many of the previously considered excitation mechanisms (see, e.g., [20, 21, 28]). Thus, our model contributes to the understanding of gravitational radiation emissions accompanying supernova explosions [29].

REFERENCES

1. L. P. Grishchuk and A. G. Polnarev, *General Relativity and Gravitation*, Ed. by A. Held (Plenum, New York, 1980), Vol. 2, p. 416.
2. D. Papadopoulos *et al.*, *Astron. Astrophys.* **377**, 701 (2001).
3. J. Moortgat and J. Kuijpers, *Astron. Astrophys.* **402**, 905 (2003).
4. J. Moortgat and J. Kuijpers, *Phys. Rev. D* **70**, 023001 (2004).
5. A. Källberg, G. Brodin, and M. Marklund, gr-qc/0410005 (2004).
6. A. M. Anile, J. K. Hunter, and B. Turong, *J. Math. Phys.* **40**, 4474 (1999).
7. M. Servin and G. Brodin, *Phys. Rev. D* **68**, 044017 (2003).
8. M. Servin, M. Marklund, G. Brodin, *et al.*, *Phys. Rev. D* **67**, 087501 (2003).
9. J. T. Mendonça, *Plasma Phys. Controlled Fusion* **44**, B225 (2002).
10. A. B. Balakin, V. R. Kurbanova, and W. Zimdahl, *J. Math. Phys.* **44**, 5120 (2003).
11. F. Y. Li and M. X. Tang, *Int. J. Mod. Phys. D* **11**, 1049 (2002).
12. G. Brodin and M. Marklund, *Class. Quantum Grav.* **20**, 45 (2003).
13. R. Ballantini, Ph. Bernard, E. Chiaveri, *et al.*, *Class. Quantum Grav.* **20**, 3505 (2003).
14. D. Papadopoulos, *Class Quantum Grav.* **19**, 2939 (2002).
15. M. Marklund, P. K. Dunsby, and G. Brodin, *Phys. Rev. D* **62**, 101501 (2000).
16. P. A. Hogan and E. M. O'Shea, *Phys. Rev. D* **65**, 124017 (2002).
17. G. Brodin, M. Marklund, and M. Servin, *Phys. Rev. D* **63**, 124003 (2001).
18. L. Vlahos, G. Voyatzis, and D. Papadopoulos, *Astrophys. J.* **604**, 297 (2004).
19. H. J. M. Cuesta, *Phys. Rev. D* **65**, 64009 (2002).
20. O. A. Kuznetsov, M. E. Prokhorov, M. V. Sazhin, *et al.*, *Astron. Rep.* **42**, 638 (1998).
21. M. V. Sazhin, S. D. Ustyugov, and V. M. Chechetkin, *JETP* **86**, 629 (1998).
22. L. Dunne, S. Eales, R. Ivison, *et al.*, *Nature* **424**, 285 (2003).
23. O. Krause, S. M. Birkmann, G. H. Rieke, *et al.*, *Nature* **432**, 596 (2004).
24. P. K. Shukla and A. A. Mamun, *Introduction to Dusty Plasma Physics* (Inst. of Physics, Bristol, 2002).
25. J. Weiland and H. Wilhelmsson, *Coherent Nonlinear Interaction of Waves in Plasmas* (Pergamon, New York, 1977; Énergoizdat, Moscow, 1981).
26. G. G. Raffelt, *Stars as Laboratories for Fundamental Physics* (Univ. of Chicago Press, Chicago, 1996).
27. S. E. Woosley, A. Heger, and T. A. Weaver, *Rev. Mod. Phys.* **74**, 1015 (2002).
28. C. Cutler and K. Thorne, in *Proceedings of the 16th International Conference on General Relativity and Gravitation, Durban, South Africa, 2001*, Ed. by N. T. Bishop and S. D. Maharaj (World Sci., Singapore, 2002).
29. M. V. Sazhin, S. D. Ustyugov, and V. M. Chechetkin, *JETP Lett.* **64**, 871 (1996).

Cross Sections for the Production of Stable and Unstable Isotopes with Charge Numbers from One to Eight in $^{16}\text{O}p$ Collisions at 3.25 A GeV/c

É. Kh. Bazarov¹, V. V. Glagolev², V. V. Lugovoy¹, S. L. Lutpullaev¹, K. Olimov¹, V. I. Petrov¹,
A. A. Yuldashev¹, and B. S. Yuldashev³

¹ Institute for Physics and Technology, “Fizika–Solntse” Research and Production Association, Uzbek Academy of Sciences, ul. G. Mavlyanova 2b, Tashkent, 700084 Republic of Uzbekistan

e-mail: olimov@uzsci.net

² Joint Institute for Nuclear Research, Dubna, Moscow region, 141980 Russia

³ Institute of Nuclear Physics, Uzbek Academy of Sciences, pos. Ulughbek, Tashkent, 702132 Republic of Uzbekistan

Received January 12, 2005

New experimental data are presented for the inclusive cross sections both for the production and for the yield of stable and unstable isotopes with charge numbers from one to eight in $^{16}\text{O}p$ collisions at 3.25 A GeV/c. © 2005 Pleiades Publishing, Inc.

PACS numbers: 25.10.+s

The identification of mechanisms of the fragmentation of nuclei interacting with hadrons and nuclei is a fundamental problem of high energy physics. According to experimental data, nuclear fragments make the basic contribution to the multiplicity of secondary particles in hadron–nucleus collisions at several GeVs per nucleon. Although this phenomenon has been studied in a number of experimental works, there is no information about such important characteristics of nuclear fragmentation processes as cross sections for the yield of all nuclear fragments, particularly unstable, observed in experiments.

The aim of this work is to determine the inclusive cross sections for the production of stable and unstable nuclei with charge numbers $Z_f = 1–3$ and cross sections for the yield of stable and unstable nuclei with charge numbers $Z_f = 4–8$ in $^{16}\text{O}p$ collisions at 3.25 A GeV/c.

We use the experimental data consisting of 13 479 $^{16}\text{O}p$ events detected on a 1-m bubble chamber (Laboratory of High Energies, Joint Institute for Nuclear Research) irradiated by ^{16}O nuclei with a momentum of 3.25 A GeV/c at the Dubna synchrophasotron. Procedure problems concerning the reconstruction of the kinematic characteristics of secondary particles and fragments, as well as their identification according to charge and mass, were previously discussed in [1–3].

Stable isotopes, fragments with the charge Z_f , were separated as in [1] by analyzing the distributions over the variable $x = 1/p$, where p is the laboratory momentum of a fragment. We selected fragments with the measured length $L \geq 35$ cm for $Z_f = 1$ and 2 and $L > 40$ cm for $Z_f = 3–8$.

The procedure for determining the production cross sections for stable isotopes with the charge number Z_f consists of the following stages.

(i) The x spectrum of fragments with the charge number Z_f is approximated by the following sum of Gaussians:

$$f_{Z_f}(x_k) = \sum_{i=1}^n a_i \exp(-(x_k - 1/A_i p_o)^2 / 2\sigma_i^2).$$

Here, n is the total number of the experimentally observed isotopes with the charge number Z_f , A_i is the mass number of the i th isotope, x_k is the x value at the k th experimental point, $p_o = 3.25$ GeV/c is the initial momentum per nucleon, and a_i and σ_i are the approximation parameters that make it possible to determine the contribution from each isotope to the x spectrum of fragments.

(ii) The fraction α_i of the i th isotope with the charge number Z_f is determined as the ratio

$$\alpha_i(Z_f) = \frac{\sum_{k=1}^m a_i \exp(-(x_k - 1/A_i p_o)^2 / 2\sigma_i^2)}{\sum_{k=1}^m \sum_{i=1}^n a_i \exp(-(x_k - 1/A_i p_o)^2 / 2\sigma_i^2)},$$

where m is the number of experimental points in the x spectrum of fragments with the charge number Z_f .

(iii) The production cross section for the i th isotope with the charge number Z_f is calculated as

$$\sigma_i(Z_f) = \alpha_i(Z_f) \langle n(Z_f) \rangle \sigma_{\text{in}}(^{16}\text{Op}),$$

where the average multiplicity $\langle n(Z_f) \rangle$ of fragments with the charge number Z_f for $Z_f \geq 2$ is taken from [4], the average multiplicity of single-charged fragments is determined as the ratio of the total number of positive single-charged particles with momenta above 1.75 GeV/c to the total number of inelastic ^{16}Op events, and $\sigma_{\text{in}}(^{16}\text{Op})$ is the inelastic cross section for ^{16}Op collisions [5], which is equal to 334 ± 6 mb for a momentum of 3.25 A GeV/c.

By definition, $\sigma_i(Z_f)$ is the inclusive cross section for the production of the i th isotope with the charge number Z_f . However, since no event with two or more isotopes with $Z_f \geq 4$ has been observed in the experiment, the cross section obtained for such isotopes can be considered as their yield cross sections.

The production cross section for unstable $^5\text{Li}_3$ nuclei was determined [6] by analyzing the effective-mass spectra of the α particle and proton, as well as by analyzing the angles between the proton momentum and the momenta of the α particles produced in ^{16}Op collisions at 3.25 A GeV/c. Both values turned out to be the same within the statistical errors: $\sigma(^5\text{Li}_3) = 8.4 \pm 0.5$ mb. As we showed in [3], the cross sections for the production of light mirror nuclei $^3\text{H}_1$ and $^3\text{He}_2$, as well as $^7\text{Li}_3$ and $^7\text{Be}_4$, coincide with each other within the statistical errors. For this reason, the cross sections for the production of the mirror nuclei $^5\text{He}_2$ and $^5\text{Li}_3$ are expected to be identical.

Using the phenomenological model of isotropic phase space and analyzing the experimental spectrum of effective masses, we obtained a value of $\sigma(^{12}\text{C}^*) = (9.8 \pm 0.9)$ mb for the cross sections for the production of excited $^{12}\text{C}^*$ nuclei in the channel of the production of three α particles in ^{16}Op collisions at 3.25 GeV/c [7]. The direct decay channel $^{12}\text{C}^* \rightarrow 3\alpha$ and the channel $^{12}\text{C}^* \rightarrow ^8\text{Be}_4 + \alpha \rightarrow 3\alpha$ provide 40 and 60% of this cross section, respectively.

Analyzing azimuthal correlations in the channels of the production of three and four α particles in ^{16}Op collisions at 3.25 GeV/c in the framework of the phenomenological model of isotropic phase space [8], we determined the contributions $W(^8\text{Be}_4) = (22.0 \pm 1.1)\%$ and $W(^9\text{B}_5) = (19.0 \pm 1.0)\%$ of the unstable nuclei $^8\text{Be}_4$ and $^9\text{B}_5$ to these channels. Using the total cross section (21.68 ± 0.87) mb for the production of three and four α particles, we obtain $\sigma(^8\text{Be}_4) = (4.80 \pm 0.31)$ mb and $\sigma(^9\text{B}_5) = (4.12 \pm 0.27)$ mb for the cross sections for the yield of these unstable nuclei. In the framework of a similar model, analyzing the scattering angle $\vartheta_{\alpha\alpha}$ between a pair of α particles in the channel of the pro-

Cross sections for the production of stable and unstable isotopes in ^{16}Op collisions at 3.25 A GeV/c

Z	A	$\sigma \pm \Delta\sigma$, mb	Z	A	$\sigma \pm \Delta\sigma$, mb
1	$^1\text{H}_1$	509.0 ± 5.7	5	$^9\text{B}_5^*$	5.70 ± 0.29
	$^2\text{H}_1$	116.9 ± 1.3		$^{10}\text{B}_5$	10.6 ± 0.4
	$^3\text{H}_1$	41.8 ± 0.4		$^{11}\text{B}_5$	10.9 ± 0.4
2	$^3\text{He}_2$	40.7 ± 1.9	6	$^{12}\text{B}_5$	0.51 ± 0.42
	$^4\text{He}_2$	164.0 ± 1.9		$^{10}\text{C}_6$	1.77 ± 0.8
	$^5\text{He}_2^*$	8.40 ± 0.50		$^{11}\text{C}_6$	9.18 ± 0.76
	$^6\text{He}_2$	1.03 ± 0.23		$^{12}\text{C}_6$	26.3 ± 0.8
3	$^5\text{Li}_3^*$	8.40 ± 0.50	7	$^{12}\text{C}_6^*$	9.80 ± 0.80
	$^6\text{Li}_3$	19.0 ± 0.8		$^{13}\text{C}_6$	9.48 ± 0.76
	$^7\text{Li}_3$	10.6 ± 0.8		$^{14}\text{C}_6$	3.68 ± 0.76
	$^8\text{Li}_3$	4.80 ± 0.76		$^{13}\text{N}_7$	9.40 ± 0.79
4	$^7\text{Be}_4$	10.3 ± 0.5	8	$^{14}\text{N}_7$	26.1 ± 0.8
	$^8\text{Be}_4^*$	7.63 ± 0.37		$^{15}\text{N}_7$	30.3 ± 0.8
	$^9\text{Be}_4$	6.15 ± 0.52		$^{14}\text{O}_8$	2.85 ± 0.7
	$^{10}\text{Be}_4$	0.89 ± 0.52		$^{15}\text{O}_8$	31.1 ± 0.7
				$^{16}\text{O}_8$	13.0 ± 0.7

* Unstable or excited states.

duction of two α particles in the same collisions, we determined the contributions $W(^8\text{Be}_4) = (9.7 \pm 0.5)\%$ and $W(^9\text{B}_5) = (5.4 \pm 0.3)\%$ of the unstable nuclei $^8\text{Be}_4$ and $^9\text{B}_5$ to this channel. Using the cross section (29.17 ± 1.51) mb for the channel of the production of two α particles, we obtain $\sigma(^8\text{Be}_4) = (2.83 \pm 0.20)$ mb and $\sigma(^9\text{B}_5) = (1.58 \pm 0.11)$ mb for the cross sections for the yield of these unstable nuclei.

Thus, the total cross sections for the yields of the unstable nuclei $^8\text{Be}_4$ and $^9\text{B}_5$ in ^{16}Op collisions at 3.25 GeV/c are equal to $\sigma(^8\text{Be}_4) = (7.63 \pm 0.37)$ mb and $\sigma(^9\text{B}_5) = (5.70 \pm 0.29)$ mb, respectively.

The results of the above procedures, along with the data on cross sections for the production of unstable nuclei, are given in the table. The table shows that

(i) α particles are produced with the largest inclusive cross section among multicharged fragments;

(ii) cross sections for the production of mirror nuclei with mass numbers differing by $\Delta A = \pm 1$ from the main mass number defined as $A = 2Z$ coincide with each other within statistical errors. Note that cross sections for the yield of the unstable isotope ^9B and the stable mirror isotope ^9Be also coincide with each other within statistical errors. It is remarkable that this rule also concerns the mirror nuclei ^{15}N and ^{15}O formed due to the

loss of one nucleon by the initial nucleus ^{16}O in peripheral collisions with a target proton.

REFERENCES

1. V. V. Glagolev, K. G. Gulamov, M. Yu. Kratenko, *et al.*, Pis'ma Zh. Éksp. Teor. Fiz. **58**, 497 (1993) [JETP Lett. **58**, 497 (1993)].
2. V. V. Glagolev, K. G. Gulamov, M. Yu. Kratenko, *et al.*, Yad. Fiz. **58**, 2005 (1995) [Phys. At. Nucl. **58**, 1896 (1995)].
3. V. V. Glagolev, K. G. Gulamov, M. Yu. Kratenko, *et al.*, Pis'ma Zh. Éksp. Teor. Fiz. **59**, 316 (1994) [JETP Lett. **59**, 336 (1994)].
4. A. S. Botvina, A. Sh. Gaitinov, V. V. Glagolev, *et al.*, Z. Phys. A **345**, 413 (1993).
5. V. V. Glagolev, K. G. Gulamov, V. D. Lipin, *et al.*, Eur. Phys. J. A **11**, 285 (2001).
6. K. G. Gulamov, S. L. Lutpullaev, V. D. Lipin, *et al.*, Ukr. Fiz. Zh., No. 5, 35 (2000).
7. É. Kh. Bazarov, V. V. Glagolev, K. G. Gulamov, *et al.*, Phys. At. Nucl. **67**, 2183 (2004).
8. É. Kh. Bazarov, V. V. Glagolev, K. G. Gulamov, *et al.*, Yad. Fiz. **67**, 2297 (2004) [Phys. At. Nucl. **67**, 2272 (2004)].

Translated by R. Tyapaev

Novel Probe of the Vacuum of the Lattice Gluodynamics[¶]

M. I. Polikarpov¹, S. N. Syritsyn¹, and V. I. Zakharov²

¹ Institute of Theoretical and Experimental Physics, Moscow, 117259 Russia

² Max-Planck Institut für Physik, 80805 Munich, Germany

Received January 17, 2005

We introduce the notion of a minimal number of negative links on the lattice for a given original configuration of $SU(2)$ fields. Negative links correspond to a large potential, not necessarily to large action. The idea is that the minimal number of negative links is a gauge invariant notion. To verify this hypothesis, we measure the correlator of two negative links, averaged over all the directions, as a function of the distance between the links. The inverse correlation length coincides within the error bars with the lightest glueball mass. © 2005 Pleiades Publishing, Inc.

PACS numbers: 11.15.-q, 11.15.Ha, 12.38.Gc

A traditional way to study spectrum of excitations is to measure correlators of various sources. For example, the correlator,¹

$$D_{gl}(r) \equiv \langle 0 | (G_{\mu\nu}^a(r))^2, (G_{\alpha\beta}^a(0))^2 | 0 \rangle, \quad (1)$$

where $G_{\mu\nu}^a$ is the gluonic field strength tensor, is sensitive to the glueball mass m_{gl} at large (Euclidean) distances r :

$$\lim_{r \rightarrow \infty} D_{gl}(r) = \text{const} + (\text{const})' \exp(-m_{gl}r). \quad (2)$$

On the other hand, one can also study gauge dependent correlators, such as

$$D_{\mu\nu}^{a,b}(r) = \langle 0 | A_{\mu}^a(r), A_{\nu}^b(0) | 0 \rangle, \quad (3)$$

where A_{μ}^a is the gauge field. Such correlators are not unitary, generally speaking, and are not controlled by glueball masses. In particular, gluon propagator (3) could even grow at large r . More realistically, i.e., as indicated by the lattice measurements, the gluon propagator falls off at large r but exhibits some spurious mass scales; for a review, see, e.g., [1, 2]. For us, it is important that these spurious mass scales are, as a rule, lower than the lightest glueball mass.

In this note, we introduce a new type of correlators that, we hypothesize, might be unitary although they are not explicitly gauge invariant (like (1)) and check our hypothesis through lattice simulations of $SU(2)$ gluodynamics.

To explain the basic idea behind our measurements, it is useful first to remind to the reader of how one can introduce a gauge invariant condensate of dimension

two in gauge theories [3]. One starts with the vacuum expectation value $\langle (A_{\mu}^a)^2 \rangle$, which is obviously gauge dependent. One can, however, minimize this vacuum expectation value on the gauge orbits, and the results $\langle (A_{\mu}^a)^2 \rangle_{\min}$ are gauge invariant by construction. To ensure that the minimum exists, a Euclidean signature is used.²

We generalize this idea to the case of a $Z(2)$ projection of the original $SU(2)$ fields. In this projection, the link variables take values ± 1 (for a review, see, e.g., [5]). Upon the $Z(2)$ projection, a $Z(2)$ gauge invariance remains. We fix this gauge freedom by minimizing the number of negative links over the whole lattice. We speculate, furthermore, that the density of these negative links might well be gauge invariant, by analogy with $\langle (A_{\mu}^a)^2 \rangle_{\min}$.

Moreover, we expect that the correlator of the negative links is unitary, like (1). This speculation goes, apparently, beyond the ideas discussed so far. Indeed, the negative links in the continuum limit correspond to singular potentials, $A_{\mu}^a \sim 1/a$, where a is the lattice spacing. One could naively argue that the correlator of such strong fields dies off in distances of order a . In particular, this is true for pure perturbative fluctuations.

This argument might not work, but only if there exist fine tuned vacuum fluctuations that are sensitive both to the lattice spacing and Λ_{QCD} . Although the idea of the existence of fine tuned fluctuations may look too exotic at first sight, such fluctuations do exist. In particular, the so-called P -vortices are closed surfaces whose total area scales in the physical units; for a review, see, e.g., [5]. On the other hand, the P -vortices are defined

[¶] This article was submitted by the authors in English.

¹ For simplicity of notations, we do not take into account the anomalous dimension.

² A modification suitable for the Minkowski space is to work in the Hamiltonian formalism [4].

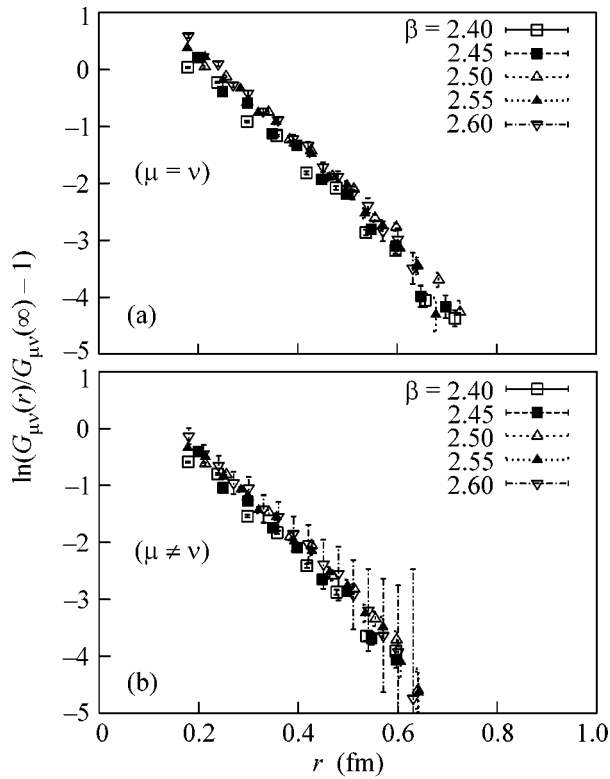


Fig. 1. $\ln\left(\frac{G_{\mu\nu}(r)}{G_{\mu\nu}(\infty)} - 1\right)$ vs. lattice spacing for (a) $\mu = \nu$ and for (b) $\mu \neq \nu$, results obtained for IMCP.

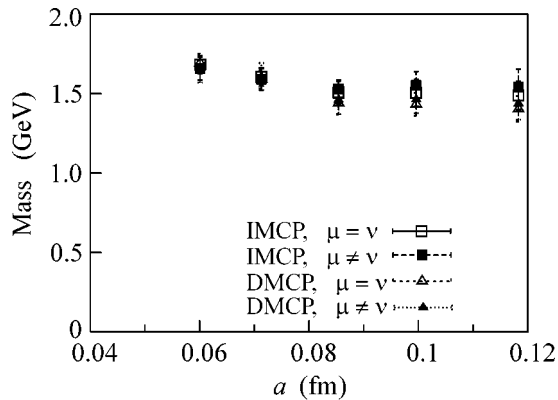


Fig. 2. Mass parameters for IMCP and DMCP for $\mu = \nu$ and for $\mu \neq \nu$.

as a unification of all the negative plaquettes in the $Z(2)$ projection. One can expect, therefore, that they are associated with an action density that is ultraviolet divergent. And, indeed, the fact that the P -vortices are associated with the ultraviolet divergent non-Abelian action was revealed directly through lattice measurements [6]. It is by analogy with these observations that

we expect the “propagator of negative links” to scale in physical units as well. This is, of course, a daring possibility that cannot be proven a priori but can be only supported or rejected by measurements.

We perform measurements in greater detail both in direct and indirect maximal center projections (DMCPs and IMCPs). The details of these calculations are given in the Appendix. As a result of $SU(2) \rightarrow Z(2)$ projection, the original $SU(2)$ field configurations are projected into the closest configuration of $Z(2)$ gauge fields. The remaining $Z(2)$ gauge freedom is then fixed by maximizing the functional

$$F(Z) = \sum_{x, \mu} Z_{x, \mu} \quad (4)$$

with respect to $Z(2)$ gauge transformations ($Z_{x, \mu} \rightarrow z_x Z_{x, \mu} z_{x+\hat{\mu}}, z_x = \pm 1$).

After gauge fixing, only the positions of the negative links are relevant and it is reasonable to change the variables:

$$\hat{Z}_{x, \mu} = \{1, \text{ if } Z_{x, \mu} = -1; 0 \text{ if } Z_{x, \mu} = 1\}. \quad (5)$$

Moreover, to imitate a scalar correlator on the discrete variables, we consider here the isotropic correlator defined as

$$G_{\mu\nu}(r) \equiv \frac{1}{N_r} \sum_{r < |x| < r + \frac{a}{2}} \langle \hat{Z}_{0\mu} \hat{Z}_{x,\nu} \rangle, \quad (6)$$

where the summation is over all links $Z_{x, \mu}$ for x lying in the spherical layer $r < |x| < r + \frac{a}{2}$ and N_r is the total number of links in this layer.

Correlator (6) tends to a nonvanishing constant $G(\infty) = \langle \hat{Z}_{x, \nu} \rangle^2$ as $r \rightarrow \infty$ ($\langle \hat{Z}_{x, \nu} \rangle$ is the average density of the negative links), and we fit the data by the expression (see (2)):

$$G(r) = G(\infty) + C \exp\{-mr\}. \quad (7)$$

We thus get mass parameter m for various values of lattice spacing a . Logarithmic plots for the isotropic correlator $G(r)$ are presented in Fig. 1 for IMCPs, while the corresponding values of mass m are depicted in Fig. 2 for IMCPs and DMCPs.

As is seen from Figs. 1 and 2, the correlator $G_{\mu\nu}(r)$ scales in physical units (within the error bars) and the mass parameter is close to the scalar 0^{++} glueball mass ($m(0^{++}) = 1.65 \pm 0.05$ GeV [7]). Thus, our measurements support the idea that correlator (6) is in fact gauge invariant and unitary. Of course, the results are not analytical but pure numerical and, in principle, the picture can change at smaller values of the lattice spacing. The nontriviality of this observation is that it is a correlator of potentials that are not explicitly gauge invariant. Moreover, in the continuum limit, the nega-

tive links correspond to singular potentials. The scaling of the correlation length observed here gives further support to the existence of fine-tuned vacuum fluctuations.

We would like to thank V.G. Bornyakov and G. Greensite for very useful discussions. The work of M.I.P. and S.N.S. was supported in part by the Russian Foundation for Basic Research (RFBR, project nos. 02-02-17308 and 01-02-17456), Deutsche Forschungsgemeinschaft (joint grant no. 436 RUS 113/739/0 with RFBR), INTAS (grant no. 00-00111), and U.S. Civilian Research and Development Foundation for the Independent States of the Former Soviet Union (grant no. RPI-2364-MO-02). The work of V.I.Z. was supported in part by the INTAS (grant no. 00-00111).

APPENDIX

We perform our calculations both in direct [8] and the indirect [9] maximal center projections (DMCPs and IMCPs). The DMCP in $SU(2)$ lattice gauge theory is defined by the maximization of the functional

$$F_1(U) = \sum_{x,\mu} (\text{Tr} U_{x,\mu})^2, \quad (8)$$

with respect to gauge transformations; $U_{x,\mu}$ is the lattice gauge field. Maximization of (8) fixes the gauge up to $Z(2)$ gauge transformations, and the corresponding $Z(2)$ gauge field is defined as $Z_{x,\mu} = \text{sgnTr} U_{x,\mu}$. To get the IMCP, we first fix the maximally Abelian gauge maximizing the functional

$$F_2(U) = \sum_{x,\mu} \text{Tr}(U_{x,\mu} \sigma_3 U_{x,\mu}^+ \sigma_3), \quad (9)$$

with respect to gauge transformations. We project gauge degrees of freedom $U(1) \rightarrow Z(2)$ by a procedure completely analogous to the DMCP case, that is, we maximize $F_1(U)$ (8) with respect to $U(1)$ gauge transformations.

To fix the maximally Abelian and direct maximal center gauge, we create 20 randomly gauge transformed copies of the gauge field configuration and apply a simulated annealing algorithm to fix the

Parameters of configurations

β	Size	N_{IMCP}	N_{DMCP}
2.35	16^4	20	20
2.40	24^4	50	20
2.45	24^4	20	20
2.50	24^4	50	20
2.55	28^4	37	17
2.60	28^4	50	20

gauges. In the calculations, we used that copy that corresponded to the maximal value of the gauge fixing functional. To fix the indirect maximal center gauge from a configuration fixed to a maximally Abelian gauge and to fix $Z(2)$ degrees of freedom, one gauge copy is enough to work with our accuracy. We work at various lattice spacings to check the existence of the continuum limit. The parameters of our gauge field configurations are listed in the table. To fix the physical scale, we use string tension in lattice units [10], $\sqrt{\sigma} = 440 \text{ MeV}$.

REFERENCES

1. C. Michael and M. Teper, Nucl. Phys. B **305**, 453 (1988).
2. R. Alkofer and L. von Smekal, Phys. Rep. **353**, 281 (2001).
3. F. V. Gubarev, L. Stodolsky, and V. I. Zakharov, Phys. Rev. Lett. **86**, 2220 (2001).
4. L. Stodolsky, P. van Ball, and V. I. Zakharov, Phys. Lett. B **552**, 214 (2003).
5. J. Greensite, Prog. Part. Nucl. Phys. **51**, 1 (2003).
6. F. V. Gubarev, A. V. Kovalenko, M. I. Polikarpov, *et al.*, Phys. Lett. B **574**, 136 (2003).
7. M. J. Teper, hep-th/9812187.
8. L. Del Debbio, M. Faber, J. Giedt, *et al.*, Phys. Rev. D **58**, 094501 (1998).
9. L. Del Debbio, M. Faber, J. Greensite, and S. Olejnik, Phys. Rev. D **55**, 2298 (1997).
10. J. Fingberg, U. M. Heller, and F. Karsch, Nucl. Phys. B **392**, 493 (1993).

Screening of the Dust-Particle Charge in a Plasma with an External Ionization Source

A. V. Filippov^{1,*}, A. G. Zagorodny², A. F. Pal'¹, and A. N. Starostin¹

¹ Troitsk Institute for Innovation and Fusion Research, Troitsk, Moscow region, 142190 Russia

* e-mail: fav@triniti.ru

² Bogolyubov Institute for Theoretical Physics, National Academy of Sciences of Ukraine, Kiev, 03143 Ukraine

Received December 27, 2004; in final form, January 20, 2005

An asymptotic theory of the screening of the dust-particle charge in a plasma with an external ionization source has been developed. It has been shown analytically that the screening of the charge of a dust particle adsorbing the charge of charged plasma particles that fall on it is not generally described by the Debye theory. The screening radius is determined by the relation between the coefficients β_{ei} and $\beta_L = 4\pi ek_i$ (k_i is the ion mobility) of the electron–ion and Langevin recombinations, respectively. When $\beta_L \gg \beta_{ei}$, the screening radius is much larger than the electron Debye radius. It has been shown that the contribution of the ion component of an isothermal plasma to screening is equal to the electron contribution if the coefficient of the electron–ion recombination is twice or more larger than the Langevin coefficient of the ion recombination, $\beta_{ei} \geq 2\beta_L$. © 2005 Pleiades Publishing, Inc.

PACS numbers: 52.27.Lw

INTRODUCTION

Dusty-plasma physics is a rapidly developing field of science. The problem of the interaction force between dust particles is an important and complicated problem in dusty-plasma physics. This problem is closely connected with the problem of the screening character for a dust-particle charge, which is incompletely solved in the physics of an ordinary low-temperature plasma [1]. The Debye character of screening the dust-particle charge is assumed in almost all the current models that have been developed in dusty-plasma physics (see, e.g., reviews [2, 3]). There is no commonly accepted point of view on the role of the ion component in field screening. The screening radius is an important parameter determining the conditions of the crystallization of the Debye plasma [2], ion drag force (see [4] and the further discussion in [5, 6]), the spectrum of the dusty plasma waves [2], etc.

In this work, the formation and screening of the charge of an isolated dust particle in a plasma with an external source of gas ionization are considered in the hydrodynamic regime of the transport of electrons and ions. Investigation of the dusty plasma at high pressures, where the gas is ionized by the external source and the ionization by plasma electrons is negligibly small, attracts great interest (see [2, 7–12]). For this reason, we analyze here dusty plasma with a constant rate of gas ionization by an external source such as a beam of fast electrons or protons in non-self-sustained discharges or laser radiation in a photoresonant plasma.

ASYMPTOTIC SCREENING THEORY

Let a dust particle be located at the origin of the coordinate system and the ionization compensating for the loss of the plasma due to the absorption of plasma particles by the dust particle be uniform and constant in time and space. In the drift–diffusion approximation, the steady state of the plasma is described by the equations

$$\nabla \Gamma_\sigma = Q_{\text{ion}} - \beta_{ei} n_e n_i, \quad \sigma = e, i. \quad (1)$$

Here

$$\Gamma_\sigma = - \left\{ \frac{e_\sigma n_\sigma}{m_\sigma \nu_\sigma} \nabla \phi + D_\sigma \nabla n_\sigma \right\}, \quad (2)$$

where ν_σ is the collision frequency; D_σ is the diffusion coefficient; ϕ is the self-consistent field potential; $e_\sigma = e$ and $-e$, where e is the elementary charge, for $\sigma = i$ and e , respectively; Q_{ion} is the intensity of the bulk ionization by the external source; and β_{ei} is the recombination coefficient. We are interested in the asymptotic behavior of the effective potential for $r \gg a$ when all the coefficients in Eqs. (1) and (2) can be considered as being independent of coordinates and the self ionization of atoms by plasma electrons is assumed to be negligibly small compared to Q_{ion} . Note that the charge and, correspondingly, the electric field of the dust particle are formed by electrons. Therefore, according to thermodynamic concepts, the field of the dust particle cannot heat the electron component and lead to a noticeable change in the coefficients of the transport, ionization,

and recombination of electrons [8]. This means that the self ionization of the plasma is possible only in an external electric field whose magnitude in discharges with the external ionization source is insufficient for an noticeable ionization of the gas.

Since the effective potential decreases with increasing distance, Eqs. (1) and (2) can be linearized beginning with a certain radius R_L . Assuming that $\nabla\Gamma_\sigma = 0$ in the absence of any dust particle, we obtain

$$n_{0e,i} = \sqrt{Q_{\text{ion}}/\beta_{ei}}. \quad (3)$$

After linearization, Eqs. (1) take the form

$$-\frac{e_\sigma n_0}{m_\sigma \nu_\sigma} \Delta\phi - D_\sigma \Delta\delta n_\sigma = -\beta_{ei} n_0 (\delta n_e + \delta n_i), \quad (4)$$

where $n_0 \equiv n_{0e,i}$ and $\delta n_\sigma \equiv \delta n_\sigma(r)$ is the deviation of the density of the σ th type of particles due to the absorption of the plasma by the dust particle.

In terms of these quantities, the Poisson equation has the form

$$\Delta\phi = -4\pi\delta\rho = -4\pi \sum_\sigma e_\sigma \delta n_\sigma. \quad (5)$$

Dividing Eq. (4) by D_σ , summing over the types of particles, and taking into account Eq. (5) and the Einstein relations $D_\sigma = T_\sigma/m_\sigma \nu_\sigma$, we arrive at the following equation for the total density $\sum_\sigma \delta n_\sigma \equiv \delta n_+$:

$$\Delta\delta n_+ - k_s^2 \delta n_+ = k_D^2 \delta n_-, \quad (6)$$

where $k_s^2 = \sum_\sigma \beta_{ei} n_0 / D_\sigma$, $k_D^2 = k_{Di}^2 - k_{De}^2$, $k_{D\sigma}^2 = 4\pi e_\sigma^2 n_0 / T_\sigma$, and $\delta n_- = \delta n_i - \delta n_e$.

Dividing Eq. (4) by D_σ , multiplying by e_σ , and summing over the types of particles, we obtain

$$\Delta\delta n_- - k_D^2 \delta n_- = k_s^2 \delta n_+, \quad (7)$$

where $k_D^2 = k_{De}^2 + k_{Di}^2$, $k_s^2 = k_{si}^2 - k_{se}^2$, and $k_{s\sigma}^2 = \beta_{ei} n_0 / D_\sigma$. For a nonisothermal plasma, from Eqs. (6) and (7) we obtain

$$(\Delta - k_1^2)(\Delta - k_2^2)\delta n_- = 0, \quad (8)$$

where

$$k_{1,2}^2 = \frac{1}{2} \left[(k_D^2 + k_s^2) \pm \sqrt{(k_D^2 - k_s^2)^2 + 4k_D^2 k_s^2} \right]. \quad (9)$$

Since $\delta n_{e,i}(\infty) = 0$, it follows from Eq. (8) that

$$\delta n_- = \frac{A}{r} e^{-k_1 r} + \frac{B}{r} e^{-k_2 r}, \quad (10)$$

where A and B are arbitrary constants that are not determined in the framework of this approach. The integra-

tion of Poisson equation (5) after the substitution of Eq. (10) into it yields

$$\phi = \frac{A_1}{r} e^{-k_1 r} + \frac{B_1}{r} e^{-k_2 r}, \quad (11)$$

where $A_1 = -4\pi e A / k_1^2$ and $B_1 = -4\pi e B / k_2^2$. According to Eq. (11), the potential created by the dust particle in the case under consideration is described, in contrast to the Debye theory, by the superposition of two exponentials with different screening constants k_1 and k_2 . It follows from Eq. (11) that

$$E = -\frac{A_1}{r^2} (1 + k_1 r) e^{-k_1 r} - \frac{B_1}{r^2} (1 + k_2 r) e^{-k_2 r}. \quad (12)$$

At large distances, screening is determined by the smaller constant k_2 corresponding to the minus sign in Eq. (9). In the plasma, D_e is always much larger than D_i . Therefore,

$$k_s^2 \approx \frac{\beta_{ei} n_0}{D_i} = \frac{\beta_{ei}}{\beta_L} k_{Di}^2, \quad k_s^2 \approx k_s^2, \quad (13)$$

where $\beta_L = 4\pi e k_i$ is the Langevin ion recombination coefficient. Since $\beta_L \gg \beta_{ei}$ for most ions at atmospheric pressure, $k_s^2 \ll k_D^2$. In this case for $T_e \gg T_i$, it follows from Eq. (9) that the screening radius in the nonisothermal plasma is given by the expression

$$\lambda_2 = \lambda_{De} \sqrt{\frac{\beta_L}{2\beta_{ei}}}. \quad (14)$$

This means that, when $\beta_L \gg \beta_{ei}$, the screening radius is much larger than the electron Debye radius, which was noted in our previous works [7–11] devoted to numerical simulations. In [9], where the character of the screening of a dust-particle charge was studied for a constant-density plasma, it was shown that the screening was exponential and the screening radius decreased with increasing the electron–ion recombination coefficient, which was in complete agreement with Eq. (14). Note that, if the three-particle recombination of electrons and ions with an electron as the third body must be taken into account in the processes of electron losses, the sum $\beta_{ei} + 2\beta_3 n_{0e}$ rather than β_{ei} enters into all the expressions and Eq. (14) takes the form

$$\lambda_2 = \lambda_{De} \sqrt{\frac{\beta_L}{2(\beta_{ei} + 2\beta_3 n_{0e})}}. \quad (15)$$

Expression (14) can be represented in the form

$$\lambda_2 = \sqrt{D_a \tau_{\text{rec}}}. \quad (16)$$

According to this relation, the screening radius up to a constant factor is determined by the characteristic length of the ambipolar diffusion of ions with the coefficient $D_a = D_i(1 + T_e/T_i)$ for the characteristic recombination time $\tau_{\text{rec}} = (2\beta_{ei} n_{e0})^{-1}$. Up to a constant factor,

expression (16) coincides with the estimate [11] of the size of the region of plasma perturbation by the dust particle.

Then, we analyze the case of *isothermal plasma*, $T_e = T_i$. In this case, $k_D^2 = 0$ and the relation between δn_+ and δn_- through Eq. (6) disappears. In this case, it follows from Eq. (6) that

$$\delta n_+ = \frac{A}{r} e^{-k_s r}. \quad (17)$$

When the sink of electrons and ions is absent (e.g., the dust particle does not adsorb electrons and ions), the densities of electrons and ions have Boltzmann distributions and $\delta n_+ = 0$ in the isothermal case. Therefore, $A = 0$ and only Debye terms remain in the below expressions. However, in the nonisothermal plasma, where charged particles are generated by the method under consideration, currents exist even for the nonabsorbing dust particle (Boltzmann distributions for electrons and ions result from the condition that currents (2) vanish; expanding these distributions at large distances and substituting the corresponding expansions into Eq. (4), we see that the right-hand side of Eq. (4) does not vanish when $T_e \neq T_i$).

The solution of Eq. (7) for $k_D \neq k_s$ has the form

$$\delta n_- = \frac{k_s^2 A}{k_s^2 - k_D^2} e^{-k_s r} + \frac{B}{r} e^{-k_D r}. \quad (18)$$

The differences of the densities of ions and electrons from the equilibrium values are expressed as

$$\delta n_i = \frac{1}{2} \frac{k_s^2 + k_s^2 - k_D^2 A}{(k_s^2 - k_D^2) r} e^{-k_s r} + \frac{1}{2} \frac{B}{r} e^{-k_D r}, \quad (19)$$

$$\delta n_e = \frac{1}{2} \frac{k_s^2 - k_s^2 - k_D^2 A}{(k_s^2 - k_D^2) r} e^{-k_s r} - \frac{1}{2} \frac{B}{r} e^{-k_D r}. \quad (20)$$

Under the condition

$$k_D^2 = k_s^2 + k_s^2, \quad (21)$$

which is equivalent to the equality

$$\beta_{ei} = \beta_L, \quad (22)$$

it follows from Eq. (19) that

$$\delta n_i \approx 0 \quad (23)$$

at distances $r \gg k_D^{-1}$, although according to Eq. (20), the perturbation of the electron density in this region decreases exponentially:

$$\delta n_e \approx \frac{A}{r} e^{-k_s r}. \quad (24)$$

For the nonisothermal plasma, approximate equality (23) at large distances is valid only under the condition

$$k_D^2 + k_D^2 = k_s^2 + k_s^2, \quad (25)$$

from which Eq. (22) again follows. Using Eq. (18), from the Poisson equation we obtain

$$\phi = -\frac{A_2}{(k_s^2 - k_D^2) r} e^{-k_s r} - \frac{B_2}{r} e^{-k_D r}, \quad (26)$$

where $A_2 = 4\pi e A k_s^2 / k_s^2$ and $B_2 = 4\pi e B / k_D^2$. It follows

from Eq. (26) that, at distances $r \gg k_{\max}^{-1}$, where $k_{\max} = \max\{k_s, k_D\}$, the asymptotic formulas for the potential and electric field have the form

$$\phi \propto \frac{1}{r} e^{-k_{\min} r}; \quad E \propto \frac{1 + k_{\min} r}{r^2} e^{-k_{\min} r}, \quad (27)$$

where $k_{\min} = \min\{k_s, k_D\}$. For $k_s = k_D$, i.e., in the resonance case, the solution of Eq. (7) has the form

$$\delta n_- = \left(-\frac{k_s^2 A}{2k_s} + \frac{B}{r} \right) e^{-k_s r}. \quad (28)$$

In this case, from the Poisson equation we obtain

$$\phi = \left(\frac{A_2}{2k_s} + \left[\frac{A_2}{k_s^2} - B_2 \right] \frac{1}{r} \right) e^{-k_s r}, \quad (29)$$

$$E = \left(\frac{A_2}{2} + \left[\frac{A_2}{k_s^2} - B_2 \right] \frac{1 + k_s r}{r^2} \right) e^{-k_s r}.$$

It is seen that the asymptotic formulas for $k_s = k_D$ have the form of a simple exponential with the Debye screening radius:

$$\phi \propto e^{-k_s r}; \quad E \propto e^{-k_s r}. \quad (30)$$

As was mentioned above, $\beta_L > \beta_{ei}$ for most ions at atmospheric pressure and, therefore, $k_s^2 < k_D^2$. Hence, the screening radius in the isothermal plasma is given by the expression

$$\lambda_s = k_s^{-1} = \lambda_{De} \sqrt{\frac{\beta_L}{\beta_{ei}}}, \quad (31)$$

which differs slightly from Eq. (14). Using Eqs. (14) and (31), one can conclude that, under the condition $\beta_L \gg \beta_{ei}$, ions are not involved in the screening of the dust particle field in both isothermal and nonisothermal plasmas. Under the opposite condition $\beta_L < \beta_{ei}$, a hump appears in the ion distribution (see Fig. 1). Consequently, the diffusion component of the ion current turns against the drift component. For this reason, the ion distribution becomes close to equilibrium and the ion component is involved in screening. Therefore, the screening radius, which is equal to the electron Debye

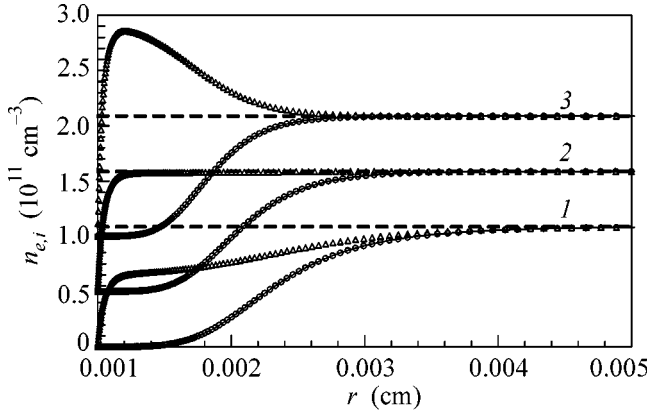


Fig. 1. Distributions of ions and electrons near the dust particle: calculations for (○) electrons and (△) ions, (solid lines) Boltzmann distributions for electrons, (dashed lines) densities of electrons and ions in the unperturbed plasma for the argon atomic density $N = (1) 2.8 \times 10^{19}$, (2) 1.12×10^{20} , and (3) $4.5 \times 10^{20} \text{ cm}^{-3}$. Lines 2 and 3 are shifted upward for a convenient representation.

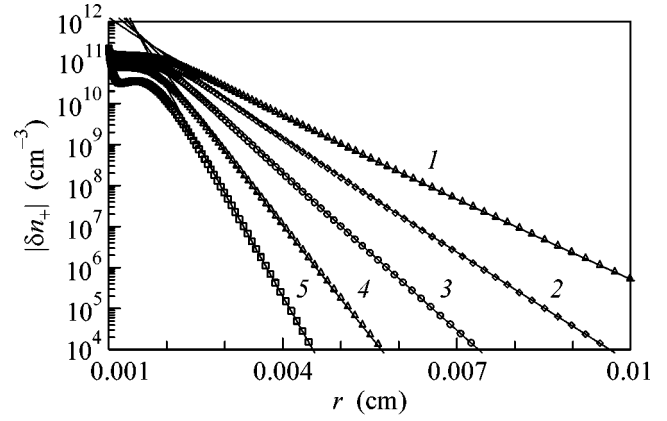


Fig. 2. Distribution of δn_+ near the dust particle: points are calculations and solid lines correspond to distribution (17) for $\beta_L = (1) 4\beta_{ei}$, (2) $2\beta_{ei}$, (3) β_{ei} , (4) $1/2\beta_{ei}$, and (5) $1/4\beta_{ei}$ and $N = (1) 2.8 \times 10^{19}$, (2) 5.6×10^{19} , (3) 1.12×10^{20} , (4) 2.24×10^{20} , and (5) $4.48 \times 10^{20} \text{ cm}^{-3}$.

radius at $\beta_L = \beta_{ei}$ ($k_s = k_D/\sqrt{2}$), becomes equal to the classical Debye radius at $\beta_L \leq \frac{1}{2}\beta_{ei}$ ($k_s \leq k_D$).

COMPARISON OF THE ASYMPTOTIC SCREENING THEORY WITH THE NUMERICAL CALCULATION RESULTS

Figure 1 shows the distributions of ions and electrons near the dust particle for various relations between the coefficients of the electron–ion and Langevin recombinations as obtained by numerically solving the time-dependent continuity equations

$$\partial n_\sigma / \partial t + \text{div} \Gamma_\sigma = Q_{\text{ion}} - \beta_{ei} n_e n_i \quad (32)$$

and the Poisson equation with the boundary conditions

$$\begin{aligned} n_{e,i}|_{r=r_0} = 0, \quad E|_{r=r_0} = eq_{\text{int}}/r_0^2, \\ n_{e,i}|_{r=\infty} = n_0 = \sqrt{Q_{\text{ion}}/\beta_{ei}}, \quad \phi|_{r=\infty} = 0, \end{aligned} \quad (33)$$

where $q_{\text{int}} = 4\pi r_0^2 \int (|\Gamma_i| - |\Gamma_e|) dt$. The calculation procedure was described in more detail in [8]. In test calculations with zero sources of the production and loss of electrons in the calculation cell, the solution with unscreened charge was obtained, which was discussed in detail in [9]. Note that such conditions are possibly realized in a so-called Q machine [13], where the ionization of cesium atoms occurs on the heated walls of a working chamber and the recombination of electrons and atomic ions in volume occurs with a negligibly low rate. Under the same boundary conditions with nonzero parameters Q_{ion} and β_{ei} , the quasi-neutrality of the calculation cell is reconstructed. In this case, the dust-particle charge and distributions of the plasma and electric

field are independent of the form of the boundary condition for the field through the accumulated charge in the above boundary condition or in the form of zero field at the outer boundary. The calculations were performed for argon, ionization rate $Q_{\text{ion}} = 10^{16} \text{ cm}^{-3} \text{ s}^{-1}$, and various pressures with the constant recombination coefficient $\beta_{ei} = 0.85 \times 10^{-6} \text{ cm}^3/\text{s}$ for the parameters $T_e = T_i = 300 \text{ K}$, $r_0 = 10 \text{ } \mu\text{m}$, $n_{e0} = n_{i0} = n_0 = 1.087 \times 10^{11} \text{ cm}^{-3}$, $\lambda_{De} = 3.63 \text{ } \mu\text{m}$, and $\lambda_D = 2.56 \text{ } \mu\text{m}$. The Langevin recombination coefficient was varied by varying pressure.

As is seen in Fig. 1, under condition (22), the ion density remains constant almost to the dust particle when the absorption of ions by the dust particle is manifested. The ion density is constant, because a decrease in the ion loss rate in the process of electron–ion recombination with decreasing the electron density is exactly compensated for by an increase in the Langevin recombination rate. This problem, as well as the condition of the appearance of a peak in the ion distribution and the formation of the ambipolar-diffusion region, was discussed in [8]. This condition coincides with Eq. (22) and is strictly justified here.

Figure 2 shows distribution (17) in comparison with the distribution calculated for δn_+ . It is seen that the calculation results are in an excellent agreement with the asymptotic theory developed above. Figure 3 shows the distribution of the reduced field. It is seen that, beginning with a certain distance, the functions $\Xi(r)$ approach the asymptotic curves parallel to the abscissa axis, as can be expected according to Eqs. (27) and (30).

Figure 4 shows the screening radii obtained in our works [10, 11] (approximating the calculation potential by the standard exponential divided by the radius) in comparison with the values calculated from Eq. (15). It

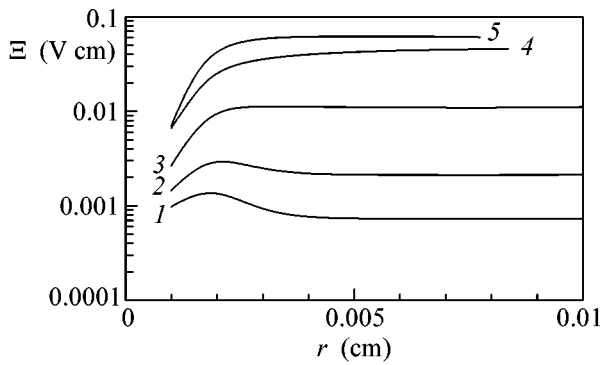


Fig. 3. Distribution of the reduced field (1–3, 5) $\Xi = Er_0^2 \exp(k_{\min}r)(1 + k_{\min}r)^{-1}$ and (4) $\Xi = Er_0^2 \exp(k_{\min}r_0)(1 + k_{\min}r_0)^{-1}$. The calculation parameters are the same as for the respective lines in Fig. 2.

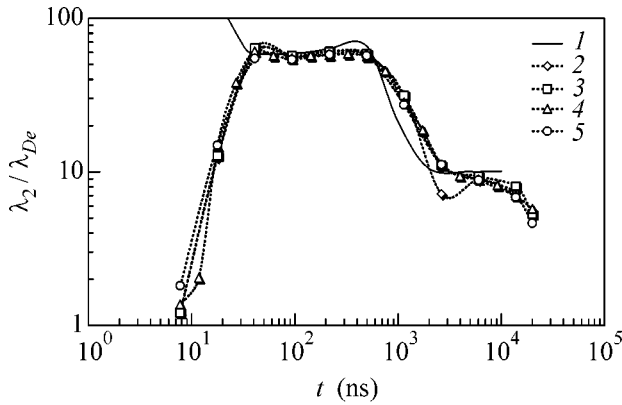


Fig. 4. Screening radius divided by the electron Debye radius (line 1) as calculated from relation (15) in comparison with data published in [11] for the photoresonant plasma for the dust particle radius $r_0 =$ (2) 1, (3) 2, (4) 5, and (5) 10 μm .

is seen that the calculations agree well with the asymptotic theory. A discrepancy at small times appears because the electron density in the photoresonant plasma at the initial time is still low and the screening radius is very large. For this reason, to correctly determine it, calculations would have to be performed with a much larger radius of the calculation cell than that used in [10, 11].

CONCLUSIONS

In this work, using the perturbation method, we have developed the asymptotic theory of the screening of the charge of an isolated dust particle in a plasma with an external source of the ionization of a gas in the hydrodynamic regime of the transport of electrons and ions.

It has been shown that the screening of the charge of the dust particle adsorbing the charged particles of the plasma is not generally described by the Debye theory. The screening radius is determined by the relation between the coefficients of the dissipative and Langevin recombinations. When the latter coefficient is small, the screening radius is much larger even than the electron Debye radius. Thus, the appreciable excess of the screening radius over the Debye radius, which was repeatedly observed in hydrodynamic numerical calculations [7–11], as well as the correlation noted in [9, 11] between the screening radius and the ion recombination coefficient, has been strictly justified.

This work was supported by the Russian Foundation for Basic Research (project nos. 04-02-16883a, 04-02-16775a, 4-02-08085ofl_a), the Council of the President of the Russian Federation for Support of Young Russian Scientists and Leading Scientific Schools (project no. NSh-1257.2003.2), and the Ukrainian State Foundation for Basic Research (project no. 02.7/0049).

REFERENCES

1. Yu. P. Raizer, *Gas Discharge Physics* (Nauka, Moscow, 1987; Springer, Berlin, 1997).
2. V. E. Fortov, A. G. Khrapak, S. A. Khrapak, *et al.*, *Usp. Fiz. Nauk* **174**, 495 (2004) [*Phys. Usp.* **47**, 447 (2004)].
3. A. Piel and A. Melzer, *Plasma Phys. Controlled Fusion* **44**, R1 (2002).
4. C. Zafiu, A. Melzer, and A. Piel, *Phys. Plasmas* **9**, 4794 (2002); **10**, 1278 (2003).
5. S. A. Khrapak, A. V. Ivlev, G. E. Morfill, *et al.*, *Phys. Plasmas* **10**, 4579 (2003).
6. C. Zafiu, A. Melzer, and A. Piel, *Phys. Plasmas* **10**, 4582 (2003).
7. A. F. Pal', D. V. Sivokhin, A. N. Starostin, *et al.*, *Fiz. Plazmy* **28**, 32 (2002) [*Plasma Phys. Rep.* **28**, 28 (2002)].
8. A. V. Filippov, N. A. Dyatko, A. F. Pal', and A. N. Starostin, *Fiz. Plazmy* **29**, 214 (2003) [*Plasma Phys. Rep.* **29**, 190 (2003)].
9. O. Bystrenko and A. Zagorodny, *Phys. Rev. E* **67**, 066403 (2003).
10. A. G. Leonov, A. F. Pal', A. N. Starostin, and A. V. Filippov, *Pis'ma Zh. Éksp. Teor. Fiz.* **77**, 577 (2003) [*JETP Lett.* **77**, 482 (2003)].
11. A. G. Leonov, A. F. Pal', A. N. Starostin, and A. V. Filippov, *Zh. Éksp. Teor. Fiz.* **126**, 75 (2004) [*JETP* **99**, 61 (2004)].
12. V. N. Babichev, A. F. Pal', A. N. Starostin, *et al.*, *Pis'ma Zh. Éksp. Teor. Fiz.* **80**, 276 (2004) [*JETP Lett.* **80**, 241 (2004)].
13. S. I. Popel', A. P. Golub', and T. V. Losseva, *Pis'ma Zh. Éksp. Teor. Fiz.* **74**, 396 (2001) [*JETP Lett.* **74**, 362 (2001)].

Translated by R. Tyapaev

Global Synchronization of Oscillations in the Level of Whistlers near Jupiter as a Consequence of the Spatial Detection of the Q Factor of a Magnetosphere Resonator

P. A. Bespalov¹ and O. N. Savina²

¹ *Institute of Applied Physics, Russian Academy of Sciences, ul. Ul'yanova 46, Nizhni Novgorod, 603950 Russia*
e-mail: bespalov@appl.sci-nnov.ru

² *Nizhni Novgorod State Technical University, ul. Lenina 24, Nizhni Novgorod, 603600 Russia*

Received December 3, 2004; in final form, January 24, 2005

The formation of the space–time structure of the intensity distribution for whistlers, as well as the content of the energetic electrons in the radiation belts of Jupiter, has been considered. Parametric nonlinear processes in a plasma magnetospheric maser have been analyzed. It has been shown that, owing to the azimuthal inhomogeneity of a magnetic trap in combination with the fast rotation of the planet, a component that is characterized by the periodic modulation and is independent of the azimuth coordinate is formed in the Q factor of the magnetospheric resonator. This modulation is manifested as an external force that ensures the synchronization of oscillations in the level of whistlers in individual magnetic field tubes under the global-resonance conditions.
© 2005 Pleiades Publishing, Inc.

PACS numbers: 94.30.Hn, 95.55.Pe, 96.50.Ek

INTRODUCTION

In each magnetic field tube in the radiation belts of Jupiter, an oscillation process may occur in the form of alternating stages of the accumulation of energetic electrons and their precipitation into the ionosphere during electromagnetic radiation pulses generated when exceeding the cyclotron instability threshold. The local frequency Ω_{RB} of the corresponding oscillations depends on the power of the source of particles in the local magnetic field tube. Analysis revealed the global resonance effect in the electron radiation belts of Jupiter [1]. Calculations based on the data for the magnetosphere of Jupiter that were available at that time showed that the corresponding local frequencies of the oscillation process in individual tubes of the radiation belts of Jupiter were nearly identical, given by the expression

$$\Omega_{\text{RB}} = \left(\frac{cD|\ln R|}{R_J} \right)^{1/2}, \quad (1)$$

and close to the angular velocity Ω_J of the planet's rotation. Here, c is the speed of light, D is the coefficient of diffusion in the magnetic sheets ($D_{LL} = DL^4$), the reflection coefficient R of waves from the ionosphere from above will be discussed in detail below, and R_J is the radius of Jupiter.

It was argued in [2] that the coincidence of the frequencies Ω_{RB} and Ω_J is not accidental. They coincide with each other, because the aforementioned oscillation process determines the properties of the radial diffusion of energetic electrons in the radiation belts and, there-

fore, the power of the source of particles. It is useful to take into account that the efficiency of the interaction between waves and particles depends on the background plasma density determined by the threshold of the exchange instability [3].

Preliminary arguments that oscillations in different magnetic field tubes must be synchronous were given in [1, 2]. Recently, this conclusion has become urgent. Direct measurements of the intensity of electromagnetic radiation [4, 5] were carried out simultaneously on two spacecrafts (Galileo–Cassini/Huygens and Cassini/Huygens–Ulysses) in different positions with respect to Jupiter. Analyzing the results from the spacecrafts, Kaiser *et al.* [4] concluded that oscillations of the level of whistlers in individual magnetic field tubes are synchronous. This means that the entire giant magnetosphere of Jupiter in whistlers flashes with a period of 10 h, which is equal to the rotation period, as a huge lamp.

Those new experimental results have additionally stimulated the return to this problem and new explanation of the synchronization of oscillation processes in different magnetic field tubes within the framework of new, more advanced calculations. We consider the set of magnetic field tubes adjacent to a certain magnetic shell in the middle part of the magnetosphere of Jupiter, which is spaced by 20–40 radii of Jupiter from its center. The space–time dependence of the damping decrement for whistlers is shown to be important for the magnetosphere resonator. Moreover, it is shown that the damping decrement has a component depending

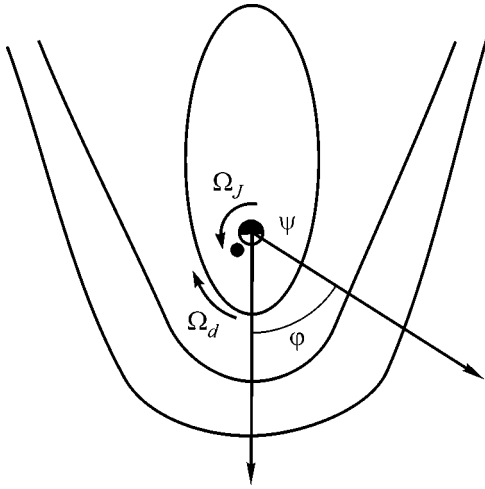


Fig. 1. Equatorial section of the Jupiter magnetosphere.

only on time with the planet-rotation period, because the decrement is determined both by the plasma parameters in the magnetic field tube and by the state of the asymmetric ionosphere. According to calculations, this component serves as an external force synchronizing oscillations of the radiation belt parameters in different magnetic field tubes.

SPATIAL DETECTION OF THE Q FACTOR OF THE MAGNETOSPHERIC RESONATOR

It is well known that laboratory lasers are successfully controlled by modulation of the Q factor of the resonator of electromagnetic waves. This property also fully concerns the plasma magnetospheric maser, where the conjugate ionospheric regions serve as mirrors. In view of this circumstance, it is important to analyze the average damping decrement of electromagnetic waves in the radiation belts. The space-time structure of the system is illustrated in Fig. 1, where the equatorial (in the ecliptic plane) section of the Jupiter magnetosphere is schematically shown with the outgoing head shock wave in the solar wind, magnetopause, and equatorial section of an individual magnetic sheet. We take a nearly inertial reference frame that, as well as the planet, rotates around the Sun and where the magnetosphere boundary is at rest. In addition, we introduce a noninertial comoving reference frame that rotates along with Jupiter and whose position is determined by the polar coordinate system. The azimuth angle φ is measured from the fixed axis directed from the planet center against the solar-wind direction.

The average damping decrement for whistlers in an individual tube can be written in the form [6]

$$\nu = 2|\ln R|T_g^{-1}. \quad (2)$$

Here, the reflection coefficient R from the ends of the magnetic trap depends primarily on the ionospheric

state. Jupiter's ionosphere rotating with the planet is asymmetric (this property is indicated in Fig. 1 by the close circle at the ionospheric altitude) due partially to the considerable shift of the magnetic dipole with respect to the planet center [7]. Therefore, $2|\ln R| = f_1(\varphi - \Omega_J t)$, where f_1 is a 2π -periodic function and φ is the azimuth angle. The period T_g of the group propagation of whistlers in the magnetospheric resonator is in turn a periodic function of the azimuth angle φ , because it is determined by the structure of the magnetosphere, namely, by the degree of the magnetosphere oblateness and the plasma density along the magnetic field tube. Both these parameters depend primarily on the local time. Therefore, $T_g^{-1} = f_2(\varphi)$, where $f_2(\varphi)$ is a 2π -periodic function. Thus, the average damping decrement of whistlers can be represented in the form

$$\nu(t, \varphi) = f_1(\varphi - \Omega_J t) f_2(\varphi). \quad (3)$$

The above periodic functions can be expanded in the Fourier series

$$\begin{aligned} & f_1(\varphi - \Omega_J t) \\ &= \sum_{k=0}^{\infty} \{a_{1k} \sin[k(\varphi - \Omega_J t)] \\ &+ a_{2k} \cos[k(\varphi - \Omega_J t)]\}, \end{aligned} \quad (4)$$

$$f_2(\varphi) = \sum_{k=0}^{\infty} [b_{1k} \sin(k\varphi) + b_{2k} \cos(k\varphi)].$$

The substitution of Eqs. (4) into Eq. (3) yields

$$\nu(t, \varphi) = \psi(t) + a_{20} f_2(\varphi) + \Phi(t, \varphi), \quad (5)$$

where

$$\begin{aligned} \psi(t) = & \frac{1}{2} \sum_{k=1}^{\infty} [(a_{1k} b_{1k} + a_{2k} b_{2k}) \cos(k\Omega_J t) \\ & + (a_{2k} b_{1k} - a_{1k} b_{2k}) \sin(k\Omega_J t)], \end{aligned}$$

and the function $\Phi(t, \varphi)$ satisfies the relation

$$\int_0^{2\pi} \Phi(t, \varphi) d\varphi = 0. \quad (6)$$

According to Eq. (5), the expression for the damping decrement of whistlers is represented as a sum of three terms. The first term is time periodic with the Jupiter rotation period T_J and is independent of the azimuth angle. The second term depends only on the azimuth angle. The third term depends on time and the azimuth angle, but its angle average is equal to zero.

Thus, spatial detection appears because the average damping decrement of whistlers and, therefore, the Q factor of the magnetospheric resonator of the plasma maser in the radiation belts of Jupiter are determined,

according to Eq. (3), by the product of two quantities depending on the time and azimuth angle. Below, we will analyze the effect of the periodic time dependence of the average damping decrement on the dynamics of the plasma magnetospheric maser.

SPACE-TIME DYNAMICS OF THE CYCLOTRON INSTABILITY OF RADIATION BELTS

In the simplest balance approximation, the self-consistent system of relativistic quasi-linear equations of interaction between the wave and particles in the plasma magnetospheric maser has the form [2, 6]

$$\frac{\partial N}{\partial t} - \Omega_d(\varphi) \frac{\partial N}{\partial \varphi} = -\delta(\varphi)WN - \frac{N}{T_l} + I(t, \varphi), \quad (7a)$$

$$\frac{\partial W}{\partial t} = h(\varphi)WN - \nu(t, \varphi)W + a. \quad (7b)$$

System (7) has a simple physical meaning. The number $N(t, \varphi)$ of particles in the magnetic field tube with unit cross section at the ionospheric level increases with time according to the power $I(t, \varphi)$ of the source of particles. The motion of particles along the azimuthal coordinate is caused by the drift of energetic particles in the inhomogeneous curved magnetic field. The corresponding angular velocity $\Omega_d(\varphi)$ is given by the formulas presented, e.g., in [8]. The second term on the right-hand side of Eq. (7a) presents losses of particles from the magnetic field tube due to synchrotron radiation (pair collisions in the Jupiter magnetosphere are of low importance). The first term on the right-hand side of Eq. (7a) presents a decrease in the number of particles in the magnetic field tube due to their precipitation into the ionosphere as a result of interaction with whistlers. This precipitation is faster for a higher energy density $W(t, \varphi)$ of the whistlers. In turn, the energy density of the whistlers is determined by transport equation (7b) averaged over the time of the whistler propagation between the conjugate regions of the ionosphere. In this equation, the power of external wave sources (e.g., lightning discharges in the atmosphere) is represented by the term a . The transverse angular anisotropy of the momentum distribution function varies slightly. Therefore, the double increment of the cyclotron instability can be written in the form $2\gamma(\varphi) = h(\varphi)N(\varphi)$. Note that the explicit expressions for the functions $\delta(\varphi)$ and $h(\varphi)$ can be obtained from formulas presented in [2], but they are unnecessary here. First, we consider processes in an individual magnetic field tube disregarding the azimuthal drift and for a fixed azimuth angle φ . In this case, the system of equations has a steady state corresponding to the balance between the arrival of particles from the source and their precipitation into the ionosphere. Let us analyze the oscillations near the steady state. In the radiation belts, where the parameters $1/T_l$

and a are small, for a constant damping decrement ν , relaxation oscillations occur with the parameters

$$\Omega_{\text{RB}} = (hI)^{\frac{1}{2}}, \quad 2\nu_{\text{RB}} = \frac{hI}{\nu}, \quad (8)$$

$$Q_{\text{RB}} = \frac{\Omega_{\text{RB}}}{2\nu_{\text{RB}}} = \frac{\nu}{(hI)^{\frac{1}{2}}},$$

where Ω_{RB} is the natural frequency of the oscillation process in a given magnetic field tube and ν_{RB} and Q_{RB} are the damping decrement and Q factor of these oscillations, respectively.

Upon the modulation of the damping decrement ν even in the space-time case, a resonance response is naturally expected in the form of the deep modulation of the parameters of the radiation belts and the level of whistlers, particularly when $Q_{\text{RB}} \gg 1$.

For simplified quantitative analysis of system (7), it is natural to introduce the new dimensionless variables

$$\tau = \Omega_J t, \quad \tau_* = \left(\frac{1}{\Omega_J T_l} + \omega_d \frac{\partial \ln h}{\partial \varphi} \right), \quad \omega_d = \frac{\Omega_d}{\Omega_J}, \quad (9)$$

$$\omega_{\text{RB}} = \frac{\Omega_{\text{RB}}}{\Omega_J}, \quad n = \frac{hN}{\Omega_J}, \quad \varepsilon = \frac{\delta}{\Omega_J} W, \quad \alpha = \frac{a\delta^2}{\Omega_J}.$$

In the new variables and in view of Eq. (5), system (7) is written as

$$\frac{\partial n}{\partial \tau} - \omega_d(\varphi) \frac{\partial n}{\partial \varphi} = -\varepsilon n - \frac{n}{\tau_*(\varphi)} + \omega_{\text{RB}}^2(\varphi), \quad (10)$$

$$\frac{\partial \varepsilon}{\partial \tau} = \varepsilon n - Q[\Psi(\tau) + a_{20}f_2(\varphi) + \Phi(\tau, \varphi)]\varepsilon + \alpha.$$

Here, all functions of φ are 2π -periodic functions, $Q = Q_{\text{RB}}(\Omega_{\text{RB}}/\Omega_J) \approx Q_{\text{RB}} \gg 1$, and the function $\Phi(\tau, \varphi)$ satisfies Eq. (6). Owing to the presence of the function $\Psi(\tau)$ in system (10), the time structure is formed in oscillations of both the intensity of whistlers and the content of energetic electrons and this structure is synchronous over the entire magnetosphere. To corroborate this statement, we performed numerical calculations.

MODEL CALCULATIONS

In the numerical calculation illustrating the fundamental aspect of the problem, only lower spatial harmonics are taken into account and the space-time dependence of the damping decrement of whistlers is written in the form

$$\nu/\Omega_J = Q_0(1 + \Delta_1 \cos \varphi)(1 + \Delta_2 \cos(\varphi - \tau)). \quad (11)$$

Here, the factor $\Delta_1 > 0$ reflects the fact that the length of the magnetic field tube is minimal and maximal at $\varphi = 0$ and π , respectively; and the factor $\Delta_2 > 0$ presents the fact that, when $\tau = 0$, the reflection coefficient is maxi-

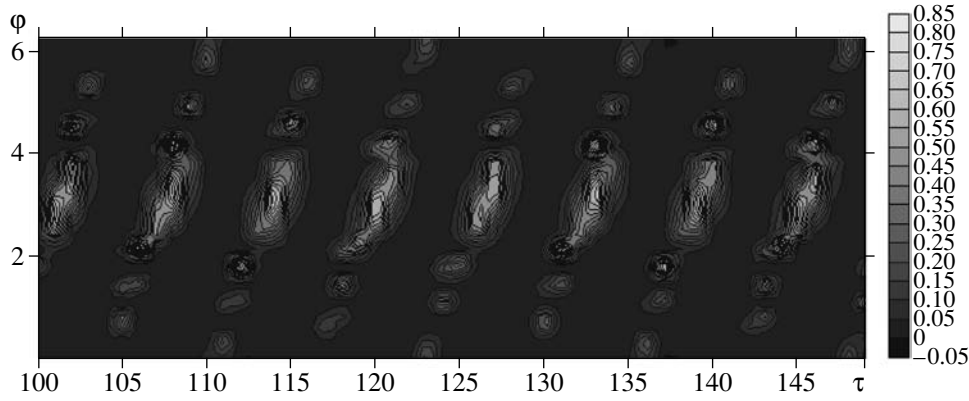


Fig. 2. Energy density ε of whistlers as a function of the azimuth angle φ and time τ as shown by different grey tones.

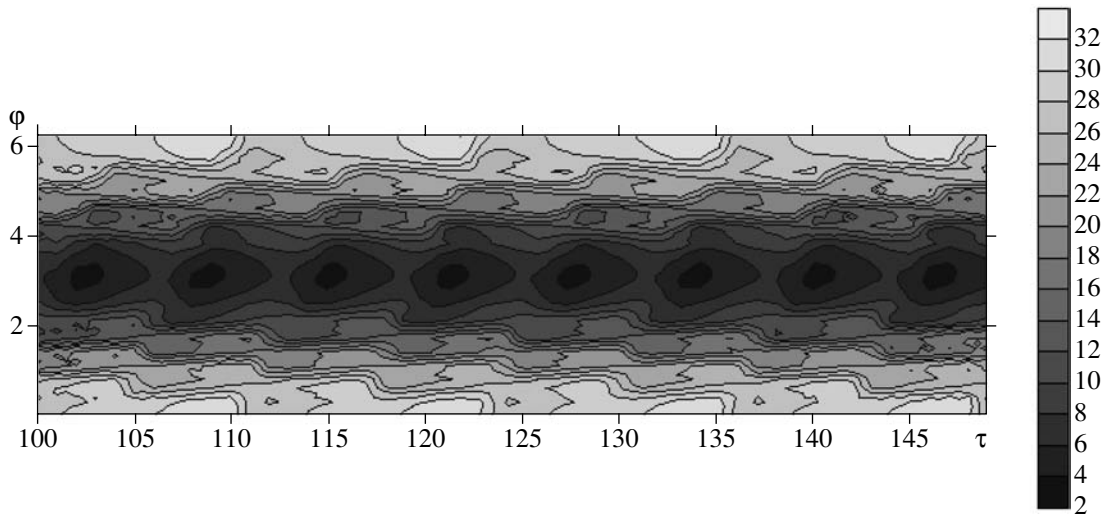


Fig. 3. Same as in Fig. 2 but for the total number n of energetic electrons in the magnetic field tube.

mal at $\varphi = 0$ for the appropriate choice of the time beginning point (see Fig. 1). Let us numerically analyze the properties of solutions of system (10). We take into account the azimuth angle dependence of $\omega_{\text{RB}}^2(\varphi)$ in the form

$$\omega_{\text{RB}}^2(\varphi) = \omega_{\text{RBo}}^2(1 + \Delta_2 \cos(\varphi)), \quad (12)$$

where the coefficients on the right-hand side roughly characterize the longitudinal inhomogeneity of the system in the power of the source of energetic particles and other parameters.

Since the natural frequency of the oscillation process in individual magnetic field tubes is close to the angular velocity of the planet rotation, we take $\omega_{\text{RBo}}^2 = 0.9$ in our model calculations. The depth of modulation associated with the asymmetry of the ionosphere is taken not too large, $\Delta_2 = 0.2$. The Q factors of the oscillation process at different longitudes may differ notice-

ably from each other. For this reason, we take $Q_o = 20$ and $\Delta_1 = 0.75$ in our model calculations. The remaining parameters that are comparatively small in the problem under consideration are assumed to be constant: $\omega_d = 0.03$, $1/\tau_* = 0.01$, and $a = 0.005$. Note that the real velocities of the azimuthal drift of energetic particles in the inhomogeneous curved magnetic field slightly affect the calculations. For this reason, we change the corresponding function to constant. At the same time, the test calculations show that, if the corresponding velocity were higher, time processes in different magnetic field tubes would be additionally synchronized. For definiteness, we take the initial conditions in the form $n(0, \varphi) = 10$ and $\varepsilon(0, \varphi) = 0.01$.

System (10) was numerically solved with the chosen model parameters. The energy density ε of whistlers as a function of time τ and the azimuth angle φ after the transient process is shown by different grey tones in Fig. 2. According to the calculations, the oscillation

process occurs with different efficiencies at different longitudes. However, maxima of the intensity of whistlers are reached quite synchronously over the entire magnetosphere. The space–time dependence of the total number n of energetic electrons in the magnetic field tube is shown by different grey tones in Fig. 3. Note that the time dependence of the total number of particles clearly exhibits the periodicity with a double period of 4π , which corresponds to a period of 20 h in the dimensional variables.

CONCLUSIONS

In the magnetosphere of Jupiter, interaction between waves and particles in individual magnetic field tubes clearly correlates with the global dynamics of electron radiation belts. This interplay is manifested in the pronounced periodicity of the intensity of whistlers and fluxes of energetic electrons. The entire giant magnetosphere of Jupiter in whistlers flashes as a huge lamp.

The experimentally observed law is likely due to several factors. First, it is important that each magnetic field tube in the radiation belts of Jupiter is characterized by the natural frequency that corresponds to interaction between waves and particles and is close to the angular velocity of Jupiter. This circumstance ensures the resonance character of the process, and a comparatively weak external action can thereby provide the deep modulation of the level of waves and particle fluxes.

Owing to the rotation of the planet with the asymmetric ionosphere, the spatial detection of the Q factor of the magnetospheric resonator occurs. The average damping decrement of whistlers includes a term that is independent of the azimuth angle and varies with time strictly periodically with the period of the orbital rotation of Jupiter. This periodic dependence is manifested as a controlling factor. (The plasma magnetospheric maser is subjected to several external factors. The modulation of the Q factor of the magnetospheric resonator most strongly affects its operation.) According to the calculations, the modulation of the level of whistlers is clearly synchronized at all longitudes. As can be shown and was checked in numerical calculations, the transport of particles and waves between individual magnetic field tubes improves the synchronization of processes in different magnetic field tubes.

The significance of this effect is more general. It must be observed for other types of electromagnetic radiation emitted due to the radiation belts of Jupiter, which vary quite synchronously in various spectral ranges of the magnetosphere. The synchronization of emission processes from different magnetic field tubes was noted in [5].

We emphasize that there is one more mechanism of the effect of the azimuthal drift of particles, which is taken into account in Eq. (7a), on the cyclotron instability and interaction between waves and particles. The drift of particles may create a polarization electric field

and thereby a current system and a magnetic signal, which changes the distribution function of energetic electrons due, e.g., to the conservation of the adiabatic invariants. However, estimates show that this mechanism is inefficient in the electron radiation belts of Jupiter. Indeed, the conductivity of the magnetospheric plasma along the magnetic field is very high, and the polarization field is short-circuited through the ionosphere, where the conductivity across the magnetic field is high. Polarization electric fields should be taken into account when analyzing the initial stage of the space–time evolution of the distributions of particles with sharp azimuthal gradients.

More complicated cases are possible when the initial oscillations are not relaxation oscillations but self-sustained oscillations in individual magnetic fields. The possibility of existing of the latter oscillations was shown in [9]. Under certain conditions, the synchronization of processes can be expected in the magnetosphere of pulsars. However, each of the mentioned cases requires special investigation.

Note that the above effect is an interesting example of the Huygens effect known in classical mechanics. In this case, oscillation processes in different magnetic field tubes (rough clock) are synchronized due to interaction with the strictly periodic orbital rotation of the planet (accurate clock).

This work was supported in part by the Russian Foundation for Basic Research (project no. 00-15-96674 for the support of leading scientific schools); the Branch of General Physics and Astronomy, Russian Academy of Sciences (Fundamental Program “Solar Wind: Generation and Interaction with the Earth and Other Planets”); and INTAS (grant no. 03-51-3922).

REFERENCES

1. P. A. Bespalov, *Pis'ma Astron. Zh.* **11**, 72 (1985) [*Sov. Astron. Lett.* **11**, 30 (1985)].
2. P. A. Bespalov, *Planet. Space Sci.* **44**, 565 (1996).
3. P. A. Bespalov and S. S. Davydenko, *Planet. Space Sci.* **42**, 583 (1994).
4. M. L. Kaiser *et al.*, *J. Geophys. Res.* **109** (2004).
5. G. B. Hospodarsky *et al.*, *J. Geophys. Res.* **109** (2004).
6. P. A. Bespalov and V. Yu. Trakhtengerts, in *Reviews of Plasma Physics*, Ed. by M. A. Leontovich (Atomizdat, Moscow, 1980; Plenum, New York, 1986), Vol. 10, p. 155.
7. T. W. Hill, A. J. Dessler, and C. K. Goertz, in *Physics of the Jovian Magnetosphere*, Ed. by A. J. Dessler (Cambridge Univ. Press, Cambridge, 1983), p. 353.
8. D. L. Hamlin, R. Karplus, R. C. Vik, *et al.*, *J. Geophys. Res.* **66**, 1 (1961).
9. P. A. Bespalov, *Pis'ma Zh. Éksp. Teor. Fiz.* **33**, 192 (1981) [*JETP Lett.* **33**, 182 (1981)].

Translated by R. Tyapaev

Ballistic Conductance of a Point Contact between a d -Type Superconductor and a Ferromagnet

B. P. Vodopyanov

Zavoiskii Physicotechnical Institute, Kazan Scientific Center, Russian Academy of Sciences,
Kazan, 420029 Tatarstan, Russia

e-mail: vodop@kzn.ru

Received December 20, 2004; in final form, January 11, 2005

The ballistic conductance of a point contact between a strong ferromagnet and a d -wave superconductor is calculated for arbitrary spin-dependent transmission coefficients. The width of the localized Andreev state level is determined. The possibility of identifying the d -type superconductor by the shape of the voltage dependence of the conductance is analyzed for a point contact with a good metallic conduction. © 2005 Pleiades Publishing, Inc.

PACS numbers: 74.50.+r, 74.80.-g, 75.30.Et

Studies of ballistic electron transport between ferromagnetic metals (Fs) and high-temperature superconductors (HTSCs) [1–3] are important for understanding the electronic properties of these materials and for the development of electronic devices using spin-polarized currents [1, 4–6]. The main distinctive feature of HTSCs, as compared to ordinary s -wave superconductors, is the anisotropy of the order parameter. It has been established [7, 8] that the order parameter in HTSCs has the $d_{x^2-y^2}$ symmetry. Superconductors (Ss) with a d -wave symmetry possess a momentum-dependent internal phase, which strongly affects the transport properties of the contacts between them and other materials. In [9], it was shown that, when the angle α between the a axis of an HTSC crystal and the vector perpendicular to the surface of a high-resistance contact is equal to $\pi/4$, quasiparticle bound states are formed at the Fermi level near the high-resistance boundary. In [10], it was found that these bound states give rise to a sharp zero-voltage peak in the tunneling conductance between HTSCs and normal metals (Ns). The experimental observation of such a peak at low temperatures is considered as evidence of the d -wave symmetry of the order parameter. The observation of the splitting of this peak is interpreted as a manifestation of the surface-induced near-boundary order parameter with broken time-reversal symmetry [11–13]. Theoretical studies of the effect of Andreev bound states, which arise due to the interference of the incident and Andreev-reflected quasiparticles, on the spin-polarized quasiparticle transport in F/S contacts were carried out in [14–17]. Those studies were based on the generalization of the theory developed in [18] (the BTK theory) to F/S structures. It was found that the properties of Andreev reflection noticeably vary in the presence of exchange interaction. The splitting of the zero-voltage peak of

conductance under the effect of exchange interaction was obtained in [16].

However, the authors of recent paper [19] arrived at the conclusion that the works in which the BTK theory was generalized to F/S structures disregarded important physical aspects of Andreev reflection and did not correctly describe the transport through an F/S interface. The fact that these works did not reproduce the formula obtained for the zero-temperature Andreev conductance from physical considerations was mentioned in [20]. This supports the conclusion made in [19]. At the same time, the number of experimental studies of the electron transport through the F/S interface increases, which requires an adequate theoretical description of this phenomenon.

The aims of this study are, (i) using the semiclassical theory of superconductivity for metals with a spin-split conduction band [20], to obtain an analytical expression for the ballistic conductance of a point contact between a strong ferromagnet and a d -wave superconductor at arbitrary values of spin-dependent transmission coefficients; (ii) to determine the role of the transparency of the F/S interface in the formation of the spectrum of Andreev bound states in the HTSC; and (iii) to analyze the possibility of identifying the d -wave superconductor by the shape of the derivative of the current–voltage dependence characterizing its point contact with the ferromagnet when this contact exhibits a good metallic conduction.

DIFFERENTIAL CONDUCTANCE OF AN F/HTSC POINT CONTACT

The general expression for the current through a point contact between a normal metal and a supercon-

ductor was obtained in [18]. For the F/S contact, this expression can be represented in the form

$$I_{F/S} = \frac{1}{e} \int_{-\infty}^{\infty} d\varepsilon (f_0(\varepsilon - eV) - f_0(\varepsilon)) G_{F/S}(\varepsilon). \quad (1)$$

Here, $f_0(\varepsilon)$ is the Fermi equilibrium distribution function and $G_{F/S}$ is the spectral density of the conductance of the F/S point contact at zero voltage. Let the ferromagnet lie to the left of the boundary $x = 0$, and the superconductor, to the right (in the region of $x > 0$). The x coordinate axis and the a - b crystallographic plane of the HTSC crystal are perpendicular to the contact plane. The expression for $G_{F/S}(\varepsilon)$ in terms of matrix semiclassical Green's functions was obtained in [20]:

$$G_{F/S}(\varepsilon) = \frac{e^2 A}{4\pi} \text{Tr} \tau_z \int \frac{d\mathbf{p}_{\parallel}}{(2\pi)^2} [1 - \hat{g}_s^R \tau_z \hat{g}_s^A - \hat{g}_a^R \tau_z \hat{g}_a^A + \hat{Y}_s^R \tau_z \hat{Y}_s^A - \hat{Y}_a^R \tau_z \hat{Y}_a^A]. \quad (2)$$

In Eq. (2), (\hat{g}_s, \hat{Y}_s) and (\hat{g}_a, \hat{Y}_a) are retarded (superscript R) and advanced (superscript A) semiclassical Green's functions that are symmetric (subscript s) and antisymmetric (subscript a) with respect to the projection of the momentum $\hat{\mathbf{p}}$ taken at the Fermi surface onto the x axis. All the Green's functions refer to the ferromagnet and are calculated at $x = 0$. To determine these functions, for each of the metals, it is necessary to solve the semiclassical superconductivity equations for metals with a spin-split conduction band [20]:

$$\text{sgn}(\hat{p}_x) \frac{\partial}{\partial x} \hat{g} + \frac{1}{2} \mathbf{v}_{\parallel} \frac{\partial}{\partial \rho} (\hat{v}_x^{-1} \hat{g} + \hat{g} \hat{v}_x^{-1}) + [\hat{K}, \hat{g}]_{-} = 0,$$

$$\hat{K} = -i \hat{v}_x^{-\frac{1}{2}} (i\varepsilon_n \hat{\tau}_z + \hat{\Delta} - \hat{\Sigma}) \hat{v}_x^{\frac{1}{2}} - i(\hat{p}_x - \hat{\tau}_x \hat{p}_x \hat{\tau}_x)/2, \quad (3)$$

$$\hat{\Delta} \equiv \hat{\Delta}(x, \mathbf{p}_F), \quad [a, b]_{\pm} = ab \pm ba.$$

Here, $\varepsilon_n = (2n + 1)\pi T$ is the Matsubara frequency, \mathbf{p}_F is the momentum at the Fermi surface, and $\hat{\tau}$ represents the Pauli matrices. The matrices \hat{g} , $\hat{\Delta}$, and \hat{p}_x have the structures

$$\hat{g} = \begin{pmatrix} g_{\alpha\alpha} & f_{\alpha-\alpha} \\ f_{-\alpha\alpha}^+ & \bar{g}_{-\alpha-\alpha} \end{pmatrix}, \quad \hat{g} = \begin{cases} \hat{g}_{>} & \hat{p}_x > 0 \\ \hat{g}_{<} & \hat{p}_x < 0 \end{cases}, \quad (4)$$

$$\hat{\Delta} = \begin{pmatrix} 0 & \Delta \\ -\Delta^* & 0 \end{pmatrix}, \quad \hat{p}_x = \begin{pmatrix} p_{x\alpha} & 0 \\ 0 & p_{x(-\alpha)} \end{pmatrix}.$$

In Eqs. (4), $\alpha = (\uparrow, \downarrow)$ is the spin index and $\hat{\Sigma}$ is the self-energy part.

Equations (3) should be solved with the boundary conditions formulated in [20]:

$$\begin{aligned} (\hat{g}_a^S)_d &= (\hat{g}_a^F)_d, & (\hat{Y}_a^S)_d &= (\hat{Y}_a^F)_d, \\ (\sqrt{\hat{R}_\alpha} - \sqrt{\hat{R}_{-\alpha}})(\hat{Y}_a^+)_n &= \alpha_3(\hat{g}_a^-)_n, \\ (\sqrt{\hat{R}_\alpha} - \sqrt{\hat{R}_{-\alpha}})(\hat{Y}_a^-)_n &= \alpha_4(\hat{g}_a^+)_n, \\ -\hat{Y}_s^- &= \sqrt{\hat{R}_\alpha}(\hat{g}_s^+)_d + \alpha_1(\hat{g}_s^+)_n, \\ -\hat{Y}_s^+ &= (\hat{R}_\alpha)^{\frac{1}{2}}(\hat{g}_s^-)_d + \alpha_2(\hat{g}_s^-)_n, \end{aligned} \quad (5)$$

where $\hat{g}_{a(s)}^{\pm} = 1/2[\hat{g}_{a(s)}^S \pm \hat{g}_{a(s)}^F]$. The functions $\hat{Y}_{a(s)}^{\pm}$ are determined in a similar way. The explicit form of matrices $\hat{g}_s^{S(F)}$ is given in [20]. The structure of the matrices of transmission coefficients \hat{D}_α and reflection coefficients \hat{R}_α ($\hat{R}_\alpha = 1 - \hat{D}_\alpha$) is the same as the structure of the matrix \hat{p}_x in Eqs. (4). Subscripts d and n indicate the diagonal and off-diagonal parts of the matrix, respectively: $\hat{T}_{d(n)} = 1/2[\hat{T} \pm \tau_z \hat{T} \tau_z]$. The coefficients α_i are determined as

$$\alpha_{1(2)} = \frac{1 + \sqrt{R_\uparrow R_\downarrow} \mp \sqrt{D_\uparrow D_\downarrow}}{\sqrt{R_\uparrow} + \sqrt{R_\downarrow}},$$

$$\alpha_{3(4)} = 1 - \sqrt{R_\uparrow R_\downarrow} \pm \sqrt{D_\uparrow D_\downarrow}.$$

Knowing the functions $g_{s(a)}$, we use boundary conditions (5) to derive the matrices \hat{Y}_s^{\pm} and $(\hat{Y}_a^{\pm})_n$. To determine the matrix $(\hat{Y}_a^{\pm})_d$, we find one more relationship between the matrices \hat{g} and \hat{Y} .

Multiply equation (4) from [20] by $\hat{G}_{mk}(x', x)$ from the left and its conjugate equation by $\hat{G}_{kn}(x, x')$ from the right. Subtracting one from the other, we obtain

$$-(-1)^k \frac{\partial}{\partial x} (\hat{G}_{mk}(x', x) \hat{v}_{xj} \hat{G}_{kn}(x, x')) = 0. \quad (6)$$

From this equation, it follows that

$$\hat{G}_{mk}(x', x) \hat{v}_{xj} \hat{G}_{kn}(x, x') = 0, \quad (7)$$

because $\hat{G}_{kn}(x, x')$ is equal to zero at infinity. Changing to the functions $\hat{g}_{a(c)}$ in Eq. (7) with the use of formulas (5) from [20], we arrive at the expressions

$$\begin{aligned} \hat{g}_s^F \hat{Y}_s^F + \hat{g}_a^F \hat{Y}_a^F &= -\hat{Y}_a^F, & \hat{g}_s^S \hat{Y}_s^S + \hat{g}_a^S \hat{Y}_a^S &= \hat{Y}_a^S, \\ \hat{Y}_s^F \hat{g}_s^F - \hat{Y}_a^F \hat{g}_a^F &= \hat{Y}_a^F, & \hat{Y}_s^S \hat{g}_s^S - \hat{Y}_a^S \hat{g}_a^S &= \hat{Y}_a^S. \end{aligned} \quad (8)$$

Eliminating the functions \hat{Y}_a^F and \hat{Y}_a^S from these relations, we obtain a set of boundary conditions for the Green's functions \hat{g} :

$$\begin{aligned} \hat{g}_a^+ \hat{b}_1 + \hat{b}_2 \hat{g}_a^+ + \hat{g}_a^- \hat{b}_3 + \hat{b}_4 \hat{g}_a^- &= \hat{b}_3 - \hat{b}_4, \\ \hat{g}_a^- \hat{b}_1 + \hat{b}_2 \hat{g}_a^- + \hat{g}_a^+ \hat{b}_3 + \hat{b}_4 \hat{g}_a^+ &= \hat{b}_1 - \hat{b}_2. \end{aligned} \quad (9)$$

Matrices \hat{b}_i in Eqs. (9) are expressed as

$$\begin{aligned} \hat{b}_1 &= \hat{Y}_s^+ \hat{g}_s^- + \hat{Y}_s^- \hat{g}_s^+, & \hat{b}_2 &= \hat{g}_s^+ \hat{Y}_s^- + \hat{g}_s^- \hat{Y}_s^+, \\ \hat{b}_3 &= \hat{Y}_s^+ \hat{g}_s^+ + \hat{Y}_s^- \hat{g}_s^-, & \hat{b}_4 &= \hat{g}_s^+ \hat{Y}_s^+ + \hat{g}_s^- \hat{Y}_s^-. \end{aligned} \quad (10)$$

To determine $(\hat{Y}_a^+)_d$ appearing in Eq. (2), we use the second row of Eqs. (8):

$$(\hat{Y}_a^+)_d = (b_1)_d - (\hat{Y}_a^+)_n \hat{g}_a^- - \hat{Y}_a^-(\hat{g}_a^+)_n. \quad (11)$$

Now, solving the first of Eqs. (3) in combination with boundary conditions (9), we determine the matrices $\hat{g}_{s(a)}$. Then, with these matrices, from Eqs. (5) and (11), we determine the matrices $\hat{Y}_{s(a)}$. Substituting all the expressions determined above into Eq. (2), we calculate the conductance. Then, we assume that the order parameter is independent of the coordinate. This assumption will allow us to obtain an analytical solution of the problem. A self-consistent calculation of the order parameter does not change the qualitative conclusions derived from such a solution [21]. For a spatially homogeneous order parameter, the solution of the first of Eqs. (3) for each of the metals has the form [22]

$$\hat{g} = e^{-\text{sgn}(\hat{p}_x) \hat{K} x} \hat{C}(\mathbf{p}_F) e^{\text{sgn}(\hat{p}_x) \hat{K} x} + \hat{C}_0(\mathbf{p}_F). \quad (12)$$

Matrices $\hat{C}_0(\mathbf{p}_F)$ represent the values of the Green's function \hat{g} far from the F/S interface:

$$\hat{C}_0^S(\mathbf{p}_F) = \begin{pmatrix} g & f \\ f^+ & -g \end{pmatrix} = \frac{\begin{pmatrix} \varepsilon_n & -i\Delta(\mathbf{p}_F) \\ i\Delta^*(\mathbf{p}_F) & -\varepsilon_n \end{pmatrix}}{\sqrt{\varepsilon_n^2 + |\Delta(\mathbf{p}_F)|^2}}, \quad (13)$$

$$\hat{C}_0^F = \tau_z \frac{\varepsilon_n}{|\varepsilon_n|}, \quad \Delta(\mathbf{p}_F) = \Delta_d(T) \cos(2\theta^S - 2\alpha).$$

Here, θ^S is the angle between the electron momentum in the superconductor and the x axis. The Green's function \hat{g}^F in Eq. (12) should tend to \hat{C}_0^F when $x \rightarrow -\infty$, and the Green's function \hat{g}^S , to $\hat{C}_0^S(\mathbf{p}_F)$ when $x \rightarrow \infty$. Performing a matrix multiplication in Eq. (12), we con-

clude that, to satisfy the above conditions, the following relations should be valid at $x = 0$:

$$\begin{aligned} \hat{C}_0^F(\mathbf{p}_F) \hat{C}^F(\mathbf{p}_F) &= -\text{sgn}(p_x) \hat{C}^F(\mathbf{p}_F), \\ \hat{C}_0^S(\mathbf{p}_F) \hat{C}^S(\mathbf{p}_F) &= \text{sgn}(p_x) \hat{C}^S(\mathbf{p}_F). \end{aligned} \quad (14)$$

From these relations, it follows that

$$\begin{aligned} \hat{g}_s^S &= \hat{X} \hat{g}_a^S + \hat{X}, & \hat{X} &= (1 + \hat{C}_{0,s}^S)(\hat{C}_{0,s}^S)^{-1}, \\ \hat{g}_s^F &= \hat{C}_0^F - \hat{C}_0^F \hat{g}_a^F, & \hat{X} &= X_d \hat{\tau}_z + (\hat{X})_n. \end{aligned} \quad (15)$$

Here, $\hat{C}_{0,s(a)}$ represents the symmetric and antisymmetric combinations of the matrix $\hat{C}_0^S(\mathbf{p}_F)$ with respect to the projection of the Fermi momentum onto the x axis: $\hat{C}_{0,s(a)}^S = 1/2[\hat{C}_0^S(p_x) \pm \hat{C}_0^S(-p_x)]$; the matrix \hat{X} has the property $(\hat{X})^2 = \hat{1}$, which is verified by a direct calculation; and $(\hat{X})_n$ is the off-diagonal part of the matrix \hat{X} .

Now, from \hat{g}_s^S and \hat{g}_s^F determined by Eqs. (15), we construct combinations \hat{g}_s^\pm and, substituting them into the set of boundary conditions (9), we determine $\hat{g}_a^S(x=0)$ and $\hat{g}_a^F(x=0)$:

$$\begin{aligned} \hat{g}_a^S &= \frac{(1 - \sqrt{R_\uparrow R_\downarrow})(\hat{X})_n \hat{\tau}_z}{(1 + \sqrt{R_\uparrow R_\downarrow}) \text{sgn}(\varepsilon_n) + (1 - \sqrt{R_\uparrow R_\downarrow}) X_d}, \\ \hat{g}_a^F &= \frac{\sqrt{D_\uparrow D_\downarrow} (\hat{X})_n \hat{\tau}_z}{(1 + \sqrt{R_\uparrow R_\downarrow}) \text{sgn}(\varepsilon_n) + (1 - \sqrt{R_\uparrow R_\downarrow}) X_d}. \end{aligned} \quad (16)$$

When solving the set of boundary equations (9), we ignored the spin dependence of the phases of scattering amplitudes. Now, knowing the Green's functions \hat{g}_a^S and \hat{g}_a^F , we determine the expression for the spectral density of conductance, $G_{F/S}(\varepsilon)$, in terms of the matrix \hat{X} :

$$\begin{aligned} G_{F/S}(\varepsilon) &= \frac{e^2 A}{\pi} \int \frac{d\mathbf{p}_\parallel}{(2\pi)^2} \left[Z^R Z^A \right. \\ &+ (\sqrt{R_\uparrow} - \sqrt{R_\downarrow})^2 X_d^R X_d^A - (\sqrt{R_\uparrow} + \sqrt{R_\downarrow})^2 \\ &+ \left. \frac{1}{2} D_\uparrow D_\downarrow \text{Tr}[(\hat{X}^R)_n (\hat{X}^A)_n] \right] \frac{1}{Z^R Z^A}, \end{aligned} \quad (17)$$

$$Z^R = 1 + \sqrt{R_\uparrow R_\downarrow} + (1 - \sqrt{R_\uparrow R_\downarrow}) X_d^R,$$

$$Z^A = 1 + \sqrt{R_\uparrow R_\downarrow} - (1 - \sqrt{R_\uparrow R_\downarrow}) X_d^A.$$

Here, \hat{X}^R and \hat{X}^A are, respectively, the retarded and advanced matrices obtained from the matrix $\hat{X}(\varepsilon_n)$ given by Eqs. (15) after the analytic continuation:

$$\begin{aligned} X_d^R &= \frac{\varepsilon(\xi_{>}^R + \xi_{<}^R)}{\xi_{>}^R \xi_{<}^R + \varepsilon^2 - \Delta_{>} \Delta_{<}^*}, \\ \hat{X}_n^R &= \frac{\begin{pmatrix} 0, \Delta_{>} \xi_{<}^R + \Delta_{<} \xi_{>}^R - \varepsilon(\Delta_{>} - \Delta_{<}) \\ -\Delta_{>}^* \xi_{<}^R - \Delta_{<}^* \xi_{>}^R - \varepsilon(\Delta_{>}^* - \Delta_{<}^*), 0 \end{pmatrix}}{\xi_{>}^R \xi_{<}^R + \varepsilon^2 - \Delta_{>} \Delta_{<}^*}. \end{aligned} \quad (18)$$

In Eqs. (18), $\Delta_{>} = \Delta_d(T) \cos(2\theta^S - 2\alpha)$ and $\Delta_{<} = \Delta_d(T) \cos(2\theta^S + 2\alpha)$. The angle θ^S varies from zero to $\theta_0 \leq \pi/2$. The angle θ_0 is determined from the condition of mirror reflection of electrons from the boundary: $p_{\parallel} = p^S \sin \theta^S = p_{F\uparrow} \sin \theta_{\uparrow} = p_{F\downarrow} \sin \theta_{\downarrow}$. Here, $p_{F\uparrow}$, $p_{F\downarrow}$, and p^S are the Fermi momenta of spin subbands of the ferromagnet and superconductor, respectively. The quantity $\hat{\xi}_{>}^R$ has the form

$$\hat{\xi}_{>}^R = -(\hat{\xi}_{>}^A)^* = \begin{cases} \frac{\varepsilon}{|\varepsilon|} \sqrt{\varepsilon^2 - |\Delta_{>}|^2}, & \varepsilon^2 > |\Delta_{>}|^2 \\ i \sqrt{|\Delta_{>}|^2 - \varepsilon^2}, & \varepsilon^2 < |\Delta_{>}|^2. \end{cases}$$

The quantity $\hat{\xi}_{<}^R$ is determined in a similar way. Formulas (1) and (17) allow one to calculate the dependence of the conductance $\sigma_{F/S}(V) = dI_{F/S}/dV$ of an F/HTSC point contact on the applied voltage at arbitrary spin-dependent transmission coefficients and angles of orientation of the HTSC crystal axes with respect to the vector perpendicular to the contact plane. For the angles $\alpha = 0$ and $\alpha = \pi/4$, the expression for the conductance has a simple form:

$$\begin{aligned} \sigma_{F/S}(V) &= \frac{e^2 A}{\pi} \int \frac{d\mathbf{p}_{\parallel}}{(2\pi)^2} \left\{ \int_{|\Delta_{>}|}^{\infty} \frac{d\varepsilon}{2T} \left[\frac{1}{\cosh^2\left(\frac{\varepsilon + eV}{2T}\right)} \right. \right. \\ &+ \left. \frac{1}{\cosh^2\left(\frac{\varepsilon - eV}{2T}\right)} \right] \frac{\varepsilon \xi^R (D_{\uparrow} + D_{\downarrow}) + \varepsilon(\varepsilon - \xi^R) D_{\uparrow} D_{\downarrow}}{Z_{\uparrow}} \\ &+ \left. \int_0^{|\Delta_{>}|} \frac{d\varepsilon}{2T} \left[\frac{1}{\cosh^2\left(\frac{\varepsilon + eV}{2T}\right)} + \frac{1}{\cosh^2\left(\frac{\varepsilon - eV}{2T}\right)} \right] \right. \\ &\left. \times \frac{D_{\uparrow} D_{\downarrow} |\Delta_{>}|^2}{Z_{\downarrow}} \right\}, \end{aligned} \quad (19)$$

$$\begin{aligned} Z_{\uparrow} &= \begin{cases} [\varepsilon(1 - \sqrt{R_{\uparrow} R_{\downarrow}}) + \xi^R(1 + \sqrt{R_{\uparrow} R_{\downarrow}})]^2; & \alpha = 0 \\ [\varepsilon(1 + \sqrt{R_{\uparrow} R_{\downarrow}}) + \xi^R(1 - \sqrt{R_{\uparrow} R_{\downarrow}})]^2; & \alpha = \frac{\pi}{4}, \end{cases} \\ Z_{\downarrow} &= \begin{cases} (1 + \sqrt{R_{\uparrow} R_{\downarrow}})^2 |\Delta_{>}|^2 - 4\varepsilon^2 \sqrt{R_{\uparrow} R_{\downarrow}}; & \alpha = 0 \\ (1 - \sqrt{R_{\uparrow} R_{\downarrow}})^2 |\Delta_{>}|^2 + 4\varepsilon^2 \sqrt{R_{\uparrow} R_{\downarrow}}; & \alpha = \frac{\pi}{4}. \end{cases} \end{aligned}$$

Here, the limits of integration with respect to angles depend on the relative values of the Fermi momenta of the spin subbands in the ferromagnet and in the superconductor. If these values satisfy the condition $p_{F\downarrow} < p^S < p_{F\uparrow}$, the integration with respect to the angles in the region $p_{F\downarrow} < p_{\parallel} = p^S \sin \theta^S = p_{F\uparrow} \sin \theta_{\uparrow}$ should be performed by setting $D_{\downarrow} = 0$ and $R_{\downarrow} = 1$.

In the case of a nonmagnetic metal ($D_{\uparrow} = D_{\downarrow}$), at $\alpha = 0$, formula (19) yields the expression obtained in [22] for the conductance of an N/S point contact if $|\Delta|$ is replaced by $|\Delta_d(T) \cos(2\theta^S)|$. For $\alpha = \pi/4$, from Eq. (19) we obtain the expressions given in the review [23] for the spectral density of conductance (Eqs. (32) and (33) in [23]). For tunneling contacts, from Eqs. (1) and (19), at both $\alpha = 0$ and $\alpha = \pi/4$, one can obtain the expressions for the current that were given in [24].

DISCUSSION

Formula (19) differs from the expressions obtained earlier on the basis of the scattering theory [14–17] and leads to a number of qualitatively new results. From this formula, it follows that finite values of the spin-dependent reflection coefficients lead to a broadening of the Andreev bound state, whose width Γ is expressed as

$$\Gamma = \sqrt{\frac{(1 - \sqrt{R_{\uparrow} R_{\downarrow}})^2 |\Delta_d(T) \sin(2\theta_S)|^2}{4\sqrt{R_{\uparrow} R_{\downarrow}}} + \frac{1}{\tau_{\phi}^2}}. \quad (20)$$

Here, τ_{ϕ} is the quasiparticle phase breaking time, which is taken into account in semiclassical Green's functions (13) by the substitution $\varepsilon_n \rightarrow (\varepsilon_n + i \text{sgn}(\varepsilon_n)/\tau_{\phi})$. The width associated with the finite transparency of the F/S interface is the basic one at low temperatures. Hence, the normalized conductance $\sigma_{F/S}(V)/\sigma_0^F$ (where $\sigma_0^F = e^2(p_{F\uparrow}^2 + p_{F\downarrow}^2)/8\pi^2$ is the Sharvin conductance of the ferromagnet and $\sigma_0^F = e^2(p_{F\uparrow} + p_{F\downarrow})/2\pi^2$ in the two-dimensional case) cannot be greater than two; i.e., the limits of its variation are the same as those of the conductance at $\alpha = 0$.

When the polarization $\delta = p_{F\downarrow}/p_{F\uparrow}$ is equal to unity and the interface is characterized by a low transparency, formula (20) transforms to the expression obtained in [25, 26] for the width of the Andreev bound state in nonmagnetic tunneling contacts.

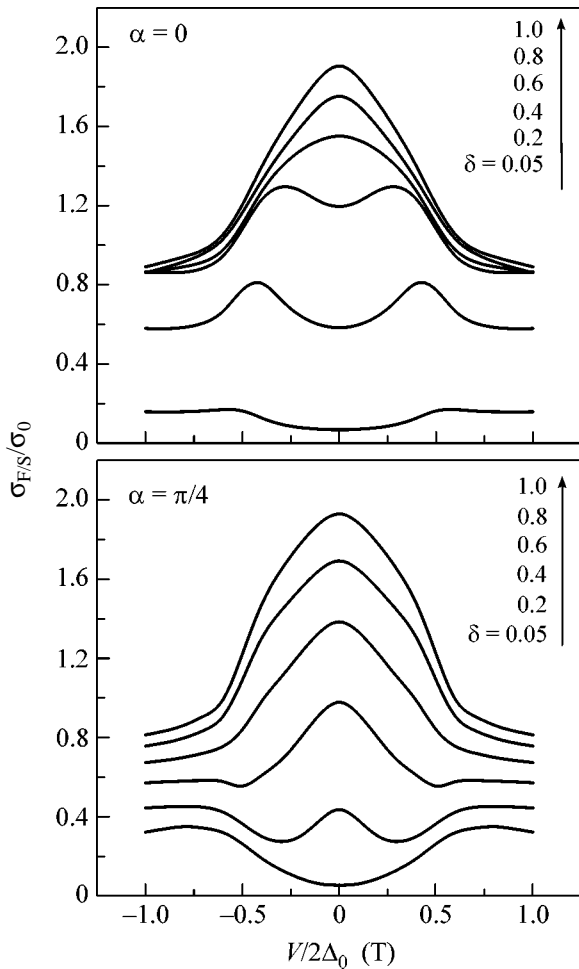


Fig. 1. Applied-voltage dependence of the normalized conductance $\sigma_{F/S}(V)/\sigma_0^F$ calculated by formula (19) for different values of the ferromagnet polarization $\delta = p_{F\downarrow}/p_{F\uparrow}$ at $\Delta_d(T)/2T = 5$.

From formula (19), it follows that, at $\alpha = \pi/4$, the spin-dependent potential barrier, which directly enters into the expression for the conductance in terms of the parameter $Z_{0, \uparrow[\downarrow]}$ in [16] and is taken into account in the determination of the spin-dependent transmission coefficients $D_{\uparrow[\downarrow]}$ in this work, does not lead to the splitting of the Andreev bound state if the effect of the induced magnetization on the energy spectrum of the HTSC is ignored. As the polarization of the ferromagnet increases, the peak of the conductance at $V = 0$ is not split but suppressed (in Figs. 1 and 2, this is illustrated for F/S contacts with a good metallic conduction). This conclusion follows from the shape of the subgap conductance line and from the contribution of the spin-dependent transmission coefficients to the total conductance at $\alpha = \pi/4$. The subgap conductance has the form of a Lorentzian that does not broaden with an increase in the polarization of the ferromagnet. The quasiparticle part of the conductance is proportional to the sum of

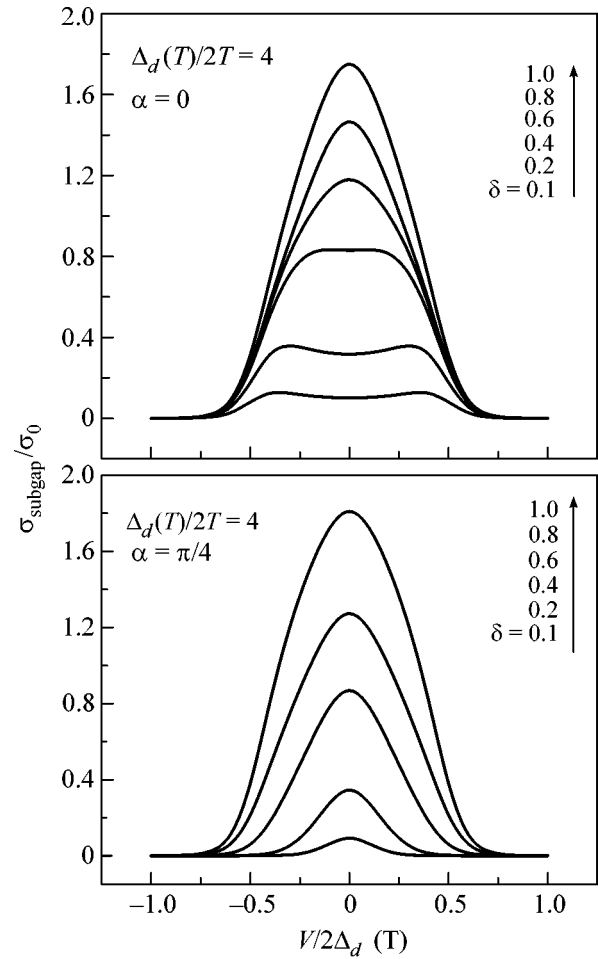


Fig. 2. Applied-voltage dependence of the subgap ($\epsilon < |\Delta_d|$) conductance.

the transmission coefficients with different spins, $D_{\uparrow} + D_{\downarrow}$, with weights independent of the energy variable, so that the splitting of the total conductance because of the spin-dependent barrier potentials is impossible for any values of $Z_{0, \uparrow[\downarrow]}$.

The splitting in the absence of an external magnetic field is possible only when the effect of the spin-polarized current [27] or induced exchange field [28] on the energy spectrum of the superconductor is taken into account.

Let us analyze the possibility of identifying a d -wave superconductor by the shape of the derivative of the current–voltage dependence characterizing its point contact with a ferromagnet in the absence of a potential barrier. For this purpose, we perform a numerical calculation using model expressions for the transmission

coefficients that correspond to a direct contact between metals (for p^S , we use $p^S = (p_{F\downarrow} + p_{F\uparrow})/2$):

$$D_{\uparrow} = \frac{4p_{x\uparrow}p_{xs}}{(p_{x\uparrow} + p_{xs})^2}, \quad D_{\downarrow} = \frac{4p_{x\downarrow}p_{xs}}{(p_{x\downarrow} + p_{xs})^2}. \quad (21)$$

From Fig. 1, one can see that, as the ferromagnet polarization δ increases, the peak value of the conductance at $\alpha = 0$ is suppressed, as in the case of an s -wave superconductor [20, 29]. This can be explained by the fact that the efficiency of Andreev reflection is determined by the number of conducting channels in the subband with the smaller value of the Fermi momentum (in the case under consideration, it is $p_{F\downarrow}$), which decreases with increasing polarization of the ferromagnet.

Only when the degree of polarization of the ferromagnet is very high, $\delta \leq 0.1$, does the quasiparticle part of the conductance, together with the contribution from the Lorentzian wings, exceed the peak value of the Lorentzian. The peak in the conductance at $V = 0$ disappears, and the dependence $\sigma_{F/S}(V)$ becomes V-shaped. This type of dependence was observed in the experiment with an F/S structure ($\text{La}_{2/3}\text{Ba}_{1/3}\text{MnO}_3/\text{DyBa}_2\text{Cu}_3\text{O}_7$) in [1]. An increase in the ferromagnet polarization, on the one hand, increases the subgap contribution to the conductance due to the localized Andreev state through a decrease in the localized state width (see Eqs. (19)); on the other hand, it reduces the number of Cooper pairs that are formed at the F/S interface and use the aforementioned state for the resonance penetration into the depth of the HTSC. The level itself makes a contribution to the conductance that decreases with increasing temperature for all polarization values excluding $\delta = 0$. Thus, from the dependence of the conductance $\sigma_{F/S}$ on the applied voltage, it is possible to identify the symmetry of the order parameter ($d_{x^2-y^2}$ or s in the case under consideration) if one of the electrodes is represented by a ferromagnet with $0.5 > \delta > 0.1$. As the strength of the potential barrier increases, the upper limit of this inequality moves toward unity.

Thus, in this paper, the ballistic conductance of an F/HTCS point contact was calculated for arbitrary spin-dependent transmission coefficients and the width of the localized Andreev state level was determined. It was found that the presence of a spin-dependent potential barrier cannot lead to the splitting of the localized Andreev state without the inclusion of the effect of induced magnetization on the energy spectrum of the HTCS. The possibility of identifying a d -type superconductor by the shape of the voltage dependence of the conductance characterizing its point contact with a ferromagnet when the contact has a metallic conduction has been analyzed.

I am grateful to G.B. Teitel'baum for discussing the results of this work. The work was supported by the

Russian Foundation for Basic Research, project no. 03-02-17432.

REFERENCES

1. V. A. Vas'ko, K. R. Nikolaev, V. A. Larkin, *et al.*, Appl. Phys. Lett. **73**, 844 (1998).
2. Z. W. Dong *et al.*, Appl. Phys. Lett. **71**, 1718 (1997).
3. Z. Y. Chen, A. Biswas, I. Zutic, *et al.*, Phys. Rev. B **63**, 212508 (2001).
4. G. Prinz, J. Magn. Magn. Mater. **200**, 57 (1999).
5. R. J. Soulen, J. M. Byers, M. S. Osofsky, *et al.*, Science **282**, 85 (1998).
6. V. V. Ryazanov, V. A. Oboznov, A. Yu. Rusanov, *et al.*, Phys. Rev. Lett. **86**, 2427 (2001).
7. D. J. Van Harlingen, Rev. Mod. Phys. **67**, 515 (1995).
8. C. C. Tsuei and J. R. Kirtley, Rev. Mod. Phys. **72**, 969 (2000).
9. C. R. Hu, Phys. Rev. Lett. **72**, 1526 (1994).
10. Y. Tanaka and S. Kashiwaya, Phys. Rev. Lett. **74**, 3451 (1995).
11. M. Sigrist, D. B. Bailey, and R. B. Laughlin, Phys. Rev. Lett. **74**, 3249 (1995).
12. M. Matsumoto and H. Shiba, J. Phys. Soc. Jpn. **64**, 3384 (1995); **65**, 4867 (1995).
13. M. Covington, M. Aprili, E. Paraoanu, and L. H. Greene, Phys. Rev. Lett. **79**, 277 (1997).
14. I. Zutic and O. T. Valls, Phys. Rev. B **60**, 6320 (1999).
15. J. X. Zhu, B. Friedman, and C. S. Ting, Phys. Rev. B **59**, 9558 (1999).
16. S. Kashiwaya, Y. Tanaka, N. Yoshida, and M. R. Beasley, Phys. Rev. B **60**, 3572 (1999).
17. I. Zutic and O. T. Valls, Phys. Rev. B **61**, 1555 (2000).
18. G. E. Blonder, M. Tinkham, and T. M. Klapwijk, Phys. Rev. B **25**, 4515 (1982).
19. K. Xia, P. J. Kelly, G. E. W. Bauer, and I. Turek, Phys. Rev. Lett. **89**, 166603 (2002).
20. B. P. Vodopyanov and L. R. Tagirov, Pis'ma Zh. Éksp. Teor. Fiz. **77**, 153 (2003) [JETP Lett. **77**, 126 (2003)].
21. Yu. S. Barash and I. V. Bobkova, Phys. Rev. B **65**, 144502 (2002).
22. A. V. Zaitsev, Zh. Éksp. Teor. Fiz. **86**, 1742 (1984) [Sov. Phys. JETP **59**, 1015 (1984)].
23. T. Löfwander, V. S. Shumeiko, and G. Wendin, Supercond. Sci. Technol. **14**, 53 (2001).
24. Yu. S. Barash, A. V. Galaktionov, and A. D. Zaikin, Phys. Rev. B **52**, 665 (1995).
25. M. B. Wolker and P. Pairor, Phys. Rev. B **59**, 1421 (1999).
26. Yu. S. Barash, Phys. Rev. B **61**, 678 (2000).
27. A. G. Aronov, Pis'ma Zh. Éksp. Teor. Fiz. **24**, 37 (1976) [JETP Lett. **24**, 32 (1976)].
28. T. Tokuyasu, J. A. Sauls, and D. Rainer, Phys. Rev. B **38**, 8823 (1988).
29. M. J. M. de Jong and C. W. J. Beenakker, Phys. Rev. Lett. **74**, 1657 (1995).

Translated by E. Golyamina

Spin-Dependent Electron Localization in Crystals

L. I. Magarill* and A. V. Chaplik

Institute of Semiconductor Physics, Siberian Division, Russian Academy of Sciences, Novosibirsk, 630090 Russia

*e-mail: levma@isp.nsc.ru

Received January 11, 2005

The possibilities of spatially localizing spin-polarized electrons in two-dimensional and three-dimensional systems due to spin-orbit interaction are studied theoretically. Using simple one-dimensional potentials as examples, it is demonstrated that electrons with a definite helicity can be localized so that carrier separation by spin is accomplished. The magnetic field effect is studied, and it is shown that the position of bound levels depends substantially on this effect. © 2005 Pleiades Publishing, Inc.

PACS numbers: 71.70.Ej, 73.50.Jt, 73.63.Hs

The recent years have been characterized by growing interest in the group of phenomena in low-dimensional systems belonging to the field known as spintronics. The main idea of the program of these investigations can be expressed by the words: “spin instead of charge.” That is, the idea is to search for various ways of controlling the spin degree of freedom of mobile carriers. Hopes for the advent of new solid-state electronic devices and new applications of such devices primarily to quantum computing are pinned on this area of investigations. It is clear that, on this path, it is necessary to learn how to induce spin polarization in an electron system and directionally affect carriers with a definite spin projection or, more precisely, with a given helicity. In addition to the evident possibility of polarizing electrons through the absorption of a circularly polarized electromagnetic wave, spin polarization by a static electric field (or direct current) through spin-orbit (SO) interaction [1–3], the spin-galvanic effect [4], and spin-dependent electron tunneling through a barrier [5] were considered.

In this work, we examine the possibility of the occurrence of a spatially localized state with only one definite spin projection; more simply, we search for situations in which, for example, a spin-up electron is bound and a spin-down electron is free. There are many such cases in atomic physics, where exchange interaction is responsible for spin separation. The simplest example is given by negative ions of alkalis and halogens: the spin of the excessive electron must compensate for the spin of the atomic electron shell. However, we will consider a one-particle problem, and the different behaviors of electrons differing in helicity will be caused by SO interaction. We will consider successively 2D and 3D cases and will also elucidate the magnetic field effect on localized and delocalized states.

1. Two-dimensional system. Rashba Hamiltonian. An electron gas in an oriented two-dimensional system (the unit vectors \mathbf{n} and $-\mathbf{n}$ perpendicular to the

system plane are not equivalent) is described by the Rashba Hamiltonian [6, 7]

$$\hat{H} = p^2/2m + \alpha(\boldsymbol{\sigma}[\mathbf{p} \times \mathbf{n}]), \quad (1)$$

where $\hat{\mathbf{p}} = (\hat{p}_x, \hat{p}_y)$ is the 2D electron momentum operator, $\boldsymbol{\sigma}$ are the Pauli matrices, α is the effective SO coupling constant, and $\hbar = 1$ is taken. Consider the situation when the system possesses a one-dimensional potential well of the form $U(x) = -U_0\delta(x)$. Our task is to find bound states. We will seek a solution of the Schrödinger equation $(\hat{H} + U)\Psi = E\Psi$ in the form

$$\Psi(x, y) = \frac{e^{ip_y y}}{\sqrt{L}} \begin{pmatrix} \psi_1(x) \\ \psi_2(x) \end{pmatrix}. \quad (2)$$

Here, L is the normalization size of the system in the y direction. The $\psi_{1,2}$ spinor components obey the system of equations

$$\begin{aligned} -\frac{1}{2m}\psi''_{1,2} + \alpha p_y \psi_{2,1} \pm \alpha \psi'_{2,1} - U_0\delta(x)\psi_{1,2} \\ = \left(E - \frac{p_y^2}{2m}\right)\psi_{1,2}, \end{aligned} \quad (3)$$

where the prime designates differentiation with respect to x . A solution of system (3) is given by a superposition of exponentials vanishing at $|x| \rightarrow \infty$

$$\begin{aligned} \psi_{1,2}(x) &= A_{1,2}^+ e^{-\xi_+ x} + A_{1,2}^- e^{-\xi_- x} \quad (x > 0), \\ \psi_{1,2}(x) &= B_{1,2}^+ e^{\xi_+ x} + B_{1,2}^- e^{\xi_- x} \quad (x < 0), \end{aligned} \quad (4)$$

where

$$\xi_{\pm} = \sqrt{-(2m\varepsilon + 2k^2) \pm 2|k|\sqrt{2m\varepsilon + k^2 + p_y^2}}. \quad (5)$$

Here $\varepsilon = E - p_y^2/2m$ and $k = m\alpha$. It is easy to verify that the real part of the exponents ξ_{\pm} are positive for $\varepsilon < -|p_y k|/m$ at $|p_y| > |k|$ and for $\varepsilon < -(k^2 + p_y^2)/2m$ at $|p_y| < |k|$.

The coefficients in Eq. (4) can be found from the continuity condition for the wave function at the point $x = 0$ and the condition for its derivative at this point

$$\begin{aligned} \Psi_{1,2}(+0) &= \Psi_{1,2}(-0); \\ \Psi'_{1,2}(+0) - \Psi'_{1,2}(-0) + 2U\Psi_{1,2}(0) &= 0, \end{aligned} \quad (6)$$

where $U \equiv mU_0$. This yields a system of eight equations for the coefficients $A_{1,2}^{\pm}$ and $B_{1,2}^{\pm}$. The spectrum of localized states is determined from the condition that the determinant of this system vanishes. The determinant is given by the expression

$$\begin{aligned} D &= 16(2m\varepsilon + p_y^2)([U^2 - (\xi_+ + \xi_-)U] \\ &\times (m\varepsilon + p_y^2 - \sqrt{(m\varepsilon)^2 - p_y^2 k^2}) + 2(2m\varepsilon + k^2 + p_y^2) \\ &\times \sqrt{(m\varepsilon)^2 - p_y^2 k^2}). \end{aligned} \quad (7)$$

The function $D(\varepsilon)$ has a root $\varepsilon = -p_y^2/2m$, which does not depend on the δ -potential strength, and another root $\varepsilon = -(k^2 + p_y^2)/2m$ at $|p_y| > |k|$. An analysis shows that these roots are spurious. If $\varepsilon = -p_y^2/2m$ is chosen, two of the eight constants $A_{1,2}^{\pm}$ and $B_{1,2}^{\pm}$ introduced above turn out to be zero. In this case, the number of matching conditions becomes greater than the number of constants remaining free. In the case of the second spurious root, roots of the characteristic equation are degenerate. Constructing a solution by the corresponding rule, we see that the resulting determinant of the system of equations for the coefficients of linearly independent solutions does not equal zero at $\varepsilon = -(k^2 + p_y^2)/2m$. The roots under discussion can become actual ones only under certain relations between the parameters p_y , U , and k of the problem. It may be shown that the satisfaction of these relations simply corresponds to an intersection of branches of the spectrum of localized states and the parabolas $-p_y^2/2m$ and $-(p_y^2 + k^2)/2m$.

Figure 1 demonstrates the numerical results for the subbands of localized states $\varepsilon_{\pm 1}(p_y) = \varepsilon_{\pm 1}(-p_y)$ at various values of the SO coupling parameter k . It is evident that the upper branch of the spectrum terminates at certain values of the momentum $p_y = \pm p_c$. This occurs when ε_{+1} reaches a value of $-p_c |k|/m$. In this case, ξ_{\pm} is equal to zero, and the corresponding wave function becomes

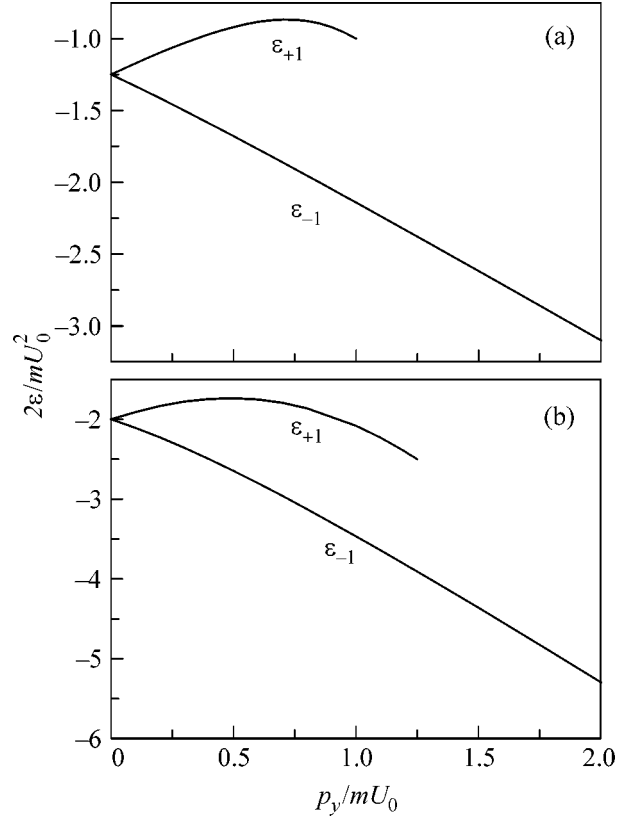


Fig. 1. Behavior of localized states as functions of p_y for $\alpha =$ (a) $0.5U_0$ and (b) U_0 .

delocalized. It is easy to find the following explicit expression for p_c :

$$p_c = \frac{U^2 + 4k^2}{4|k|}. \quad (8)$$

For a given U , p_c reaches its minimum value equal to U at $|k| = U/2$.

Figure 2 presents dependences of $\varepsilon_{\pm 1}$ on k at a fixed momentum p_y . Thus, the negative energy level of a δ -shaped 1D well in a spinless problem is split by the SO interaction. This effect, as it must, depends essentially on the momentum p_y of the free motion along the y axis and vanishes at $p_y = 0$. There is a critical momentum p_c such that only electrons of one definite helicity remain bound in the well when $|p_y| > p_c$.

2. Three-dimensional system. Dresselhaus Hamiltonian. In this section, we consider the electron gas in a bulk noncentrosymmetric III–V semiconductor with the SO interaction in the presence of a one-dimensional δ -function well $-U_0\delta(z)$. Such a system is described (in the coordinate system referenced to the

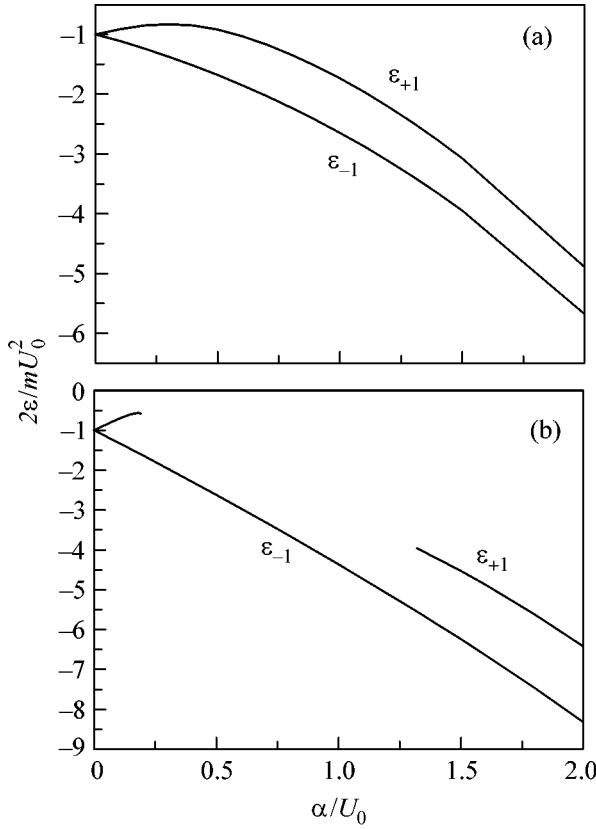


Fig. 2. Energies of localized states vs. the SO coupling constant for the momentum $p_y =$ (a) $0.5mU_0$ and (b) $1.5mU_0$. Localized states are absent in the discontinuity region in Fig. 2b.

principal crystal axes) by the Hamiltonian of the form [7, 8]

$$\hat{H} = \frac{\mathbf{p}_{\parallel}^2}{2m} + \frac{p_z^2}{2m} + \gamma[(\sigma_y p_y - \sigma_x p_x)p_z^2 + \sigma_z(p_x^2 - p_y^2)p_z + \sigma_x p_x p_y^2 - \sigma_y p_y p_x^2] - U_0 \delta(z), \quad (9)$$

where $\mathbf{p}_{\parallel} = (p_x, p_y)$. The part of the Hamiltonian cubic in the momentum corresponds to the SO interaction and is characterized by the effective band parameter γ . It should be noted that the cubic terms in Eq. (9) are much smaller than the quadratic ones. We seek a solution in the form

$$\Psi(\mathbf{r}) = \frac{e^{i\mathbf{p}_{\parallel}\mathbf{r}_{\parallel}}}{\sqrt{S}} \begin{pmatrix} \psi_1(z) \\ \psi_2(z) \end{pmatrix}, \quad (10)$$

where S is the normalization area of the system in the (x, y) plane and $\mathbf{r}_{\parallel} = (x, y)$. The $\psi_{1,2}$ functions obey the system of equations

$$-\psi''_{1,2} + 2m\gamma p_{\pm} \psi''_{2,1} \mp i2m\gamma(p_x^2 - p_y^2)\psi'_{1,2} \pm i2m\gamma p_x p_y p_{\mp} \psi'_{2,1} - 2mU_0 \delta(z)\psi_{1,2} = 2m\epsilon\psi_{1,2}, \quad (11)$$

where now the prime designates differentiation with respect to z , $\epsilon = E - p_{\parallel}^2/2m$, and $p_{\pm} = p_x \pm ip_y$. The $\psi_{1,2}$ functions must obey conditions similar to (6)

$$\begin{aligned} \psi_{1,2}(+0) &= \psi_{1,2}(-0); \\ \psi'_{1,2}(+0) - \psi'_{1,2}(-0) + 2U\psi_{1,2}(0) \\ + 2m\gamma p_{\pm}[\psi'_{2,1}(+0) - \psi'_{2,1}(-0)] &= 0. \end{aligned} \quad (12)$$

The characteristic equation for system (3) has the form

$$\begin{aligned} (\lambda^2 + 2m\epsilon)^2 + 4m^2\gamma^2[\lambda^2(p_x^2 - p_y^2)^2 - p_{\parallel}^2\lambda^4 \\ - p_x^2 p_y^2 p_{\parallel}^2 - 4p_x^2 p_y^2 \lambda^2] = 0. \end{aligned} \quad (13)$$

Consider first the case $p_x = p_y = p_{\parallel}/\sqrt{2}$. In this case, Eq. (13) has the roots

$$\lambda_{1,2} = \pm \sqrt{\frac{-4m\epsilon + \delta p_{\parallel}^2}{2(1 - \delta)}} \equiv \pm \xi_{+}, \quad (14)$$

$$\lambda_{3,4} = \pm \sqrt{\frac{-4m\epsilon - \delta p_{\parallel}^2}{2(1 + \delta)}} \equiv \pm \xi_{-}. \quad (15)$$

Here, $\delta = 2m\gamma p_{\parallel} \ll 1$, which corresponds to the smallness of the cubic term mentioned above. At $\epsilon < 0$ and $|\epsilon| > p_{\parallel}^2 \delta/4m$, the roots of the characteristic equation are real. Localized states should be sought similar to Eq. (4). For the coefficients $A_{1,2}$ and $B_{1,2}$, we again obtain a system of equations. The spectrum is determined from the condition that the determinant of this system equals zero. The roots of the determinant are found analytically, and we obtain

$$\epsilon_{\pm 1}(p_{\parallel}) = \frac{2(mU_0)^2 + p_{\parallel}^2(\delta^2 \mp \delta)}{4m(1 \mp \delta)} \quad (16)$$

for two subbands. The ϵ_{-1} subband for all p_{\parallel} values corresponds to a localized state, whereas the ϵ_{+1} subband describes localized states only when $\epsilon_{+1} < -\delta p_{\parallel}^2/2$, because otherwise ξ_{-} becomes imaginary. Thus, the upper branch has a termination point, which is determined by the equation

$$4m\gamma^2 p_{\parallel}^4 - 2\gamma p_{\parallel}^3 + mU_0^2 = 0. \quad (17)$$

Taking into account that $\delta = 2m\gamma p_{\parallel}$ is small, we find the following expression for the longitudinal momentum at the termination point:

$$p_{\parallel}^c = (mU_0^2/2\gamma)^{1/3}. \quad (18)$$

Note that the condition $2m p_{\parallel}^c \gamma \equiv (2m^2\gamma U_0)^{2/3} \ll 1$ must be satisfied and p_{\parallel}^c must obviously be much smaller than the Brillouin momentum.

When the longitudinal momentum is directed along a cube edge [e.g., $\mathbf{p}_{\parallel} = (p_{\parallel}, 0)$], an analysis shows that

the bound level in the δ well is weakly split but the termination point is absent and delocalization does not occur.

The 3D problem is solved quite simply if the approximation proposed in [5] is used: $p_{\parallel} \ll |p_z|$, where p_z is the imaginary momentum of the bound electron. In this approximation, only the first term is retained in the SO interaction in the Hamiltonian (9). The resulting Hamiltonian is diagonalized by the spinors of the form

$$\begin{pmatrix} \Psi_1(z) \\ \Psi_2(z) \end{pmatrix} = \chi_{\mu}(z) \begin{pmatrix} 1 \\ -\mu e^{-i\phi} \end{pmatrix} \frac{1}{\sqrt{2}}, \quad (19)$$

where $\mu = \pm 1$ is the helicity, and ϕ is the polar angle of the \mathbf{p}_{\parallel} vector. In this case, two independent 1D equations arise for the $\chi_{\mu}(z)$ functions

$$[-d^2/dz^2 + 2m_{\mu}U(z)]\chi_{\mu} = 2m_{\mu}\varepsilon\chi_{\mu}, \quad (20)$$

and two different effective masses correspond to the two helicities

$$\frac{1}{m_{\mu}} = \frac{1}{m}(1 + \mu\delta), \quad (\delta \ll 1). \quad (21)$$

One may try to obtain spin separation in, for example, the structure $\text{Ga}_x\text{Al}_{1-x}\text{As}/\text{A}_3\text{B}_5/\text{Ga}_y\text{Al}_{1-y}\text{As}$. Such a ‘‘sandwich’’ is described in the band diagram by a non-symmetrical rectangular well, which (as distinct from a symmetric one) may have no bound state. Therefore, by selecting band discontinuities that depend on the concentrations x and y at a given γ , it is possible to achieve the localization of particles of only definite helicity in the inner part of the heterostructure. It is well known that the first discrete level for an electron with mass m_{μ} appears in such a well under the condition

$$\sqrt{2m_{\mu}a^2U_2} > \arctan\left(\sqrt{\frac{U_1 - U_2}{U_2}}\right), \quad (22)$$

where $U_{1,2}$ are the heights of the well walls ($U_1 > U_2$) and a is the well width. From Eq. (22), it may be concluded that, if the inequalities

$$\begin{aligned} \sqrt{2ma^2U_2}\left(1 + \frac{\delta}{2}\right) &> \arctan\left(\sqrt{\frac{U_1 - U_2}{U_2}}\right) \\ &> \sqrt{2ma^2U_2}\left(1 - \frac{\delta}{2}\right) \end{aligned} \quad (23)$$

are satisfied, only an electron with the helicity $\mu = -1$ is localized.

Consider another example of two δ wells spaced at a distance a from each other: $U(z) = -U_0[\delta(z) + \delta(z - a)]$. Solving Eq. (20), we obtain the dispersion relation

$$(\kappa_{\mu} - m_{\mu}U_0)^2 = (m_{\mu}U_0)^2 e^{-2\kappa_a}, \quad (24)$$

where $\kappa_{\mu} = \sqrt{-2m_{\mu}\varepsilon}$. It follows from Eq. (24) that, under the condition

$$mU_0a(1 - \delta) < 1 < mU_0a(1 + \delta), \quad (25)$$

two localized states exist for the helicity $\mu = -1$, whereas only one localized state exists for the other helicity value.

3. Magnetic field effect. As evident from the geometry of the problems under consideration, it is reasonable to investigate the case of \mathbf{B}_{\parallel} , that is, a field parallel to the surface or to the plane $z = 0$ in the 3D problem. In the case of \mathbf{B}_{\perp} , particles are localized in the plane even without an additional lateral potential (e.g., in the representation of a given momentum). This case is beyond the scope of this work.

In the 3D problem with the Dresselhaus Hamiltonian, the field \mathbf{B}_{\parallel} significantly changes the orbital motion of electrons. Therefore, the Zeeman contribution can be disregarded (if the g factor is small). On the contrary, in the two-dimensional case, \mathbf{B}_{\parallel} affects only the Zeeman contribution to the system energy.

The general case (arbitrary fields and an arbitrary longitudinal momentum) involves rather cumbersome calculations. Being interested here only in the qualitative aspects of the problem, we will again consider the approximation [5] $p_x l, p_y l \ll 1$, where l is the wave function localization length along the z axis, and, in addition, we will consider not too strong magnetic fields such that $l \ll L$, where $L = \sqrt{c/eB_{\parallel}}$ is the magnetic length. Then, we arrive at the following system of equations for the spinor components $\Psi_{1,2}$ (the vector potential gauge is selected so that $A_y = -B_{\parallel}z, A_x = A_z = 0$):

$$\begin{aligned} \left[-\frac{d^2}{dz^2} + \left(p_y - \frac{z}{L^2}\right)^2 + U(z)\right]\Psi_{1,2} \\ + 2m\gamma\left[p_{\pm}\frac{d^2}{dz^2} \mp i\frac{1}{L^2}\frac{d}{dz}\left(z\frac{d}{dz}\right)\right]\Psi_{2,1} = 2m\varepsilon\Psi_{1,2}, \end{aligned} \quad (26)$$

where $\varepsilon = E - p_x^2/2m$. Owing to the assumptions made above, the last term on the left-hand side of Eq. (26) may be treated as a small perturbation. However, it is convenient here to include $p_{\pm}d^2/dz^2$ into the main part of the Hamiltonian so that the perturbation operator comprises only one term

$$\hat{V}_{\text{pert}} = \frac{\gamma}{L^2}\delta_y\frac{d}{dz}\left(z\frac{d}{dz}\right). \quad (27)$$

We again consider the model $U(z) = -U_0\delta(z)$. The unperturbed part of the Hamiltonian is diagonalized using spinors given by Eq. (19). The functions $\chi_{\mu}(z)$ now satisfy the equation

$$\left[-\frac{d}{dz^2} + \left(p_y - \frac{z}{L^2}\right)^2 - U_0\delta(z)\right]\chi_{\mu} = 2m_{\mu}\varepsilon\chi_{\mu}. \quad (28)$$

Solutions of this equation are expressed in terms of the parabolic cylinder functions $D_{q_\mu}((z - z_0)\sqrt{2}/L_\mu)$ and $D_{q_\mu}(-(z - z_0)\sqrt{2}/L_\mu)$, where $q_\mu = (\varepsilon/\omega_c)\sqrt{m_\mu/m}$, $\omega_c = eB_\parallel/mc$, and $L_\mu = L\sqrt{m/m_\mu}$. At $U_0 = 0$, we immediately obtain the SO-split Landau spectrum

$$\varepsilon_{n,\mu} = \left(n + \frac{1}{2}\right)\omega_c\sqrt{\frac{m}{m_\mu}}. \quad (29)$$

Taking U_0 into account, we obtain the dispersion relation

$$\frac{\sqrt{\pi}}{\Gamma(-q_\mu)} = m_\mu L_\mu U_0 D_{q_\mu}(z_0\sqrt{2}/L_\mu) D_{q_\mu}(-z_0\sqrt{2}/L_\mu). \quad (30)$$

For the ground level $n = 0$ [still disregarding perturbation (27)], we obtain

$$\varepsilon_{0,\mu} = \omega_c\sqrt{\frac{m}{m_\mu}}\left[\frac{1}{2} - \frac{m_\mu L_\mu U_0}{\sqrt{\pi}}\exp\left(-\sqrt{\frac{m_\mu}{m}}(p_y L)^2\right)\right]. \quad (31)$$

Here, we used the fact that m_μ differs only slightly from m and set $q_\mu = 0$ for the ground state in the subscript of the $D_q(t)$ functions.

Finally, taking \hat{V}_{pert} into account, in the first order, we obtain

$$E_{0,\mu} = \frac{p_x^2}{2m} + \omega_c\sqrt{\frac{m}{m_\mu}} \times \left[\frac{1}{2} - \frac{m_\mu^{3/4} m^{1/4} L U_0}{\sqrt{\pi}}\exp\left(-\sqrt{\frac{m_\mu}{m}}(p_y L)^2\right)\right] - \mu\gamma\sqrt{\frac{m}{m_\mu}}\frac{p_y^2}{2p_\parallel L^2} \quad (32)$$

for the two lowest subbands. It is evident from Eq. (32) that the SO interaction makes two contributions to the splitting of the Landau subbands: one exponentially depending on the momentum p_y , and the other one linear in the longitudinal momentum p_\parallel .

Thus, as should be expected, a magnetic field favors the localization of a particle near a short-range defect, which is represented in this case by a δ -shaped well: both the D_{q_μ} functions decrease as their arguments increase. However, the localization radius and the particle energy depend essentially on the magnetic field, and these dependences are different for electrons differ-

ing in helicity. Hence, the corresponding occupation numbers are also different. Using this fact, the spin polarization in the system can be changed directionally.

The inclusion of the x -aligned magnetic field in the 2D system leads to a modification of the term with σ_x in Eq. (1): $\alpha\sigma_x p_y \rightarrow \sigma_x(\alpha p_y - g\mu_B B/2)$ (g is the g factor and μ_B is the Bohr magneton). Hence, it immediately follows that the spectrum of localized states in the presence of the magnetic field is given by the equation

$$E_\mu^{(B)}(p_x, p_y) = \frac{p_y^2}{2m} + \varepsilon_\mu(p_x, p_y - g\mu_B B/2\alpha), \quad (33)$$

where $\varepsilon_\mu(p_x, p_y)$ is determined by the solution of the problem in the absence of the magnetic field.

The case of $\mathbf{B} \parallel y$ when the characteristic equation for ξ_\pm becomes a complete fourth-order equation involves much more cumbersome calculations. We leave this problem for a more comprehensive analysis elsewhere.

We are grateful to M.V. Éntin for discussions and to V.L. Gurevich and V.I. Perel' for interest in our work. This work was supported by the Russian Foundation for Basic Research, by the Council of the President of the Russian Federation for Support of Young Russian Scientists and Leading Scientific Schools (project no. NSH-593.2003.2), and by the programs of the Russian Academy of Sciences and the Ministry of Education and Science of the Russian Federation.

REFERENCES

1. V. M. Edelstein, *Solid State Commun.* **73**, 233 (1990).
2. A. G. Aronov, Yu. B. Lyanda-Geller, and G. E. Pikus, *Zh. Éksp. Teor. Fiz.* **100**, 973 (1991) [*Sov. Phys. JETP* **73**, 537 (1991)].
3. A. V. Chaplik, M. V. Entin, and L. I. Magarill, *Physica E (Amsterdam)* **13**, 744 (2002).
4. S. D. Ganichev, E. L. Ivchenko, V. V. Bel'kov, *et al.*, *Nature* **417**, 153 (2002).
5. V. I. Perel, S. A. Tarasenko, I. N. Yassievich, *et al.*, *Phys. Rev. B* **67**, 201 304(R) (2003).
6. Yu. A. Bychkov and E. I. Rashba, *JETP Lett.* **39**, 78 (1984).
7. E. I. Rashba and V. I. Sheka, in *Landau Level Spectroscopy*, Ed. by G. Landwehr and E. I. Rashba (Elsevier, Amsterdam, 1991), p. 178.
8. G. Dresselhaus, *Phys. Rev.* **100**, 580 (1955).

Translated by A. Bagatur'yants

Thermoelectric Study of the Phase Transitions in Cerium at Ultrahigh Pressures from 0 to 20 GPa

S. V. Ovsyannikov, V. V. Shchennikov*, and B. N. Goshchitskii

*Institute of Metal Physics, Ural Division, Russian Academy of Sciences,
ul. S. Kovalevskoi 18, Yekaterinburg, 620219 Russia*

**e-mail: vladimir.v@imp.uran.ru*

Received December 29, 2004; in final form, January 12, 2005

The pressure dependences of the thermoelectric power S of Ce samples were measured at pressures P from 0 to 20 GPa in a synthetic diamond cell. The dependence of S on P was found to be nonmonotonic both in the region of transitions from the fcc (γ) phase to the modified fcc (α) phase followed by the transition to the body-centered monoclinic (α'') and the tetragonal (ϵ) phases at pressures of about 1, 5–6, and 12–15 GPa, respectively, and in the stability region of these phases. The thermoelectric power sign was found to be positive for all high-pressure Ce phases. The found $S(P)$ dependence was compared with the published computational data on the electronic structure of the cerium phases. Cerium was taken as an example to demonstrate the advantage of the thermoelectric studies over other methods of investigation of phase transitions. © 2005 Pleiades Publishing, Inc.

PACS numbers: 05.70.Fh, 62.50.+p, 72.20.Pa, 81.40.Vw

In rare-earth metals, the formation of crystal structures depends clearly either on the atomic number in the lanthanum series or on pressure [1–5]. Cerium is the first metal in the lanthanum series and has only one f electron in its electron shell. A change in the cerium electronic structure upon pressure-induced phase transitions and, in particular, the behavior of the f band are of great interest for understanding the general regularities in the formation of electronic structures of lanthanides and types of crystal lattices appearing in them at normal and higher pressures. For this reason, although the high-pressure phase transitions in cerium have been studied in numerous works [1–16], they are still being intensively studied both theoretically and experimentally by various transition methods [4, 13, 14].

Under normal conditions, cerium crystallizes in the fcc lattice ($Fm\bar{3}m$) [3–5]. The isostructural $\gamma \rightarrow \alpha$ transition [1–5] that occurs in cerium at room temperature and $P \approx 0.8$ GPa is accompanied by a noticeable (16–17%) change in volume. It is not yet fully understood and is one of the most intriguing phenomena. The transition was detected from the jumps in the volume and electrical resistance and from changes in the lattice constant and elastic modulus [1–15]. At higher pressures (5–7 GPa), further sequential phase transitions occur in the body-centered monoclinic α'' phase ($C2/m$) or the uranium α phase (distorted variants of the fcc lattice) and thereupon (at 12–17 GPa) in the body-centered tetragonal ϵ phase ($I4/mmm$) [3–5].

In the initial fcc structure, the electronic configuration of cerium is $4f^15d^16s^2$. Models in which only the charge or spin instability is taken into account cannot

account for the isostructural $\gamma \rightarrow \alpha$ transition in cerium [4, 9, 13]. In the first case, a $4f^1$ electron is localized in the initial phase and delocalized in the new phase and, hence, is involved in the bond formation. In the second model, the $4f^1$ electron is assumed to be localized in both phases, while the phase transition occurs due to the spin-fluctuation energy [4, 9, 13]. Indeed, in contrast to the α phase, antiferromagnetism was found in γ -Ce, in agreement with the relativistic band calculations showing that the f band in the initial cerium phase is split into two narrow bands with different spin polarizations [15]. Recent synchrotron and neutron studies have shown that the isostructural transition at 0.8 GPa in cerium is caused by the appreciable changes not only in the electronic and magnetic but also in the phonon subsystems [4].

Various methods for studying phase transitions detect changes in a certain (electron, phonon, or magnetic) subsystem. In cerium, strong changes in the first two subsystems occur even before the isostructural phase transition [1–4, 11, 13]. For instance, the compressibility [1], neutron diffraction, and ultrasonic [11, 13] data suggest that the bulk modulus in cerium is approximately halved prior to the phase transition, which correlates with the observed softening of the longitudinal phonon modes. An approximately twofold increase is also observed for the thermoelectric power [8] that characterizes the structure of the electron bands. A similar large change in the electrical resistivity of cerium (a decrease by half) occurs only upon the $\gamma \rightarrow \alpha$ phase transition, while, in the pressure range from 0 to 0.8 GPa, where both the elastic modulus and thermoelectric power change strongly, the resistivity

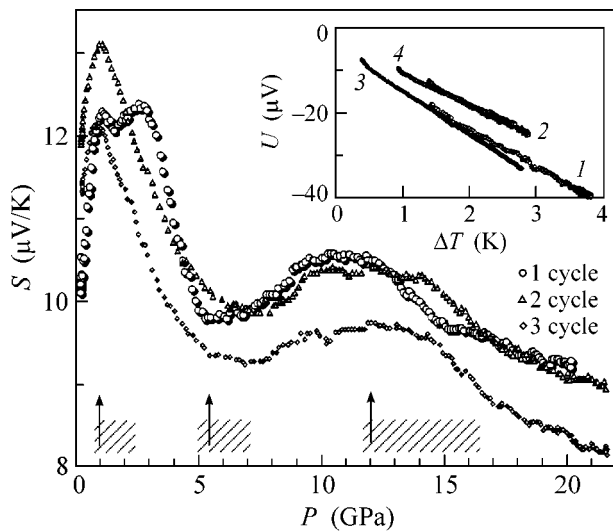


Fig. 1. Pressure dependence of the thermoelectric power S obtained for Ce sample no. 3 at $T = 293$ K in three consecutive cycles of an increase in pressure. The arrows indicate structural phase transitions, and the shaded regions correspond to the pressure ranges where these transitions are completed according to the data obtained in [1–15]. Inset: the thermoelectric signal vs. the temperature difference for the Ce samples: curves 1 and 3 are obtained at the beginning of the first and second cycles, respectively (at $P \approx 0$ GPa), and curves 2 and 4 are for the end of these cycles (at $P \approx 20.1$ and 21.6 GPa, respectively).

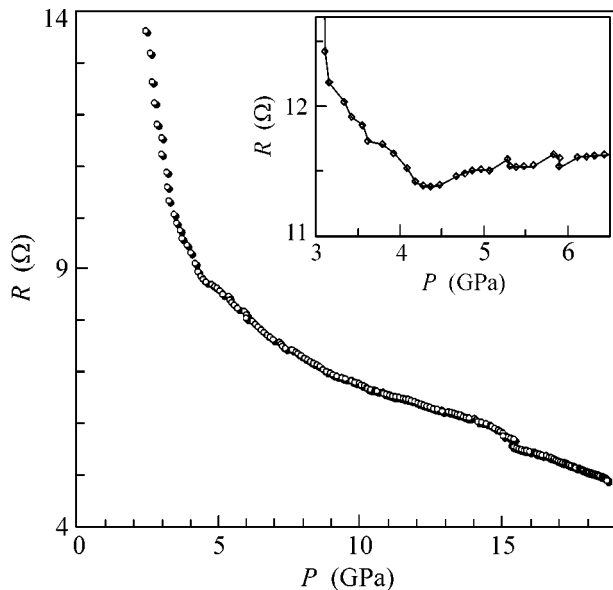


Fig. 2. Pressure dependence of the electrical resistance R obtained for a Ce sample at $T = 293$ K. Inset: the portion of the $R(P)$ curve obtained after subtracting the linear slope ($a \times P$), where $a = -0.596$ Ω/GPa .

increases only by about 5% [2, 4, 6–8]; i.e., it only slightly reflects the behavior of the electronic and crystal structures under pressure.

A method for studying phase transitions in semiconductors at high pressures up to 30 GPa was developed in [17–19]. This method also proved to be quite efficient for the detection of changes occurring in the electronic subsystems of metallic phases, in which the conductivity is caused by the charge carriers from several bands (e.g., electrons and holes) [18, 19]. We used this method to study phase transitions in the pressure range from 0 to 20 GPa for cerium, in which f , d , and s electrons can contribute to the conductivity [14]. The aim of this work was to perform thermoelectric measurements over a broad pressure range, where several structural modifications occur, so that one could compare the values of S and the corresponding pressure coefficients for each phase and gain qualitative information on the change in the electronic structure.

Cerium of type “ÉO” was studied. Structural certification of the material was carried out using an IVV-2M nuclear reactor by neutron diffraction analysis at the wavelength $\lambda = 1.532$ Å (see, e.g., [20]). The diffraction spectra corresponded to the fcc structure with the lattice constant $a = 1.1534 \pm 0.0004$ Å [15].

The dependences $S(P)$ and $R(P)$ of the thermoelectric power and electrical resistance, respectively, were measured for microsamples ($\sim 0.2 \times 0.2 \times 0.05$ mm) in conducting high-pressure synthetic diamond cells [17–19]. The alternative methods of studying thermoelectric power in a chamber with a compressible capsule [21] and in transparent diamond cells with implanted contacts [22] are as yet restricted by a hydrostatic pressure of 12 GPa. The pressure in the compressible spacer made from lithographic stone was determined using calibration graphs constructed by recording phase transitions in reference materials, ZnSe, CdTe, etc., with an error of about 10% [17–19]. To create the temperature gradient, one of the anvils was heated. The temperature at fixed anvil points was measured using thermocouples [17–19]. The procedure for measuring the quantities $S(P)$ and $R(P)$ was the same as in [17–19]. Measurements were made using an automated setup that allowed simultaneous recording of the pressure, temperature differences, thermoelectric signal, sample compression, and other parameters of the experiment [18, 19]. The errors in determining the $S(P)$ and $R(P)$ did not exceed 20 and 5%, respectively. The change in the sample volume upon compression was disregarded. The accuracy of determining the thermoelectric power was monitored by measurements performed for special purity grade lead, whose thermoelectric power $S \approx -1.27$ $\mu\text{V}/\text{K}$ is close to zero [23, 24].

The pressure dependence of the thermoelectric power of the Ce samples has a pronounced nonmonotonic character (Fig. 1) and reflects the changes occurring in their electronic structure. In the initial γ phase, S increases with P by a factor of 1.3–2 (Fig. 1). These

results are in agreement with the results obtained at hydrostatic pressures below 9 GPa [8]. The $S(P)$ dependence correlates with the behavior of the cerium electrical resistance $R(P)$ [1, 2, 4–8], but the thermoelectric power changes upon much stronger phase transitions (Figs. 1, 2, and [8]). Note that, in the majority of works where the electrical resistance of Ce was measured, the samples were preliminary deformed [1, 2, 4]. In the pressure ranges 1–2 and 5–6 GPa, where, according to the data from [3–5], the structural phase transitions occur, the thermoelectric power decreases (upon the first transition) or increases (upon the second transition) sharply (Fig. 1 and [8]). The transition at $P \geq 6$ GPa occurs presumably to the monoclinic body-centered phase α'' [3, 4, 25]. In [4], the effect of elastic stresses on the shift of phase-stability boundaries was considered in the framework of the group theoretical approach to demonstrate that the transition to the α uranium phase is energetically favorable at high temperatures in the samples without intrinsic elastic stresses, whereas the “cold” sample compression (as in our case) initiates transition to the monoclinic body-centered phase, which is confirmed by the experiment [4, 25]. Above 12 GPa, the sign of dS/dP changes and the thermoelectric power decreases with increasing pressure, while at $P \geq 15$ GPa, where the $R(P)$ curve also has kink (Fig. 2), S depends slightly on the pressure (Fig. 1). The change in the sign of the pressure coefficient for S at 12 GPa can be attributed to the onset of the phase transition to the tetragonal phase that is completed above 15 GPa, in accordance with the data of the synchrotron and x-ray studies [3, 5].

The general expressions for the electrical conductivity σ and thermoelectric power S have the form

$$\sigma = -\int \sigma(E) (\partial f / \partial E) dE, \quad (1)$$

$$S = -(k_0/e) \int [E - E_F] / k_0 T [\sigma(E) / \sigma] (\partial f / \partial E) dE.$$

Here, f is the distribution function, E_F is the Fermi energy, k_0 is the Boltzmann constant, e is the electron charge, T is the temperature, and E is the electron energy. In the case of metallic conductivity, Eq. (1) transforms to the well-known formula $S \approx -(k_0/e)(\pi^2/3)k_0 T [d \ln(\sigma(E)/dE)]|_{E=E_F}$ [23, 24, 26, 27].

In the low- and high-pressure cerium phases, s -, d -, and f -band electrons contribute to the total conductivity σ . These contributions are determined by the type of the electronic structure of the phases with different crystal lattices and depend on the charge-carrier mobility and the density of electronic states in the indicated bands [23, 24, 26, 27]. For instance, in a two-band metal with carriers from the s and d bands, $S \approx -(k_0/e)(\pi^2/3)k_0 T [3/2E_F - (1/(N_d(E))\partial N_d(E)/\partial E)]|_{E=E_F}$, where $N_d(E)$ is the density of states in the d band [23, 24, 26]. The second term in the square brackets is due to the electron scattering on the d -band carriers and strongly influences the thermoelectric power magni-

tude and sign [23, 24]. For a nearly empty d band, this expression accounts for the positive sign of the thermoelectric power [23, 24]. In cerium, there is also the near-empty f band where the main compression-induced changes occur [14], which manifested in the thermoelectric power behavior. According to Eq. (1), the conductivity is determined by the contribution from all the electron bands and, hence, changes slightly with pressure. Note that the signs of the pressure coefficients for the thermoelectric power and conductivity are opposite in the body-centered monoclinic structure above 6 GPa: S increases (Fig. 1 and [8]) while R decreases with increasing pressure [6–8].

The density of electronic states was calculated for different high-pressure cerium phases in [14]. It was found that the Fermi level in the α phase lies at the side of the van Hove peak in the density of states, while, in the other phases, it lies in the pseudogap region, which ordinarily corresponds to the higher structural stability. The density of states calculated in [14] for different bands near the Fermi level explains the strong pressure dependence of the cerium thermoelectric power (Fig. 1). In [14], the structural instability of cerium was explained by the degeneracy of the hybridized pdf states near the Fermi level and the transition was presumably attributed to the Peierls lattice distortion.

One can see from the data obtained in this work that, both upon the phase transitions and in the phase-stability regions, the cerium thermoelectric power, which is determined by s , d , and f electrons, is much more sensitive to a change in the electronic subsystem than electrical resistance. Earlier [28–32], it was shown that the thermoelectric power is highly sensitive to the pressure-induced electronic transitions in semiconductors, conducting ceramics, and other materials. This proves that the thermoelectric power method offers advantages over other methods for studying the phase transitions and electronic structure of high-pressure phases.

We are grateful to I.F. Berger and V.I. Voronin for the neutron-diffraction certification of the samples and to A.V. Mirmel'shtein for discussion of the results. This work was supported by the Russian Foundation for Basic Research (project no. 04-02-16178) and INTAS (grant no. 03-55-629).

REFERENCES

1. P. W. Bridgman, Proc. Am. Acad. Arts Sci. **81**, 165 (1952).
2. P. W. Bridgman, Proc. Am. Acad. Arts Sci. **79**, 149 (1951).
3. W. P. Holzapfel, Rep. Prog. Phys. **59**, 29 (1996).
4. V. P. Dmitriev, A. Y. Kuznetsov, O. Bandilet, *et al.*, Phys. Rev. B **70**, 014 104 (2004).
5. Y. K. Vohra, Physica B (Amsterdam) **190**, 1 (1993).
6. O. B. Tsiok and L. G. Khvostantsev, Zh. Éksp. Teor. Fiz. **120**, 1438 (2001) [JETP **93**, 1245 (2001)].

7. L. G. Khvostantsev and N. A. Nikolaev, *Phys. Status Solidi B* **114**, K135 (1982).
8. L. G. Khvostantsev and N. A. Nikolaev, *Phys. Status Solidi A* **77**, 161 (1983).
9. A. K. McMahan, *J. Less-Common Met.* **149**, 1 (1989).
10. G. Eliashberg and H. Capellman, *JETP Lett.* **67**, 125 (1998).
11. Z. Witczak and V. A. Goncharova, *Acta Mater.* **47**, 1565 (1999).
12. N. Richard and S. Bernard, *J. Alloys Compd.* **323–324**, 628 (2001).
13. I.-K. Jeong, T. W. Darling, M. J. Graf, *et al.*, *Phys. Rev. Lett.* **92**, 105702 (2004).
14. P. Ravindran, L. Nordstrom, R. Ahuja, *et al.*, *Phys. Rev. B* **57**, 2091 (1998).
15. E. Yu. Tonkov, *Phase Diagrams of Elements at High Pressure* (Nauka, Moscow, 1979) [in Russian].
16. S. V. Chernov, *Mat. Model.* **1**, 1 (1989).
17. I. M. Tsidil'kovskii, V. V. Shchennikov, and N. G. Gluzman, *Fiz. Tekh. Poluprovodn. (Leningrad)* **16**, 958 (1983) [*Sov. Phys. Semicond.* **16**, 604 (1983)].
18. S. V. Ovsyannikov and V. V. Shchennikov, *Pis'ma Zh. Éksp. Teor. Fiz.* **80**, 41 (2004) [*JETP Lett.* **80**, 35 (2004)].
19. S. V. Ovsyannikov, V. V. Shchennikov, and A. Misyuk, *Pis'ma Zh. Éksp. Teor. Fiz.* **80**, 459 (2004) [*JETP Lett.* **80**, 405 (2004)].
20. V. I. Voronin, V. V. Shchennikov, I. F. Berger, *et al.*, *Fiz. Tverd. Tela (St. Petersburg)* **43**, 2076 (2001) [*Phys. Solid State* **43**, 2165 (2001)].
21. L. G. Khvostantsev, L. F. Vereshchagin, and N. M. Uliyanitskaya, *High Temp. High Press.* **5**, 261 (1973).
22. D. A. Polvani, J. F. Meng, M. Hasegawa, *et al.*, *Rev. Sci. Instrum.* **70**, 3586 (1999).
23. R. D. Barnard, *Thermoelectricity in Metals and Alloys* (Taylor and Francis, London, 1972).
24. F. J. Blatt, P. A. Schroeder, C. L. Foiles, and D. Greig, *Thermoelectric Power of Metals* (Plenum, New York, 1976; Metallurgiya, Moscow, 1980).
25. M. I. McMahan and R. J. Nemes, *Phys. Rev. Lett.* **78**, 3884 (1997).
26. I. M. Lifshits, M. Ya. Azbel', and M. I. Kaganov, *Electron Theory of Metals* (Nauka, Moscow, 1971; Consultants Bureau, New York, 1973).
27. H. Fritzsche, *Solid State Commun.* **9**, 1813 (1971).
28. A. A. Averkin, M. P. Volotskiĭ, Zh. Zh. Zhaparov, and V. I. Kaĭdanov, *Fiz. Tekh. Poluprovodn. (Leningrad)* **6**, 538 (1972) [*Sov. Phys. Semicond.* **6**, 462 (1972)].
29. L. G. Khvostantsev, L. F. Vereshchagin, and E. G. Shulita, *High Temp. High Press.* **5**, 657 (1973).
30. V. F. Kraĭdenov and E. S. Itskevich, *Fiz. Nizk. Temp.* **18**, 1187 (1992) [*Sov. J. Low Temp. Phys.* **18**, 829 (1992)].
31. V. F. Kraĭdenov and E. S. Itskevich, *Fiz. Nizk. Temp.* **19**, 835 (1993) [*Low Temp. Phys.* **19**, 597 (1993)].
32. V. V. Shchennikov and S. V. Ovsyannikov, *Fiz. Tverd. Tela (St. Petersburg)* **45**, 590 (2003) [*Phys. Solid State* **45**, 619 (2003)].

Translated by V. Sakun

Plasma Oscillations in Fullerene Molecules during Electron Capture

R. F. Tuktarov*, R. F. Akhmet'yanov, E. S. Shikhovtseva,
Yu. A. Lebedev, and V. A. Mazunov

*Institute of the Physics of Molecules and Crystals, Ufa Scientific Center, Russian Academy of Sciences,
Ufa, 450075 Russia*

*e-mail: renatuk@anrb.ru

Received December 8, 2004; in final form, January 14, 2005

The anomalously wide energy range for the formation of long-lived negative molecular ions during electron capture by fullerene molecules is explained by the excitation of collective electron (plasma) oscillations in these molecules. A model for such excitations for fullerenes C_{60} and C_{70} is proposed on the basis of the Thomas–Fermi model. This model provides good correlation between the experimental curves of resonant electron capture and the theoretical energy dependences of the density of plasma oscillation modes. © 2005 Pleiades Publishing, Inc.

PACS numbers: 61.46.+w, 71.45.Gm

INTRODUCTION

In contrast to dissociative electron capture by polyatomic molecules, which is observed for the entire variety of organic compounds in the energy range 0–15 eV, nondissociative attachment of electrons leading to the formation of long-lived (mass-spectrometrically detected) negative molecular ions (NMIs) may occur either at thermal energies of electrons (SF_6^- [1, 2] and others) or at epithermal energies [3, 4] below 3–4 eV; at these energies, NMI peaks are observed simultaneously for several resonances.

At the same time, the first experiments on electron capture by C_{60} and C_{70} fullerene molecules [5–7] have already revealed an extremely wide electron energy range (0–15 eV) in which NMIs are formed in the gaseous phase. In this case, a narrow “thermal” resonance with a peak near 0 eV and a broad bell-shaped band with a complex structure and several local peaks are clearly observed (see, e.g., Fig. 1). Such a particular interaction of electrons with fullerenes (and some of their derivatives [8]) may be associated with the excitation of collective electron oscillations in fullerene molecules [9]. An incident excess electron spends its entire energy on exciting such plasma oscillations and, when its energy becomes close to zero, is captured by a molecule. A similar mechanism of the formation of long-lived NMIs for molecules is known as the Feshbach resonance with the electronic and/or vibrational excitation of a target molecule under the condition of positive electron affinity in the ground or electron-excited state [2]. However, the absolute values of energies in these two cases differ substantially: the energy of collective

electron excitations may be many times higher than the energy of the electronic and vibrational transitions.

It should be noted that experiments on electron impact [10–12] also revealed the excitation of collective electron oscillations, which is responsible for the dissociative ionization and fragmentation of neutral and charged fullerenes by high-energy (0.01–1 keV) electrons. The plasmon contribution in the effective cross section for the process was manifested in experi-

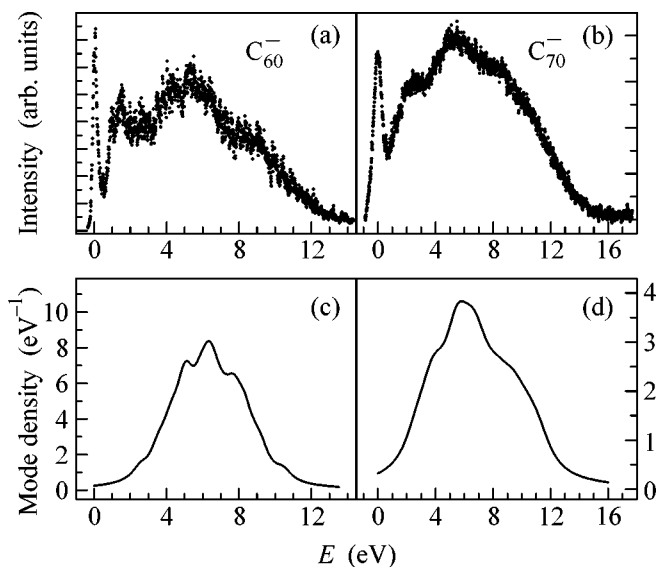


Fig. 1. Experimental curves for the effective yield of resonant electron capture (a) C_{60}^- and (b) C_{70}^- fullerene molecules, and (c) and (d) the respective distribution functions for plasma oscillation modes.

ments in the form of a structureless resonance band in the energy range 10–50 eV, whose position, shape, and width weakly correlated with the charge state of the fullerene ion and its mass [12]. At the same time, it is well known that the intensity and localization of this band must depend on the number of valence (collectivized) electrons in the fullerene molecule, while the band shape may be determined by the predominance of certain plasma modes manifested under various experimental conditions of their excitation [13]. Such a possibility of separating plasma modes in fullerenes can be realized in negative ion mass spectrometry when the excitation is executed by low-energy electrons through the mechanism of resonant electron capture [5, 7], which are “softer” than that in experiments on electron impact, where the energy resolution is relatively low.

This study is aimed at developing a quantitative model of plasma oscillations in fullerene molecules during electron capture that would take into account the geometrical parameters of the fullerene skeleton and the nonuniformity of the electron density distribution over the surface of the molecule. As a result, it would become possible to explain the experimental data on the resonant capture of electrons by C_{60} and C_{70} fullerenes on the basis of theoretical calculations of the distribution functions for plasma oscillation modes.

EXPERIMENT

The interaction of free fullerene molecules with electrons was studied experimentally using a laboratory negative ion mass spectrometer in the regime of resonant capture of electrons [7]. The idea of the method was described in detail in [2, 3] and, as applied to fullerenes, is as follows. A collimated C_{60} molecular beam generated due to sample heating (to 600–700 K) is fed to the ionization chamber where it perpendicularly intersects an energy-controlled electron beam (0–30 eV) whose energy distribution has an FWHM of no worse than 0.4 eV. Negative ions formed as a result of electron capture are mass selected by a static magnetic analyzer. The method implies the recording of so-called effective-yield curves, which describe the dependence of the ion current on the energy of ionizing electrons for all the negative ions formed in the process. The mass spectrum itself is the complete set of such curves. In contrast to the mass spectrum for other “ordinary” polyatomic molecules, the fullerene mass spectrum has a single peak of a molecular ion with the corresponding set of isotopic peaks. Typical experimental curves for the resonant capture of electrons by C_{60} and C_{70} fullerene molecules are shown in Figs. 1a and 1b.

MODEL

The simplest model applied to these objects is the hydrodynamic model of surface plasmons [14]. In this model, electrons are treated as a charged liquid on the surface of a fullerene molecule. If we consider that the

electron concentration N on the surface of the fullerene molecule does not change with increasing the number of carbon atoms (in the first approximation, the sizes of hexagons and pentagons can be regarded as constant), while the radius of the fullerene molecule is proportional to \sqrt{N} , the energy of surface plasmons in accordance with this model must be proportional to $N^{-1/4}$. The dependence of the energy range of the NMI formation on the number of atoms must be the same. Indeed, for C_n fullerene series, where $n = 60, 70, 76, 78, 84,$ and 90 , the peak of the high-energy resonance is shifted towards lower energies with increasing the number of atoms. However, the range of the formation of NMIs in this case increases from ~ 13 eV for C_{60} to ~ 20 eV for C_{90} . These differences in the position of the distribution peak and in the range of formation may be due to the fact that the model does not take into account the geometrical factors, which depend on the shape of the molecule as well as on the electron distribution over its surface (only the C_{60} molecule can be treated as spherical). Apparently, it is the disregard of the geometrical factors that complicates the application of the approaches [15, 16] for explaining the experimental data on the resonant capture of electrons even for C_{60} . In the model proposed below for the excitation of plasma oscillations in fullerene molecules, both the asphericity of the shape and the nonuniformity of the distribution of electrons over the surface are taken into account when describing the motion of the electron liquid in the field of the positively charged ions of the fullerene skeleton.

Our consideration is based on microscopic quantum hydrodynamics for fermions [17, 18]. It is known that the solution of systems of equations in quantum hydrodynamics may form an infinite chain of unclosed equations. Following [17, 18], we introduce the Thomas–Fermi model to close the systems of equations. In this case, the continuity and momentum balance equations take the form

$$\begin{aligned} \frac{\partial n(\mathbf{r}, t)}{\partial t} + \nabla(n(\mathbf{r}, t)\mathbf{v}(\mathbf{r}, t)) &= 0, \\ m_e \left(\frac{\partial}{\partial t} + \mathbf{v}(\mathbf{r}, t)\nabla \right) \mathbf{v}^\alpha(\mathbf{r}, t) & \\ + \nabla^\alpha(W(\mathbf{r}, t) - e\Phi(\mathbf{r}, t)) &= 0. \end{aligned} \quad (1)$$

Here, $\Phi(\mathbf{r}, t)$ is the total potential of the field of electrons and ions, \mathbf{v} is an analogue of the velocity in classical hydrodynamics, and $W(\mathbf{r}, t)$ is the energy in the Thomas–Fermi model. If we consider the surface electron density $\sigma(\mathbf{r}, t)$ rather than the volume electron density $n(\mathbf{r}, t)$, $W(\mathbf{r}, t)$ can be represented (disregarding the exchange and spin corrections) in the form

$$W(\mathbf{r}, t) = \frac{\hbar^2}{4\pi m_e} \sigma(\mathbf{r}, t). \quad (2)$$

In the stationary case ($v = 0$), system (1) is transformed into the Thomas–Fermi equation

$$W(\mathbf{r}) - e\Phi(\mathbf{r}) = 0. \quad (3)$$

Spherical fullerene C₆₀. We treat the C₆₀ molecule as a sphere with carbon ions rigidly fixed on its surface and having the coordinates $\theta_k, \varphi_k = \Omega_k$ ($d\Omega = \sin\theta d\theta d\varphi$). For the surface distribution of electrons, $n(\mathbf{r}, t) = \delta(\mathbf{r} - R)\sigma(\mathbf{r}, t)$ and solution of Eq. (3) in the stationary case has the form

$$\sigma_0(\Omega) = \sigma_0 + \frac{1}{R^2} \sum_{lm} \phi_{lm}^{60} \xi_l Y_{lm}(\Omega),$$

where $Y_{lm}(\Omega)$ is a Legendre spherical function and

$$\sigma_0 = \frac{N}{4\pi R^2}, \quad \phi_{lm}^{60} = \sum_{k=1}^N Y_{lm}^*(\Omega_k),$$

$$\xi_l = \left[1 + (2l+1) \frac{a_B}{4R} \right]^{-1},$$

where a_B is the Bohr radius. For nonstationary processes, the solution for the surface electron distribution density is sought in the form

$$\sigma(\Omega, t) = \sigma_0(\Omega) + \sum_{lm} \sigma_{lm}(t) Y_{lm}(\Omega),$$

where $\sigma_{lm}(t) = \sigma_{lm} e^{i\omega_{lm} t}$. Solutions of system (1) give the eigenfrequencies of plasma-type oscillations,

$$\omega_{lm}^2 = \omega_p^2 \frac{l(l+1)}{2l+1} 4\pi \lambda_m^{(l)}, \quad (4)$$

where $\lambda_m^{(l)}$ are the eigenvalues of the matrix

$$A_{m_1 m_2}^{(l)} = \frac{1}{N} \sum_{k=1}^N Y_{lm_1}(\Omega_k) Y_{lm_2}^*(\Omega_k)$$

for a certain l value. Expression (4) was derived under the condition that $\xi_l \sim 1$. This condition imposes a constraint in $l \ll 2R/a_B - 1/2 = L_{\max} \sim 11$. For $l > L_{\max}$, we obtain complex values for frequencies, which corresponds to the damping of plasma oscillations.

Spheroidal fullerene C₇₀. Let us consider a C₇₀ molecule in a spheroid (confocal, $c = \text{const}$ is the focus)

coordinate system $x = c\sqrt{(\mu^2 - 1)(1 - v^2)} \cos\varphi$, $y = c\sqrt{(\mu^2 - 1)(1 - v^2)} \sin\varphi$, $z = c\mu v$. For $\mu = \mu_0 = 1/\varepsilon$, we obtain $\varepsilon = 0.561$ and $R/c = 1.462$; i.e., the C₇₀ molecule has the spheroid shape, i.e., a sphere extended along the z axis with eccentricity ε . In the case of the surface distribution of electrons, the potentials of the fields of electrons and ions for $\mu = \mu_0$ have the form

$$\Phi^e(\mu_0, \Omega) = 8\pi e^2 c g(\mu_0)$$

$$\times \sum_{lm} \frac{(-1)^m}{2l+1} \sigma_{(0)lm}(\mu_0) \Theta_{lm}(\mu_0) Q_{lm}(\mu_0) Y_{lm}(\Omega),$$

$$\Phi^{\text{ion}}(\mu_0, \Omega) = \frac{8\pi e^2}{c} g(\mu_0)$$

$$\times \sum_{lm} \frac{(-1)^m}{2l+1} \phi_{lm}^{70} \Theta_{lm}(\mu_0) Q_{lm}(\mu_0) Y_{lm}(\Omega),$$

respectively. Here, e is the electron charge;

$$\Theta_{lm}(\mu_0) = \sqrt{\frac{2l+1}{2} \frac{(l-m)!}{(l+m)!}} P_{lm}(\mu_0),$$

$$Q_{lm}(\mu_0) = \sqrt{\frac{2l+1}{2} \frac{(l-m)!}{(l+m)!}} K_{lm}(\mu_0),$$

where $P_{lm}(\mu_0)$ and $K_{lm}(\mu_0)$ are the associated Legendre functions of the first and second kind, respectively;

$$\phi_{lm}^{70}(\mu_0) = \frac{1}{\sqrt{\mu_0^2 - 1}} \sum_{k=1}^{70} \frac{Y_{lm}^*(\Omega_k)}{\sqrt{\mu_0^2 - v_k^2}}$$

($Y_{lm}(\Omega) = \Theta_{lm}(v) \frac{e^{im\varphi}}{\sqrt{2\pi}}$, $\Omega = \langle v, \varphi \rangle$). The steady-state solution of Eq. (3) has the form

$$\sigma_0(\Omega) = \frac{1}{c} \sum_{lm} \phi_{lm}^{70}(\mu_0) \xi_{lm}(\mu_0) Y_{lm}(\Omega),$$

where

$$\xi_{lm}(\mu_0) = \left[1 + (2l+1) \frac{(-1)^m a_B}{8\pi e^2 c g(\mu_0) \Theta_{lm}(\mu_0) Q_{lm}(\mu_0)} \right]^{-1}.$$

For nonstationary processes, we seek the surface distribution of electrons in the form

$$\sigma(\Omega, t) = \sigma_0(\Omega) + \sum_{lm} \sigma_{lm}(\mu_0, t) Y_{lm}(\Omega),$$

where $\sigma_{lm}(\mu_0, t) = \sigma_{lm}(\mu_0) e^{i\omega_{lm} t}$. Undamped plasma-type oscillations can be determined from the solution of system (1) as

$$\omega_{lm}^2 = \omega_p^2 8\pi \left(\frac{R}{c} \right)^3 \left[l(l+1) + \frac{m^2}{\mu_0^2 - 1} \right] \times \frac{(-1)^m}{2l+1} \Theta_{lm}(\mu_0) Q_{lm}(\mu_0) A_{lm}(\mu_0). \quad (5)$$

Here,

$$A_{lm}(\mu_0) = \frac{1}{\sqrt{\mu_0^2 - 1}} \frac{1}{N} \sum_{k=1}^{70} \frac{|Y_{lm}(\Omega_k)|^2}{\sqrt{\mu_0^2 - \nu_k^2}}.$$

Expression (5) was derived under the condition that $\xi_{lm}(\mu_0) \sim 1$. Otherwise, solutions of system (1) are damped.

DISCUSSION

According to the model proposed above, the process of electron capture by the fullerene molecule can be described as follows. If the energy of the incident electron is equal or close to the energy of a certain plasma mode, it excites this mode, loses its energy, and is then captured with zero energy by the molecule. Each vibrational mode has its own energy distribution and the distribution functions may overlap. Consequently, the electron with a fixed energy can excite one of several possible modes. Obviously, the larger the number of different modes in a given energy range, the higher the probability of the NMI formation and, hence, the higher the intensity of a signal when recording the experimental curves of the effective ion yield.

To compare the experimental data with the results of calculations, it is necessary to plot the frequency (or energy) dependence $g(\omega)$ of the vibrational mode density for plasmons. To this end, it is necessary to numerically solve the system of equations (1), to obtain a set of eigenfrequencies ω_{lm} of oscillations, to replace them by Gaussians Γ with the standard deviation equal to the width of the electron distribution, and to sum over the entire energy range, $g(\omega) \approx \sum_{lm} \Gamma(\omega - \omega_{lm})$.

The results of numerical calculations of plasma oscillation mode density are presented in Figs. 1c and 1d together with the corresponding experimental curves for the resonant capture of electrons by molecules of C_{60} and C_{70} fullerenes. It is seen that these curves correlate: the ranges of NMI formation for both types of fullerenes, as well as the positions of the main peaks and other local singularities, coincide with each other. Some discrepancy between the experimental and theoretical curve is observed only in the low-energy range, especially for C_{60} (Fig. 1a). According to our calculations, the lowest energy of the vibrational mode for C_{60} is approximately equal to 2.55 eV. The cross section for the NMI formation is a nonlinear function of the electron energy: as the energy decreases, the time of the interaction between the electron and molecule (and, hence, the formation cross section) increases [1, 2], which leads to a relative increase in the density of low-energy plasma modes. The narrow peaks on the experimental curve in the range of thermal energies (≤ 2 eV) are associated with the presence of the so-called single-particle resonances [2] that do not belong to collective excitations and, hence, are ignored in our model.

The above general approach to studying collective vibrations of fullerenes is not limited to the C_{60} and C_{70} molecules. Higher fullerene molecules with substantial deviation from the spherical shape, as well as fluorinated and hydrogenated fullerenes, will be investigated experimentally and theoretically in our future works.

ACKNOWLEDGMENTS

The work of E.S.Sh. was supported by the Foundation for Support of Domestic Science. This work was supported by the Branch of General Physics and Astronomy, Russian Academy of Sciences (program "New Materials and Structures," contract no. 10002-251/OFN), and the Russian Foundation for Basic Research (project nos. 05-02-97902, 05-02-16450, and 05-03-32372).

REFERENCES

1. L. G. Christophorou and J. K. Olthoff, *J. Phys. Chem. Ref. Data* **29**, 267 (2000).
2. V. I. Khvostenko, *Mass-Spectrometry of Negative Ions in Organic Chemistry* (Nauka, Moscow, 1981), p. 159 [in Russian].
3. V. I. Khvostenko, V. A. Mazunov, V. S. Fal'ko, *et al.*, *Khim. Fiz.* **1**, 915 (1982).
4. Yu. V. Vasil'ev and V. A. Mazunov, *Pis'ma Zh. Éksp. Teor. Fiz.* **51**, 129 (1990) [*JETP Lett.* **51**, 144 (1990)].
5. M. Lezius, P. Scheier, and T. D. Mark, *Chem. Phys. Lett.* **203**, 232 (1993).
6. T. Jaffke, E. Illenberger, M. Lezius, *et al.*, *Chem. Phys. Lett.* **226**, 213 (1994).
7. Yu. V. Vasil'ev, R. F. Tuktarov, and V. A. Mazunov, *Rapid Commun. Mass Spectrom.* **11**, 757 (1997).
8. Yu. V. Vasil'ev, O. V. Boltalina, R. F. Tuktarov, *et al.*, *Int. J. Mass Spectrom. Ion Processes* **173**, 113 (1998).
9. C. Bulliard, M. Allan, and S. Leach, *Chem. Phys. Lett.* **209**, 434 (1993).
10. S. Matt, B. Dunser, M. Lezius, *et al.*, *J. Chem. Phys.* **105**, 1880 (1996).
11. D. Hathiramani, K. Aichele, W. Arnold, *et al.*, *Phys. Rev. Lett.* **85**, 3604 (2000).
12. P. Scheier, H. Deutsch, K. Becker, and T. D. Mark, *Int. J. Mass Spectrom.* **233**, 293 (2004).
13. L. G. Gerchikov, P. V. Efimov, V. M. Mikoushkin, and A. V. Solov'yov, *Phys. Rev. Lett.* **81**, 2707 (1998).
14. G. Barton and C. Eberlin, *J. Chem. Phys.* **95**, 1512 (1991).
15. G. F. Bertsch, A. Bulgak, D. Tomanek, and Y. Wang, *Phys. Rev. Lett.* **66**, 2690 (1991).
16. A. Bulgak and N. Ju, *Phys. Rev. B* **46**, 4297 (1991).
17. L. S. Kuz'menkov, S. G. Maksimov, and V. V. Fedoseev, *Teor. Mat. Fiz.* **126**, 136 (2001).
18. L. S. Kuz'menkov, S. G. Maksimov, and V. V. Fedoseev, *Teor. Mat. Fiz.* **126**, 258 (2001).

Translated by N. Wadhwa

Acoustic Modes in 2D Atomic Hydrogen on the Surface of Superfluid ^4He

A. I. Safonov

Russian Research Center Kurchatov Institute, pl. Akademika Kurchatova 1, Moscow, 123182 Russia

e-mail: safonov@issph.kiae.ru

Received January 18, 2005

Possible acoustic modes in a superfluid 2D gas of hydrogen atoms adsorbed on the surface of liquid helium at $T \lesssim 0.1$ K are considered depending on the oscillation frequency and times of energy and momentum transfers both between 2D subsystems of hydrogen atoms and riplons and into the bulk liquid or substrate. Analogues of the usual and second sounds are realized in 2D hydrogen at high frequencies. In the case of weak coupling with the bulk liquid and substrate, riplons provide an addition to the normal hydrogen component, which leads to a change in the speed of the second sound. In the most interesting range of low frequencies, an analogue of the fourth sound is realized, when riplons and the normal hydrogen component are immobile and only the superfluid hydrogen component moves. In this case, when the rate of heat transfer into the bulk liquid is much lower than the sound frequency, oscillations of the temperature of hydrogen can be observed in phase with density oscillations. Methods for exciting acoustic modes are discussed. © 2005 Pleiades Publishing, Inc.

PACS numbers: 03.75.Kk, 67.40.Pm, 67.65.+z, 68.03.Kn, 68.43.Pq

The two-dimensional superfluidity [1, 2] observed in helium films with a thickness of several atomic layers [3] must also take place in a Bose gas. One of the good examples of a 2D Bose gas with weak interaction is the gas of electron and nuclear spin-aligned hydrogen atoms that occupy the only bound state with an energy of $E_a = -1.14$ K in the absorption potential on the liquid-helium surface (2D $\text{H}\downarrow$). A high phase-space density of 2D $\text{H}\downarrow$ required for the observation of superfluidity can be reached, e.g., in a miniature magnetic trap [4]. In this case, it is, however, difficult to directly detect 2D $\text{H}\downarrow$. Wide opportunities for observing and studying the transport processes on the liquid-helium surface involving 2D $\text{H}\downarrow$ [5] are opened by experiments on the thermal compression of 2D hydrogen with direct diagnostics by ESR spectroscopy [6, 7]. Thus, the question of possible experimental manifestations of the superfluidity of 2D hydrogen arises. This question is a part of the more general problem of a 2D superfluid Bose gas on the surface of a superfluid Bose liquid.

First of all, in a superfluid gas it is natural to expect the appearance of several types of oscillations similar to the first (usual), second, etc., sounds. Acoustic modes on the helium surface involving 2D atomic hydrogen can be analyzed using quantum surface hydrodynamics. This approach ensures the transition from the microscopic consideration of capillary waves to the description in terms of the 2D gas of elementary excitations, riplons [8]. The features associated with the superfluidity of 2D $\text{H}\downarrow$ can be described in the framework of two-fluid hydrodynamics similarly to the bulk superfluid helium [9]. The difference is that normal

motion involves not only the normal hydrogen component but also riplons.

It is necessary to emphasize that the interaction of hydrogen with riplons leads to the formation of two types of mixed elementary excitations [10], which are combinations of riplons with hydrogen quasiparticles. Therefore, strictly speaking, hydrogen and riplons should be treated as hydrogen-like and ripplon-like excitations, respectively. The basic contribution to the interaction comes from the process of the emission or absorption of a ripplon by a hydrogen atom, where the atom in the initial or final state has zero momentum, i.e., is in a quasi-condensate. In the surface Hamiltonian, terms quadratic in the creation (annihilation) operators of riplons and above-condensate hydrogen quasiparticles correspond to this process. Terms of third and higher orders describe the relaxation processes responsible for the nonzero width of mixed terms and their interaction. The elementary-excitation spectra appreciably differ from the pure hydrogen and pure ripplon spectra when the initial terms are sufficiently close to each other. For the case under consideration, this condition corresponds to energies several times higher than thermal energy, whereas hybridization disappears in the long-wavelength limit. As a result, the real effect of hybridization on the thermodynamics and kinetics of the surface is insignificant [10].

Key quantities for the problems under consideration are the characteristic times of the transfer of the longitudinal momentum from the hydrogen system to riplons (τ_{HR}) and from riplons into the substrate or bulk liquid (τ_{R}). The τ_{HR} value was calculated in the Boltz-

mann limit by Zimmerman and Berlinsky [11]. It is natural to assume that the result for degenerate hydrogen can be significantly different and requires individual consideration. The rate of momentum transfer both from riplons to phonons of bulk helium and into the substrate was measured by Mantz *et al.* [12] and calculated in [13].

The relation between τ_{HR} and τ_{R} can be arbitrary, because the temperature dependences of the quantities differ from each other and τ_{R} depends on the character of the surface [13]. In particular, according to [11], τ_{HR} decreases from 6×10^{-7} to 10^{-8} s when the temperature increases from 40 to 150 mK. At the same time, τ_{R} for the film is nearly independent of the temperature for $T \lesssim 150$ mK [12] but depends strongly on the film thickness [13, 14] and the substrate roughness scale [13].

The hydrodynamic description of oscillations is obviously applicable only if the oscillation frequency is much lower than the frequencies of quasiparticles forming the 2D gas. The validity of this condition can easily be verified because the frequency $\Omega_T \sim T/\hbar \sim 10^{10} \text{ s}^{-1}$ of a thermal ripplon, as well as the elementary excitations in 2D H \downarrow , is sufficiently high.

Further, hydrodynamics is based on the assumption of local thermodynamic equilibrium, which we supplement with the assumption of the equilibrium of each of the individual subsystems. In turn, this means that the thermal equilibrium within a subsystem is established much faster than energy and momentum exchange with other subsystems and the thermostat (bulk liquid or substrate). Such an assumption is quite justified for 2D hydrogen. Indeed, in the free-particle limit, $T \gg mc^2$, where c is the speed of sound, the relaxation is determined by interatomic collisions. The frequency of elastic collisions between hydrogen atoms is equal to $\tau_{\text{HH}}^{-1} \approx \sigma \times 3.5 \times 10^{-4} \text{ cm}^2/\text{s}$ [5], which is much higher than τ_{HR}^{-1} over the entire density range under consideration. In the opposite, acoustic limit, $T \ll mc^2$, equilibrium in 2D H \downarrow is established due to interaction between phonons. The relaxation time due to the spontaneous decay of a phonon into two phonons, similar to the decay of phonons in superfluid helium, is estimated as $\tau^{-1} \sim \hbar k_T^4/m\sigma$ [15]. For the density $\sigma = 2 \times 10^{13} \text{ cm}^{-2}$ and temperature $T = 0.1 \text{ K}$, the wave vector of a thermal phonon is equal to $k_T = T/\hbar c = 3.2 \times 10^6 \text{ cm}^{-1}$; thereby, $\tau \sim 3 \times 10^{-10} \text{ s}$.

The thermal relaxation of riplons is likely caused by the $\text{R} \rightleftharpoons \text{R} + \text{R}$ process [16]. In the case of its inefficiency [17], it is more correct to consider the interaction of hydrogen with the thermostat *through* riplons and to determine the corresponding nonequilibrium distribution of riplons from the kinetic equation. Nevertheless, the thermodynamic description of riplons remains meaningful when $\tau_{\text{HR}} \ll \tau_{\text{R}}$ or $\tau_{\text{HR}} \gg \tau_{\text{R}}$. In these two important limiting cases, the distribution of

riplons remains thermal and their temperature and velocity coincide with, respectively, the temperature and velocity of the hydrogen or the substrate.

In view of the above discussion, the linearized transport equations for the 2D system are written omitting the dissipative terms responsible for longitudinal heat conduction, diffusion, and viscosity. The continuity equation for hydrogen [18] has the form

$$\dot{\rho}_{\text{H}} + \text{div} \mathbf{j}_{\text{H}} = 0. \quad (1)$$

Here, as usual, the dot over the symbol stands for the time derivative; $\mathbf{j}_{\text{H}} = \rho_n \mathbf{v}_n + \rho_s \mathbf{v}_s$ is the hydrogen flux, where \mathbf{v}_n (\mathbf{v}_s) and ρ_n (ρ_s) are the velocity and mass density of the normal (superfluid) components, respectively, and $\rho_{\text{H}} = m\sigma = \rho_n + \rho_s$ is the total density, where m is the hydrogen atomic mass.

The equation of motion for the normal hydrogen component has the form

$$\rho_n \dot{\mathbf{v}}_n + \nabla P_{\text{H}} + \frac{\rho_n}{\tau_{\text{HR}}} (\mathbf{v}_n - \mathbf{v}_{\text{R}}) = 0, \quad (2)$$

where P_{H} is the 2D hydrogen pressure, includes the momentum transfer from the hydrogen to riplons in the τ approximation, and the last term on the left-hand side should be treated as the formal definition of the corresponding time constant τ_{HR} .

The equation of motion for riplons including the momentum transfer into the substrate is similar:

$$\rho_{\text{R}} \dot{\mathbf{v}}_{\text{R}} + \nabla P_{\text{R}} - \frac{\rho_n}{\tau_{\text{HR}}} (\mathbf{v}_n - \mathbf{v}_{\text{R}}) + \frac{\rho_{\text{R}}}{\tau_{\text{R}}} \mathbf{v}_{\text{R}} = 0. \quad (3)$$

The equation of motion for the superfluid hydrogen component has the usual form

$$\dot{\mathbf{v}}_s + \nabla \mu_{\text{H}} = 0. \quad (4)$$

The specific chemical potential $\mu_{\text{H}} \approx \sigma \tilde{U}/m$ of hydrogen is determined primarily by H–H interaction, because under the superfluidity conditions $\sigma \Lambda^2 \gtrsim 7$ [19, 20], and, therefore, the thermal contribution to μ_{H} that is about $Te^{-\sigma \Lambda^2}$ is exponentially small (here, $\Lambda = \sqrt{2\pi \hbar^2/mT}$ is the thermal wavelength of the hydrogen atom and \tilde{U} is the mean-field parameter generally depending on the density [20]).

Heat transfer from hydrogen to riplons [11] and from riplons to the film bulk [21] is described by the following equations of energy conservation:

$$T_{\text{H}} (\dot{S}_{\text{H}} + \text{div} S_{\text{H}} \mathbf{v}_n) + K_{\text{HR}} (T_{\text{H}} - T_{\text{R}}) = 0, \quad (5)$$

$$T_{\text{R}} (\dot{S}_{\text{R}} + \text{div} S_{\text{R}} \mathbf{v}_{\text{R}}) - K_{\text{HR}} (T_{\text{H}} - T_{\text{R}}) + K_{\text{RP}} (T_{\text{R}} - T_0) = 0. \quad (6)$$

Here, T_0 is the temperature of the liquid in the film bulk and K_{HR} and $K_{\text{RP}} = 5.3T^{17/3} \text{ W cm}^{-2} \text{ K}^{-20/3}$ [21] are the heat conductivities of the hydrogen–rippion and ripplon–phonon contacts, respectively.

Assuming that deviations of the thermodynamic quantities from their steady values, as well as \mathbf{v}_n , \mathbf{v}_s , and \mathbf{v}_R , are small, excluding the velocities from Eqs. (1)–(6), and substituting the solution in the form of the plane wave $\exp(i\omega t - i\mathbf{k}\mathbf{r})$, we arrive at the system of three equations for the amplitudes of the oscillations of the hydrogen density ρ_{H} and temperatures T_{H} and T_{R} . The condition of the consistency of these three equations yields, as usual, the relation between the frequency ω and wave number k . However, this general dispersion relation containing terms up to ω^6 and k^6 is very lengthy.

The results turn out to be transparent in some limiting cases. In particular, in the high-frequency limit, when $\omega\tau_{\text{HR}} \gg 1$ and $\omega\tau_{\text{R}} \gg 1$ simultaneously, terms describing the momentum transfer, i.e., containing τ_{HR} and τ_{R} , can be omitted. The heat transfer rate is usually not higher than the momentum transfer rate. Correspondingly, under this condition, the quantities $K_{\text{RP}}/\omega S_{\text{R}}$ etc., are also small [in particular, $K_{\text{RP}}/S_{\text{R}} = 1.6 \times 10^5 (T/0.1 \text{ K})^{13/3} \text{ s}^{-1}$]. Therefore, the hydrogen and ripples are coupled neither with each other nor with the substrate, and the system of Eqs. (1)–(6) is split into two independent systems. In this case, Eqs. (3) and (6) describe the propagation of the second surface sound (i.e., a ripplon density wave or, identically, a temperature wave) with a velocity of $u_{\text{R}} = S_{\text{R}}/\sqrt{\rho_{\text{R}}(\partial S_{\text{R}}/\partial T)} \propto T_{\text{R}}^{1/3}$ [22]. The remaining four equations describe two different oscillation modes in 2D H \downarrow , which are 2D analogues of the usual and second sounds. As usual, excluding the velocities from these equations and expressing $\Delta\mu$ and ΔP in terms of the increments of the density and temperature of hydrogen [23], we arrive at the following system of equations:

$$\ddot{\rho} - c^2 \Delta \rho - S \Delta T = 0, \quad (7)$$

$$B \ddot{\rho} - c^2 \frac{\rho_s}{\rho} \Delta \rho - \frac{\rho_n}{S} \left(\frac{\partial S}{\partial T} \right) \ddot{T} = 0. \quad (8)$$

Here, all quantities without subscripts refer to hydrogen, $c^2 = (\partial P/\partial \rho)_T$ is the speed of the usual sound in 2D

H \downarrow , and $B = 1 - \frac{\rho_n}{S} \left(\frac{\partial S}{\partial \rho} \right)$.

Substituting again the solution in the form of a plane wave, we obtain the following equation for the oscillation propagation velocity $u = \omega/k$:

$$u^4 - u^2 \left[c^2 + \frac{BS^2}{\rho_n (\partial S/\partial T)} \right] + \left(\frac{\rho_s}{\rho} \right) c^2 \frac{S^2}{\rho_n (\partial S/\partial T)} = 0. \quad (9)$$

Under these conditions, the fraction of the overcondensate hydrogen component approaches $\xi = m\tilde{U}/4\pi\hbar^2 \approx 0.14$ [20, 24]; i.e., it is sufficiently low, and the elementary excitations are Bogoliubov quasiparticles, whose energy $\hbar\omega_k$ and wavenumber k are related by the known relation $\hbar\omega_k = (\epsilon_k^2 + 2\sigma\tilde{U}\epsilon_k)^{1/2}$, where $\epsilon_k = \hbar^2 k^2/2m$. For low temperatures, in addition to the zeroth term $\sigma^2\tilde{U}/2$, long-wavelength excitations with the phonon-like dispersion relation, $\omega_k \approx ck$, where $c^2 = \sigma\tilde{U}/m$, make the basic contribution to the hydrogen energy. The expansion of the hydrogen pressure $P_{\text{H}} = -F_{\text{H}}$, where F_{H} is the free energy of the unit area, in powers of the ratio $\theta = T/mc^2$ is

$$P_{\text{H}} \approx \frac{1}{2} \sigma^2 \tilde{U} [1 + 2C\xi\theta^3 + \xi O(\theta^5)], \quad (10)$$

where $C = \int_0^\infty (e^x - 1)^{-1} x^2 dx \approx 2.404$. It is easy to estimate that the second and subsequent terms in the square brackets are appreciably smaller than the first term under the superfluidity conditions. From Eq. (10), we obtain the hydrogen entropy in the form $S_{\text{H}} = (\partial P_{\text{H}}/\partial T)_\mu \approx (\partial P_{\text{H}}/\partial T)_\sigma \approx 3C\xi\sigma\theta^2$; therefore, $B = 1 + \rho_n/\rho$. Note that S_{H} is comparable with the entropy of ripples; $S_{\text{R}} \approx 1.52 \times 10^{-2} T^{4/3} \text{ erg/cm}^2 \text{ K}^{7/3}$. Then, since $(\partial P_{\text{H}}/\partial \rho)_S \approx (\partial P_{\text{H}}/\partial \rho)_T \approx c^2$, the speed of the first and second sounds in superfluid 2D hydrogen are expressed as [25]

$$u_{\text{H1}}^2 \approx c^2 = \sigma\tilde{U}/m, \quad (11)$$

$$u_{\text{H2}}^2 \approx \frac{\rho_s S_{\text{H}}^2}{\rho_n \rho} \left(\frac{\partial S_{\text{H}}}{\partial T} \right)^{-1} \approx \frac{3}{2} C \xi \left(\frac{\rho_s}{\rho_n} \right) \theta^3 c^2, \quad (12)$$

respectively. It is interesting that the speed of the usual sound, as was expected, is determined only by interaction and is independent of temperature. At the same time, u_{H2}^2 is proportional to $T^{3/2}$ and inversely proportional to density. In particular, for $T \rightarrow 0$, the fraction of the normal component tends to ξ and the ratio of the speeds is equal to

$$u_{\text{H2}}/u_{\text{H1}} \approx 1.9\theta^{3/2}. \quad (13)$$

Then, let us analyze the case of weak coupling between ripples and the substrate, $\tau_{\text{HR}} \ll \tau_{\text{R}}$. Such a situation may be realized, e.g., on the surface of a bulk liquid or macroscopically thick films, as well as for a very smooth substrate; i.e., when the ripplon momentum relaxation is mainly due to interaction with phonons of the liquid in the absence of hydrogen. In this case, the choice of the oscillation frequency can ensure the condition $\tau_{\text{HR}}\omega \ll 1 \ll \tau_{\text{R}}\omega$, under which ripples simply represent the contribution to the normal density of hydrogen component similarly to the contribution of a small ^3He impurity in superfluid helium to the normal (phonon at low temperatures) density. In

this case, the total entropy S is conserved, the temperatures of the hydrogen and riplons coincide with each other, and, instead of Eq. (9), we obtain

$$u^4 - u^2(Ac^2 + Bu_2^2) + (\rho_s/\rho)c^2u_2^2 = 0. \quad (14)$$

Here, u_2 differs from u_{H2} by changing the entropy of hydrogen and the normal density ρ_n to the total entropy of the hydrogen–riplon mixture and $\rho'_n = \rho_n + \rho_R$, respectively. The factor $A = 1 - (\rho_R/\rho_H)(\rho_n/\rho'_n)$ differs slightly from unity, because $\rho_R \ll \rho_H$ for the case under consideration. Thus, the speed of the usual sound is again approximately equal to c , and the speed of the second sound, as expected, is given by the expression

$$u_{HR2}^2 \approx \frac{\rho_s S^2}{\rho'_n \rho} \left(\frac{\partial S}{\partial T} \right)^{-1}. \quad (15)$$

Finally, let us address the most interesting case of extremely low frequencies, $\omega\tau_R \ll 1$ and $\omega\tau_{HR} \ll 1$. In this case, the riplons and the normal hydrogen component are immobile, i.e., $\mathbf{v}_n = \mathbf{v}_R = 0$, which is similar to the case of the propagation of the fourth sound [9] involving only the superfluid hydrogen component. In this case, continuity equation (1) takes the form

$$\dot{\rho}_H + \rho_s \operatorname{div} \mathbf{v}_s = 0. \quad (16)$$

This equation, together with Eq. (4) and the expression for the chemical potential μ_H , provides the wave equation

$$m\ddot{\sigma} - \frac{\rho_s \tilde{U}}{m} \Delta \sigma. \quad (17)$$

Thus, the speed of the fourth sound is given by the expression

$$u_4^2 = \frac{\rho_s \tilde{U}}{m^2} = \frac{\rho_s}{\rho_H} c^2. \quad (18)$$

The fast transfer of the longitudinal momentum into the substrate does not imply that the heat transfer is also fast since there exist the *elastic* channel of the relaxation of the longitudinal momentum of riplons [13]. Therefore, for $\omega \gg K_{RP}/S_R = 1.6 \times 10^5 (T/0.1 \text{ K})^{13/3} \text{ s}^{-1}$, the temperatures of the hydrogen and riplons do not remain constant. According to the conditions, $\omega \ll \tau_{HR}^{-1} \sim K_{HR}/S_H$; i.e., the heat transfer between the hydrogen and riplons is sufficiently fast and, therefore, $T_H \approx T_R$. In this case, summing Eqs. (5) and (6), we see that the *total* entropy of the 2D system is conserved; i.e.,

$$dS = \frac{\partial S_H}{\partial \sigma} d\sigma + \frac{\partial}{\partial T} (S_H + S_R) dT = 0. \quad (19)$$

From this condition, we obtain the relation between the amplitudes of oscillations of the hydrogen density and temperature in the acoustic wave:

$$\frac{\delta\sigma}{\sigma} \approx \left[2 + \frac{\sigma \tilde{U}^2}{3C\xi T} \left(\frac{\partial S_R}{\partial T} \right) \right] \frac{\delta T}{T}. \quad (20)$$

It is interesting to note that the oscillations of the hydrogen density and temperature are in-phase, because the derivative $(\partial S_H/\partial \sigma)_T$ is negative. Finally, for extremely low frequencies $\omega \ll K_{RP}/S_R$, the temperature remains constant and equal to the substrate temperature.

In conclusion, note that the problem of a method for exciting and detecting oscillations is of particular importance for experiments. At high frequencies, when hydrogen (with or without riplons) is isolated from the substrate, the excitation of oscillations in 2D H \downarrow by modulating the temperature or velocity of the substrate is impossible. The efficient modulation of the density of hydrogen itself at a frequency ω by means of ESR is possible only for $\omega T_2 \lesssim 1$, because the induced recombination of hydrogen atoms is due to transverse relaxation with a time constant T_2 . Indeed, in the absence of transverse relaxation, the precession of spins is coherent and any pair of atoms thereby remains in the triplet state, where recombination is impossible. The problem of a mechanism and transverse relaxation rate in quasi-condensed (locally coherent) 2D hydrogen is closely connected with the aforementioned problem of establishing thermal equilibrium. The classical estimate of the rate of transverse relaxation due to dipole–dipole interaction upon elastic atomic collisions yields $T_2^{-1} \sim \sigma \times 10^{-6} \text{ cm}^2/\text{s}$ [6, 26], which is comparable with the momentum transfer rate τ_{HR}^{-1} into riplons. Therefore, high-frequency oscillations can be excited by ESR only when the coupling of riplons with the substrate is weak. Moreover, it is known that the dissipation of a 2D superflow increases with both the oscillation frequency and superfluid velocity [3]. According to the above consideration, the fourth sound realized at low frequencies is a most promising tool for experimental observation of superfluidity in 2D H \downarrow . “Oscillations” with $\omega = 0$, i.e., a steady flow of the superfluid component, present a specific kind of the fourth sound. In particular, this mode must be substantial for the formation of the instability of the ESR spectrum of 2D hydrogen [6].

I am grateful to L.A. Maksimov for stimulating discussions and I.I. Lukashevich for support and attention to the work. This work was supported by the Russian Foundation for Basic Research and the Ministry of Science and Education of the Russian Federation.

REFERENCES

1. V. L. Berezinskiĭ, Zh. Éksp. Teor. Fiz. **59**, 907 (1970) [Sov. Phys. JETP **32**, 493 (1970)]; Zh. Éksp. Teor. Fiz. **61**, 1144 (1971) [Sov. Phys. JETP **34**, 610 (1972)].

2. J. M. Kosterlitz and D. J. Thouless, *J. Phys. C* **5**, L124 (1972).
3. D. J. Bishop and J. D. Reppy, *Phys. Rev. B* **22**, 5171 (1980).
4. A. I. Safonov, S. A. Vasilyev, I. S. Yasnikov, *et al.*, *Phys. Rev. Lett.* **81**, 4545 (1998).
5. A. I. Safonov, A. A. Kharitonov, and I. I. Lukashevich, *J. Low Temp. Phys.* **138** (1/2) (2005).
6. S. A. Vasilyev, A. I. Safonov, J. Järvinen, *et al.*, *Phys. Rev. Lett.* **89**, 153002 (2002).
7. S. A. Vasilyev, J. Järvinen, A. I. Safonov, and S. Jaakkola, *Phys. Rev. A* **69**, 023610 (2004).
8. K. R. Atkins, *Can. J. Phys.* **31**, 1165 (1953).
9. I. M. Khalatnikov, *An Introduction to the Theory of Superfluidity* (Nauka, Moscow, 1965; Addison-Wesley, Redwood City, 1988).
10. M. W. Reynolds and G. V. Shlyapnikov, *Phys. Lett. A* **207**, 105 (1992).
11. D. S. Zimmerman and A. J. Berlinsky, *Can. J. Phys.* **61**, 508 (1983).
12. I. B. Mantz, D. O. Edwards, and V. U. Nayak, *Phys. Rev. Lett.* **44**, 663 (1980); **44**, 1094(E) (1980).
13. A. I. Safonov, S. S. Demukh, and A. A. Kharitonov, *Pis'ma Zh. Éksp. Teor. Fiz.* **79**, 362 (2004) [*JETP Lett.* **79**, 304 (2004)].
14. I. B. Mantz, D. O. Edwards, and V. U. Nayak, *J. Phys. Colloq.* **39**, C6-300 (1978).
15. E. M. Lifshitz and L. P. Pitaevskii, *Course of Theoretical Physics, Vol. 9: Statistical Physics* (Nauka, Moscow, 1978; Pergamon, New York, 1980), Part 2, pp. 161–165.
16. W. F. Saam, *Phys. Rev. A* **8**, 1918 (1973).
17. P. Roche, M. Roger, and F. I. B. Williams, *Phys. Rev. B* **53**, 2225 (1996).
18. In contrast to a usual gas mixture, the continuity equation is not valid for the hydrogen–rippion mixture, because the number of rippions is not conserved.
19. N. Prokof'ev and B. Svistunov, *Phys. Rev. A* **66**, 043608 (2002).
20. U. Al Khawaia, J. O. Andersen, N. P. Proukakis, and H. T. C. Stoof, *Phys. Rev. A* **66**, 013615 (2002).
21. M. W. Reynolds, I. D. Setija, and G. V. Shlyapnikov, *Phys. Rev. B* **46**, 575 (1992).
22. A. F. Andreev and D. A. Kompaneets, *Zh. Éksp. Teor. Fiz.* **61**, 2459 (1972) [*Sov. Phys. JETP* **34**, 1316 (1972)].
23. Hereinafter, we ignore a very weak, no stronger than logarithmic, dependence of \bar{U} on the hydrogen density (see, e.g., [24]).
24. Yu. Kagan, B. V. Svistunov, and G. V. Shlyapnikov, *JETP Lett.* **42**, 209 (1985).
25. When deriving Eqs. (11) and (12), only corrections linear in the ratio $(u_{\text{H}_2}/c)^2 \ll 1$ are retained. The linear correction to $u_{\text{H}_1}^2$ is equal to $2u_{\text{H}_2}^2 (\rho_n/\rho_s)$ and, therefore, can be omitted. At the same time, the correction to $u_{\text{H}_2}^2$ that has the same magnitude but opposite sign is significant.
26. I. Shinkoda and W. N. Hardy, *J. Low Temp. Phys.* **85**, 99 (1991).

Translated by R. Tyapaev

Density of States Anomalies in Hybrid Superconductor–Ferromagnet–Normal Metal Structures[†]

A. A. Golubov¹, M. Yu. Kupriyanov^{2,3}, and M. Siegel³

¹ Faculty of Science and Technology, University of Twente, The Netherlands

² Nuclear Physics Institute, Moscow State University, Moscow, 119992 Russia

³ Institute for Micro- and Nanoelectronic Systems, Karlsruhe University, D-76187 Karlsruhe, Germany

e-mail: a.golubov@tn.utwente.nl, mkupr@pn.sinp.msu.ru, m.siegel@ims.uni-karlsruhe.de

Received January 25, 2005

The results of calculations of the spatially-resolved density of states (DOS) in an S(F/N) bilayer are presented (S is a superconductor, F is a metallic ferromagnet, N is a normal metal) within quasiclassical theory in the dirty limit. Analytical solutions are obtained in the case of thin F, N layers which demonstrate the peculiar features of DOS in this system. The dependences of the minigap and the DOS peak positions on the exchange energy and parameters of the layers are studied numerically. © 2005 Pleiades Publishing, Inc.

PACS numbers: 74.50.+r, 74.80.Dm, 75.30.Et

In the past few years, there was a noticeable interest to the Josephson junctions with ferromagnetic barriers due to possibility to realize the π -junctions having the phase difference π in the ground state. The π -states in SFS junctions were first predicted by [1–3] and realized experimentally by Ryazanov *et al.* [4, 5] in Nb/CuNi/Nb structures and later by other groups [6–10] using different ferromagnetic barriers. These experiments stimulated further theoretical activity (see [11] for the review). In particular, Josephson structures composed from arrays of 0- and π -Josephson junctions should exhibit extraordinary characteristics [12, 13]. Such arrays were recently realized in zigzag HTS/LTS structures [14].

The purpose of the present paper is to study spatially resolved electronic density of states (DOS) in the structure of S(FN) type (S is superconductors, F is a metallic ferromagnet, N is a normal metal), consisting of a bulk superconductor with ferromagnetic and normal layers on the top of it, which is a generic system for 0- and π -junctions connected in parallel.

DOS in SF bilayers (a ferromagnet coupled to a superconductor) was studied quite extensively before. Two new features were predicted compared to SN systems: spin splitting and spatial oscillations of DOS in a ferromagnet [15–21]. The effect of spatial oscillations was quite extensively discussed in the theoretical literature in different models [15–18] and observed experimentally [22]. This effect is closely related to 0– π transitions. The effect of splitting is relevant for thin ferromagnetic layers and was studied theoretically in [19, 20]. In the present work, we discuss an interplay

between the oscillations and splitting in a more complex S(F/N) structure.

The geometry of the structure is shown in Fig. 1. We assume that the dirty limit conditions are fulfilled in all metals, F is a weak monodomain ferromagnet with the exchange energy H much smaller than the Fermi energy, and the interfaces are not magnetically active. In this case, spin-dependent corrections to the resistivities can be neglected and the S(F/N) structure is described by the following spin-independent suppression parameters:

$$\gamma_{BF} = R_{BF} \mathcal{A}_{BF} / \rho_F \xi_F, \quad \gamma_F = \rho_S \xi_S / \rho_F \xi_F, \quad (1)$$

$$\gamma_{BN} = R_{BN} \mathcal{A}_{BN} / \rho_N \xi_N, \quad \gamma_N = \rho_S \xi_S / \rho_N \xi_N, \quad (2)$$

$$\gamma_B = R_B \mathcal{A}_B / \rho_N \xi_N, \quad \gamma = \rho_F \xi_F / \rho_N \xi_N. \quad (3)$$

Here, R_{BF} , R_{BN} , and R_B are the specific resistivities of the SF, SN, and NF interfaces, respectively; $\rho_{S,F,N}$, $D_{S,F,N}$, and $\xi_{S,F,N}$ are the resistivities, the diffusion constants, and the coherence lengths of the S, F, and N layer and

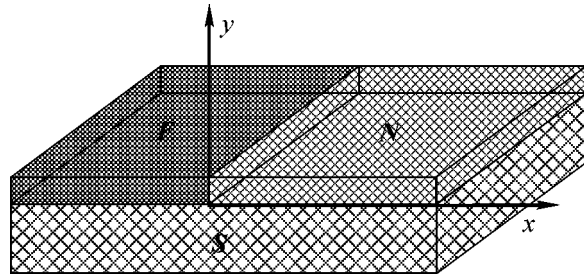


Fig. 1. The geometry of the structure.

[†]This article was submitted by the authors in English.

the coherence lengths, where $\xi_{S,F,N} = \sqrt{D_{S,F,N}/2\pi T_c}$ and T_c is the critical temperature of the superconductor.

Under the above assumptions, the problem can be solved in the framework of the Usadel equations [23]. To simplify it further, we assume that S is a bulk superconductor and $\gamma_N \ll \gamma_{BN}$, $\gamma_F \ll \gamma_{BF}$ so that the rigid boundary conditions

$$F_S = \frac{\Delta}{\sqrt{\omega^2 + \Delta^2}}, \quad G_S = \frac{\omega}{\sqrt{\omega^2 + \Delta^2}}$$

are valid for superconductor. Here, Δ is the magnitude of the order parameter in S electrode, F_S and G_S are the Green's functions, $\omega = \pi T(2n + 1)$ are the Matsubara frequencies.

Let us choose the x, y axes as shown in Fig. 1 and use the θ parametrization $G = \cos\theta$, $F = \sin\theta$, then the Usadel equations have the form

$$\xi_{F,N}^2 \frac{\pi T_c}{\tilde{\omega}} \left\{ \frac{\partial^2}{\partial x^2} \theta_{F,N} + \frac{\partial^2}{\partial y^2} \theta_{F,N} \right\} - \sin\theta_{F,N} = 0, \quad (4)$$

where $\tilde{\omega} = \omega + iH$ in F and $\tilde{\omega} = \omega$ in N.

The boundary conditions at the SF ($y = 0, -\infty < x \leq 0$), SN ($y = 0, 0 \leq x < \infty$), and FN ($x = 0, 0 \leq y \leq d_F, d_N$) interfaces have the form [24]

$$\gamma_{B(F,N)} \xi_{F,N} \frac{\partial}{\partial y} \theta_{F,N} = -\sin(\theta_S - \theta_{F,N}), \quad y = 0, \quad (5)$$

$$\begin{aligned} \gamma_B \xi_F \frac{\partial}{\partial x} \theta_F &= \sin(\theta_N - \theta_F), \\ x = 0, \quad 0 \leq y \leq d_F, d_N, \end{aligned} \quad (6)$$

$$\xi_N \frac{\partial}{\partial x} \theta_N = \gamma \xi_F \frac{\partial}{\partial x} \theta_F, \quad x = 0, \quad 0 \leq y \leq d_F, d_N,$$

where $\sin\theta_S = \Delta/\sqrt{\omega^2 + \Delta^2}$ and $\cos\theta_S = \omega/\sqrt{\omega^2 + \Delta^2}$. At the free interfaces, the boundary conditions are

$$\frac{\partial}{\partial y} \theta_{F,N} = 0, \quad y = d_{F,N}, \quad (7)$$

$$\frac{\partial}{\partial x} \theta_{F,N} = 0, \quad 0 \leq y \leq d_F, \quad x \rightarrow \mp\infty. \quad (8)$$

We will consider the limit of thin F and N layers $d_{F,N} \ll \xi_{F,N}$. In this case, one can neglect both the derivative on x and nongradient items in Usadel equations (4) and substitute the resulting solutions

$$\begin{aligned} \theta_{F,N}(x, y) &= \theta_{F,N}(x) \\ &- K_{F,N}(x) \frac{d_{F,N}}{\xi_{F,N}^2} y + K_{F,N}(x) \frac{y^2}{2\xi_{F,N}^2}, \end{aligned}$$

$$K_{F,N}(x) = \left\{ \frac{\tilde{\omega}}{\pi T_c} \sin\theta_{F,N} - \xi_{F,N}^2 \frac{\partial^2}{\partial x^2} \theta_{F,N} \right\},$$

into boundary conditions (5). Then, the problem is reduced to the one-dimensional equations for lateral variations of $\theta_{N,F}$ in the x -direction:

$$\zeta_{N,F}^2 \frac{\partial^2}{\partial x^2} \theta_{N,F} - \sin(\theta_{N,F} - \theta_{N,F}(\pm\infty)) = 0, \quad (9)$$

where

$$\theta_{N,F}(\pm\infty) = \arctan \frac{\pi T_c \sin\theta_S}{\tilde{\omega} \tilde{\gamma} + \pi T_c \cos\theta_S}, \quad (10)$$

the decay lengths ζ_N and ζ_F are

$$\zeta_{N,F} = \xi_{N,F} \sqrt{\frac{\pi T_c \tilde{\gamma} \cos\theta_{N,F}(\pm\infty)}{(\tilde{\omega} \tilde{\gamma} + \pi T_c \cos\theta_S)}}, \quad (11)$$

and we have taken for simplicity equal barrier parameters for F and N

$$\gamma_{BN} \frac{d_N}{\xi_N} = \gamma_{BF} \frac{d_F}{\xi_F} \equiv \tilde{\gamma}. \quad (12)$$

The general solution of Eq. (9) has the form

$$\begin{aligned} \theta_{N,F}(x) &= \theta_{N,F}(\pm\infty) \\ &+ 4 \arctan \left[\left(\frac{\tan \frac{\theta_{N,F}(0) - \theta_{N,F}(\pm\infty)}{4}}{\mp \frac{x}{\zeta_{N,F}}} \right) \exp \left\{ \mp \frac{x}{\zeta_{N,F}} \right\} \right]. \end{aligned} \quad (13)$$

The integration constants $\theta_N(0)$ and $\theta_F(0)$ in (13) have to be determined from the boundary conditions (6) at $x = 0$ and can be found analytically in the limit of large transparency of the FN interface when $\theta(x)$ is continuous at $x = 0$:

$$\theta_N(0) = \theta_F(0) = \theta(0).$$

From (11), it follows that the effective decay length in normal metal, ζ_N , is a real quantity and equals to $\zeta_N = \xi_N \sqrt{\tilde{\gamma}}$ for small ω and tends to $\zeta_N = \xi_N \sqrt{\pi T_c / \omega}$ with ω increase. The effective decay length ζ_F in ferromagnet at low $\omega \ll \Delta$, $H/\tilde{\gamma}$ is given by $\zeta_F = \xi_F \sqrt{\tilde{\gamma} / \sqrt{1 - \tilde{\gamma}^2 (H/\pi T_c)^2}}$, i.e., it becomes complex for sufficiently strong exchange field $H > \pi T_c / \tilde{\gamma}$.

Below, we consider several limiting cases.

Identical F and N metals. Assume for simplicity that the F and N materials differ by the existence the

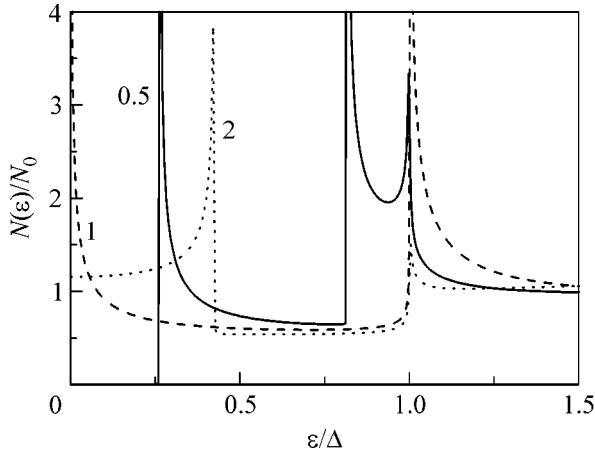


Fig. 2. The total DOS in an SF bilayer for various values of $\tilde{\gamma}h$ as indicated in the figure.

exchange field in F ($\gamma = 1$, $\xi_F = \xi_N = \xi$), then, from (6) for $\theta(0)$, we have

$$\theta(0) = 2 \arctan \frac{\sin \frac{\theta_N(\infty)}{2} + g \sin \frac{\theta_F(-\infty)}{2}}{\cos \frac{\theta_N(\infty)}{2} + g \cos \frac{\theta_F(-\infty)}{2}}, \quad (14)$$

$$g = \frac{\zeta_N}{\zeta_F}.$$

Identical F metals with antiparallel direction of magnetization. The results can be easily generalized to the case of an S(F/F) structure with two identical ferromagnetic films having opposite magnetization directions (antiferromagnetic configuration)

$$\theta(0) = 2 \arctan \frac{g^* \sin \frac{\theta_F^*(-\infty)}{2} + g \sin \frac{\theta_F(-\infty)}{2}}{g^* \cos \frac{\theta_F^*(-\infty)}{2} + g \cos \frac{\theta_F(-\infty)}{2}}. \quad (15)$$

Using the solutions obtained above, one can calculate the spatially resolved DOS in S(F/N) and S(F/F) structures.

DOS in S(F/N) and S(F/F) proximity systems. The DOS for each spin direction is given by

$$N(\varepsilon) = \frac{N_0}{2} \text{Re} G(\omega \rightarrow -i\varepsilon + \delta), \quad (16)$$

where N_0 is the total DOS for both spins at the Fermi surface in the normal state and $G(\varepsilon - i\delta) = \cos\theta(\varepsilon - i\delta)$ is the retarded Green's function. The total DOS is found by summing over both spin projections, i.e., $N^{\text{total}} = N(H) + N(-H)$.

DOS in N and F metals far from the F/N interface. In a normal metal far from the F/N interface ($x = \infty$), the total DOS is given by

$$N_N(\varepsilon) = N_0 \text{Re} \frac{\tilde{\varepsilon}_N}{\Omega_N}, \quad \Omega_N = \sqrt{\tilde{\varepsilon}_N^2 - \Delta^2} \text{sgn}(\varepsilon), \quad (17)$$

$$\tilde{\varepsilon}_N = \varepsilon(1 + \tilde{\gamma}\sqrt{\Delta^2 - \varepsilon^2}/\pi T_c).$$

It is well known (see [25, 26]) that DOS in a F/N bilayer has a minigap at $\varepsilon_g < \Delta$, which depends on the value of $\tilde{\gamma}$, and $N_N(\varepsilon)$ has the peaks at $\varepsilon = \varepsilon_g$ and $\varepsilon = \Delta$. The minigap ε_g characterizes the strength of superconducting correlations induced into N metal due to the proximity effect.

In SF bilayers, modifications of DOS due to spin splitting of energy levels were investigated in [19, 20]. The DOS per spin projection in the F layer has the form

$$N_{F\uparrow, F\downarrow}(\varepsilon) = \frac{N_0}{2} \text{Re} \frac{\tilde{\varepsilon}_{F\uparrow, F\downarrow}}{\Omega_{F\uparrow, F\downarrow}}, \quad (18)$$

$$\Omega_{F\uparrow, F\downarrow} = \sqrt{\tilde{\varepsilon}_{F\uparrow, F\downarrow}^2 - \Delta^2} \text{sgn}(\varepsilon \mp H),$$

$$\tilde{\varepsilon}_{F\uparrow, F\downarrow} = \varepsilon + \tilde{\gamma}(\varepsilon \mp H)\sqrt{\Delta^2 - \varepsilon^2},$$

which demonstrates the energy renormalization due to the exchange field. In particular, it follows from (18) that now there are two minigaps in the spectrum $\varepsilon_{g\uparrow}$ and $\varepsilon_{g\downarrow}$ and $\varepsilon_{g\uparrow} \leq \varepsilon_g \leq \varepsilon_{g\downarrow}$.

The total DOS in a F/N bilayer $N_{\text{tot}}(\varepsilon) = N_{F\downarrow}(\varepsilon) + N_{F\uparrow}(\varepsilon)$ is shown in Fig. 2. It is clearly seen that, at $h = H/\pi T_c < 1/\tilde{\gamma}$, there are three peaks in DOS located at $\varepsilon_{g\downarrow}$, $\varepsilon_{g\uparrow}$, and Δ , respectively. At $h = 1/\tilde{\gamma}$, the low-energy singularity is shifted to the Fermi level, and for $h > 1/\tilde{\gamma}$, the first peak disappears resulting in only two singularities in the DOS at $\varepsilon = \varepsilon_{g\uparrow}$ and $\varepsilon = \Delta$. Note that the total DOS at low energies depends nonmonotonously on H even in a thin F-layer, even though spatial oscillations are absent across the layer. Equation (18) yields $N_{F\uparrow, F\downarrow}(\varepsilon = 0) = (N_0/2) \text{Re}(\tilde{\gamma}h \text{sgn}(h)/\sqrt{\tilde{\gamma}^2 h^2 - 1})$. For $\tilde{\gamma}h < 1$, the total DOS $N(0) = 0$ due to the minigap in F, while for $\tilde{\gamma}h \geq 1$, the total low-energy DOS increases sharply, exceeds unity, and saturates at $N(0) = N_0$ for $\tilde{\gamma}h \gg 1$.

DOS at the F/N interface. At $x = 0$ and for identical transport parameters on the F and N metals from (14), (16), we obtain

$$N_{F\uparrow, F\downarrow}(\varepsilon) = \frac{N_0}{2} \text{Re} \frac{-i\tilde{\varepsilon}_N - i\tilde{\varepsilon}_{F\uparrow, F\downarrow} + 2\tilde{\varepsilon}_{FN}}{\Omega_{F\uparrow, F\downarrow} + \Omega_N + 2\sqrt{\Delta^2 - \tilde{\varepsilon}_{FN}^2}}, \quad (19)$$

where

$$\tilde{\varepsilon}_{FN} = \sqrt{\frac{\Omega_N \Omega_{F\uparrow, F\downarrow} - \tilde{\varepsilon}_N \tilde{\varepsilon}_{F\uparrow, F\downarrow} - \Delta^2}{2}}, \quad (20)$$

and Ω_N , $\tilde{\varepsilon}_N$ and $\Omega_{F\uparrow, F\downarrow}$, $\tilde{\varepsilon}_{F\uparrow, F\downarrow}$ are defined by (17) and (18), respectively.

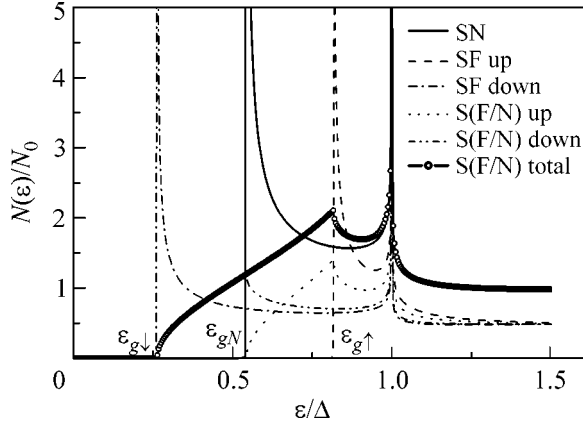


Fig. 3. Spin-resolved DOS: comparison of FS, FN, and S(FN) for $\tilde{\gamma}h = 0.5$.

It follows from Eq. (19) that, similar to the case of the SF bilayer considered above, the minigap exists if $\tilde{\gamma}h < 1$. With increasing exchange field, the total DOS at $\epsilon = 0$ becomes nonzero if $\tilde{\gamma}h > 1$ is given by simple expression

$$N(0) = N_0 \sqrt{\tilde{\gamma}^2 h^2 - 1} / \tilde{\gamma} h. \quad (21)$$

DOS at the F/F interface. At $x = 0$, we have

$$N(\epsilon)/N_0 = \text{Re} \frac{-2i\tilde{\epsilon}_N + 2\tilde{\epsilon}_{FF}}{\Omega_{F\uparrow} + \Omega_{F\downarrow} + 2\sqrt{\Delta^2 - \tilde{\epsilon}_{FF}^2}}, \quad (22)$$

$$\tilde{\epsilon}_{FF} = \sqrt{\frac{\Omega_{F\uparrow}\Omega_{F\downarrow} - \tilde{\epsilon}_{F\uparrow}\tilde{\epsilon}_{F\downarrow} - \Delta^2}{2}}.$$

It can be shown that DOS at the F/F interface given by Eq. (22) coincides exactly with the total DOS for the F/N interface, $N_{F\uparrow}(\epsilon) + N_{F\downarrow}(\epsilon)$, where $N_{F\uparrow}(\epsilon)$ and $N_{F\downarrow}(\epsilon)$ are given by Eq. (19). In particular, the minigap exists if $\tilde{\gamma}h \leq 1$, and at $\tilde{\gamma}h > 1$, the DOS at F/F is determined by Eq. (21).

The results of calculations from Eq. (19) at low temperatures $T \ll T_c$ are shown in Figs. 3 and 4 for $\tilde{\gamma}h = 0.5$ and $\tilde{\gamma}h = 2$, respectively, together with the DOS for SF ($x \rightarrow -\infty$) and SN ($x \rightarrow \infty$) bilayers.

There are four characteristic energies in the system: $\epsilon_{g\downarrow}$, ϵ_g , $\epsilon_{g\uparrow}$, and Δ . Here, $\epsilon_{g\downarrow}$ is the minigap for the spin-down subband SF bilayer at $x \rightarrow -\infty$. It follows from Eq. (19) that $N_{F\downarrow}(\epsilon) = 0$ at $\epsilon \leq \epsilon_{g\downarrow}$ and becomes nonzero at $\epsilon > \epsilon_{g\downarrow}$, i.e., $\epsilon_{g\downarrow}$ is the minigap for the spin-down subband in S(FN) at $x = 0$. However, contrary to SF case, $N_{F\downarrow}(\epsilon)$ has no peak $\epsilon = \epsilon_{g\downarrow}$ but grows continuously from zero value.

For the spin-up subband, the minigap in $N_{F\uparrow}(\epsilon)$ is not equal to the gap $\epsilon_{g\uparrow}$ in the spin-up subband in SF

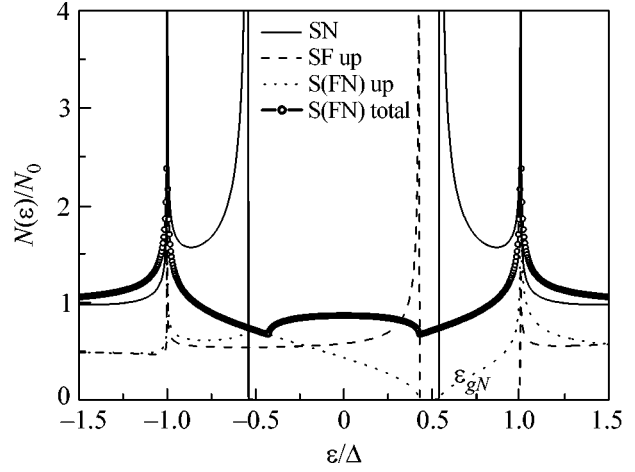


Fig. 4. Spin-resolved DOS: comparison of FS, FN, and S(FN) for $\tilde{\gamma}h = 2$.

bilayer at $x \rightarrow -\infty$. Instead, $N_{F\uparrow}(\epsilon)$ the gap value is determined by ϵ_g , the minigap in SN bilayer at $x \rightarrow \infty$. The formal reason is that, in the interval $\epsilon \geq \epsilon_g$, Ω_N becomes an imaginary number and both numerator and denominator in Eq. (19) are complex, thus leading to nonzero DOS in this energy range. Similar to the spin-down case, there is no peak in $N_{F\uparrow}(\epsilon)$ at the gap energy $\epsilon = \epsilon_g$, while the peak occurs at $\epsilon = \epsilon_{g\uparrow}$ (see Fig. 3). With further increase of energy, there is a sharp peak in DOS at $\epsilon = \Delta$ followed by saturation at $N_0/2$ for $\epsilon \gg \Delta$.

For $h\tilde{\gamma} > 1$, the minigap at $N_{F\downarrow}(\epsilon)$ vanishes and the structure of DOS becomes different, as illustrated in Fig. 4 for the case $h\tilde{\gamma} = 2$. The main qualitative difference from the previous case is that the spin-down and total DOS are gapless for $h\tilde{\gamma} < 1$.

The total DOS at the F/N interface at $x = 0$ (which coincides with the total DOS in the F/F case), is shown

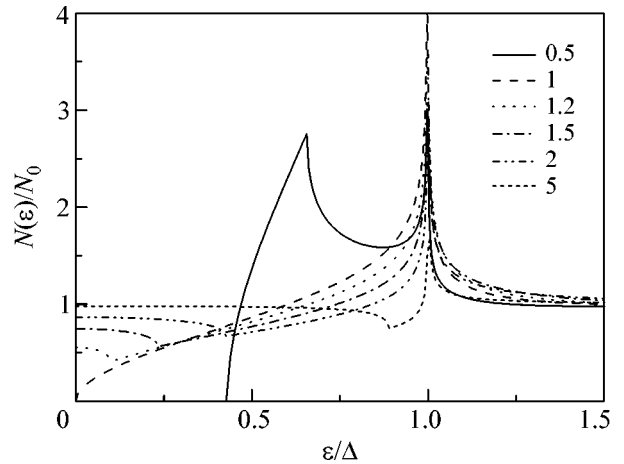


Fig. 5. The total DOS in S(FN) for various values of $\tilde{\gamma}h$ as indicated in the figure.

in Fig. 5 for various values of $h\tilde{\gamma}$. One can see that the gap is closed at $h\tilde{\gamma} = 1$, and the broad zero-energy DOS peak is formed with further increase of h until low-energy states become continuously filled at $h\tilde{\gamma} \gg 1$.

In conclusion, we have studied theoretically the spatially-resolved DOS in the S(FN) structures and in S(FF) structures with antiparallel magnetization directions. Analytical solutions were obtained in the case of thin F, N layers which demonstrate the peculiar features of DOS in this system. We have illustrated the results numerically and have studied the dependences of the minigap and the DOS peak positions on the exchange energy and parameters of the layers.

This work was supported in part by Russian Ministry of Education and Science and by the Russian Foundation for Basic Research (project no. 04-02-17397a).

REFERENCES

1. A. I. Buzdin, L. N. Bulaevskii, and S. V. Panyukov, *Pis'ma Zh. Éksp. Teor. Fiz.* **35**, 147 (1982) [*JETP Lett.* **35**, 178 (1982)].
2. A. I. Buzdin and M. Yu. Kupriyanov, *Pis'ma Zh. Éksp. Teor. Fiz.* **53**, 308 (1991) [*JETP Lett.* **53**, 321 (1991)].
3. A. I. Buzdin, B. Vujičić, and M. Yu. Kupriyanov, *Zh. Éksp. Teor. Fiz.* **101**, 231 (1992) [*Sov. Phys. JETP* **74**, 124 (1992)].
4. V. V. Ryazanov, V. A. Oboznov, A. Yu. Rusanov, *et al.*, *Phys. Rev. Lett.* **86**, 2427 (2001).
5. V. V. Ryazanov, V. A. Oboznov, A. V. Veretennikov, and A. Yu. Rusanov, *Phys. Rev. B* **65**, 020501 (2002).
6. O. Bourgeois, P. Gandit, A. Sulpice, *et al.*, *Phys. Rev. B* **63**, 064517 (2001).
7. T. Kontos, M. Aprili, J. Lesueur, *et al.*, *Phys. Rev. Lett.* **89**, 137007 (2002).
8. C. Surgers, T. Hoss, C. Schonenberger, and C. Strunk, *J. Magn. Magn. Mater.* **240**, 598 (2002).
9. Y. Blum, A. Tsukernik, M. Karpovskii, and A. Palevski, *Phys. Rev. Lett.* **89**, 187004 (2002).
10. H. Sellier, C. Baraduc, F. Lefloch, and R. Calemczuk, *Phys. Rev. B* **68**, 054531 (2003).
11. A. A. Golubov, M. Yu. Kupriyanov, and E. Il'ichev, *Rev. Mod. Phys.* **76**, 411 (2004).
12. R. Mints, *Phys. Rev. B* **57**, R3221 (1998); R. G. Mints and I. Papiashvili, *Phys. Rev. B* **64**, 134501 (2001).
13. A. I. Buzdin and A. E. Koshelev, *Phys. Rev. B* **67**, 220504 (2003).
14. H. Hilgenkamp, Ariando, H. J. H. Smilde, *et al.*, *Nature* **422**, 50 (2003).
15. A. I. Buzdin, *Phys. Rev. B* **62**, 11377 (2000).
16. I. Baladie and A. Buzdin, *Phys. Rev. B* **64**, 224514 (2001).
17. M. Zareyan, W. Belzig, and Yu. V. Nazarov, *Phys. Rev. Lett.* **86**, 308 (2001); *Phys. Rev. B* **65**, 184505 (2002).
18. F. S. Bergeret, A. F. Volkov, and K. B. Efetov, *Phys. Rev. B* **65**, 134505 (2002).
19. V. N. Krivoruchko and E. A. Koshina, *Phys. Rev. B* **66**, 014521 (2002).
20. A. A. Golubov, M. Yu. Kupriyanov, and Ya. V. Fominov, *Pis'ma Zh. Éksp. Teor. Fiz.* **75**, 223 (2002) [*JETP Lett.* **75**, 190 (2002)].
21. D. Huertas-Hernando and Yu. V. Nazarov, *cond-mat/0404622*.
22. T. Kontos, M. Aprili, J. Lesueur, and X. Grison, *Phys. Rev. Lett.* **86**, 304 (2001).
23. K. D. Usadel, *Phys. Rev. Lett.* **25**, 507 (1970).
24. M. Yu. Kupriyanov and V. F. Lukichev, *Zh. Éksp. Teor. Fiz.* **94** (6), 139 (1988) [*Sov. Phys. JETP* **67**, 1163 (1988)].
25. W. L. McMillan, *Phys. Rev.* **175**, 537 (1967).
26. A. A. Golubov and M. Yu. Kupriyanov, *Zh. Éksp. Teor. Fiz.* **96**, 1420 (1989) [*Sov. Phys. JETP* **69**, 805 (1989)].

New Class of Non-Carbon AIP Nanotubes: Structure and Electronic Properties

S. V. Lisenkov¹, G. A. Vinogradov¹, and N. G. Lebedev²

¹ Emanuel Institute of Biochemical Physics, Russian Academy of Sciences, ul. Kosygina 4, Moscow, 119991 Russia
e-mail: lisenkov@sky.chph.ras.ru

² Faculty of Physics, Volgograd State University, ul. Prodol'naya 30, Volgograd, 400062 Russia

Received January 26, 2005

A new class of non-carbon nanotubes based on Group III and Group V elements (aluminum and phosphorus, respectively) is considered. The equilibrium geometry, energy characteristics, and electronic structure of the AIP nanotubes were calculated using the density functional theory. These calculations demonstrated that the AIP nanotubes are energetically stable structures. It was found that a low strain energy (approximately 0.01–0.07 eV) is required for rolling a two-dimensional hexagonal AIP structure into a tube. The AIP nanotubes are found to be wide-band-gap semiconductors with a band gap of 2.05–3.73 eV with direct (for the zigzag type) or indirect (for the armchair type) transitions between the top of the valence band and the bottom of the conduction band. The band gap of these nanotubes increases with the tube diameter, approaching the band gap of a two-dimensional hexagonal AIP layer. © 2005 Pleiades Publishing, Inc.

PACS numbers: 61.48.+w, 73.20.At, 73.22.–f

The synthesis of carbon nanotubes in 1991 [1] caused a burst of activity by both experimenters and theorists. It was found [2, 3] that these structures exhibit a set of properties useful for potential applications. More recently, it was found that carbon is not the only element capable of forming nanotube structures. In 1992, the first non-carbon nanotubes were synthesized based on layered molybdenum disulfide and tungsten disulfide [4]. This discovery stimulated a variety of theoretical studies and experiments (e.g., see reviews [5–7]) on searching for and synthesizing new possible non-carbon nanotube structures that are geometrically similar to carbon nanotubes.

Among the whole variety of non-carbon materials, III–V semiconductors have attracted major attention because of their potential applications. Boron–nitrogen (BN) nanotubes were the first type of theoretically predicted non-carbon nanotubes geometrically similar to carbon nanotubes [8, 9]. However, these nanotubes were synthesized by an arc discharge only in 1995 [10]. Recently, a variety of non-carbon nanotubes, including nanotubes based on Group III and Group V elements, have been theoretically predicted [11–16] and synthesized [17–20]. As a rule, the classification proposed previously [21] for carbon nanotubes is used for describing non-carbon nanotubes composed of hexagons.

It is well known that diamond-structured carbon and a BN crystal with the zinc-blende structure are dielectrics with nearly equal energy gaps ($E_g \sim 5.5$ eV). However, the electronic properties of their quasi-one-dimensional forms (nanotubes as the graphene plane rolled

into a cylinder) are essentially different. Thus, carbon nanotubes can be either conducting or semiconducting depending on their helicity [21, 22], whereas BN nanotubes are dielectrics with an energy gap of about 5.5 eV, which is nearly independent of the helicity of BN nanotubes [8]. It was found that the electronic structure of other classes of non-carbon nanotubes based on Group III and Group V elements (GaN and AlN) [11, 12] is also different from the electronic structure of carbon nanotubes.

In this work, using density functional theory (DFT), we simulated the geometric structure and calculated the electronic properties of a new class of non-carbon nanotubes based on aluminum (Al) and phosphorus (P), elements of Groups III and V, respectively. It is well known that an AIP crystal with the zinc-blende structure is a semiconductor with an energy gap of 2.45 eV and an indirect transition between the valence band and the conduction band. Therefore, it is of interest to determine the energetic stability of AIP nanotubes and to calculate their electronic structure in order to estimate their potential applications in nanotechnology.

The calculations were performed using DFT [23], which is commonly applied to calculate the electronic structures and geometric and energetic properties of various materials. This theory has been successfully used to study the properties of a variety of non-carbon nanotube structures [8, 9, 11, 12, 14, 15]. The computations were performed using the ABINIT code [24] involving a plane-wave basis and pseudopotentials. This program is based on an efficient algorithm of fast Fourier transforms (used for converting wave functions

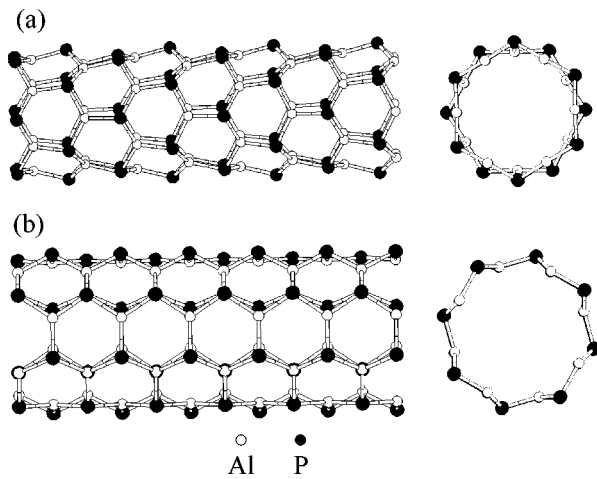


Fig. 1. Examples of AIP nanotubes: (a) zigzag (6,0) and (b) armchair (4,4). Open and closed circles indicate aluminum and phosphorus atoms, respectively.

between the direct and reciprocal spaces) [25], the conjugate gradient method [26], and the potential-based conjugate gradient algorithm for the determination of the self-consistent potential [27] and total energy and for the optimization of the geometric configuration of the system.

The calculations were performed in the generalized gradient approximation using the Perdew–Burke–Ernzerhof parameterization [28]. Norm-conserving nonlocal pseudopotentials were used to describe electrons in the atomic framework [29–31]. The required basis set of plane waves was specified by the kinetic energy cut-off parameter (so-called cutoff energy) equal to 60 Ry. Test calculations demonstrated that the use of a higher cutoff energy changed the total energy by less than 1 meV.

We performed the test calculations of the equilibrium geometry, unit-cell parameter, and phonon frequencies at the point $\mathbf{q} = \Gamma$ of the reciprocal space of an AIP crystal with the zinc-blende structure. The results of these calculations allowed us to conclude that the pseudopotentials used are applicable to the subsequent calculations. The calculated Al–P bond length of 2.34 Å and the unit-cell parameter of 5.50 Å are in excellent agreement with the experimental values of 2.36 and 5.45 Å, respectively [32]. The calculated frequency of a transverse optical mode at the point Γ was equal to 13.25 THz, which is also consistent with the experimental value of 13.17 THz. Thus, these pseudopotentials are suitable for calculating new AIP structures. The atomic coordinates and unit-cell parameters were optimized using the BFGS method [33] until the forces acting on the atoms and the mechanical stresses in the cell became lower than 2.5×10^{-3} eV/Å and 3×10^{-3} GPa, respectively. During the geometry optimization of nanotubes, 6 k points in the Brillouin zone were used. For each particular calculated structure, it was

found that a further increase in the number of k points changed the total energy by less than 1 meV. The Monkhorst–Pack method [34] was used for the generation of k points.

We began our study with the determination of the equilibrium geometry of AIP nanotubes. The calculated average length of the Al–P bond in the nanotubes was 2.30 Å, which is shorter than the experimental bond length of 2.36 Å [32] in a crystal of AIP with the zinc-blende structure. Similarly to other types of nanotubes composed of Group III and Group V elements [35], AIP nanotubes exhibited distorted tubular structures in which aluminum and phosphorus atoms were shifted inward to the axis and outward to the nanotubes, respectively. Figure 1 shows the optimized structures of AIP nanotubes of the zigzag (6,0) and armchair (4,4) types (Figs. 1a and 1b, respectively). Here, the notation of nanotube types [armchair (n, n) and zigzag ($n, 0$)] is equivalent to the notation for carbon nanotubes [21], as well as to that used previously for the description of non-carbon nanotubes [8]. It can be seen in Fig. 1 that these nanotubes consist of two cylindrical layers, in which the inner and outer cylinders are composed of aluminum and phosphorus atoms, respectively.

Since a nanotube is a graphene layer rolled into a cylinder, we simulated and calculated the cohesive energy of a graphene-like layer composed of Al and P. An AIP supercell containing 96 atoms in the atomic plane was used for the geometry optimization of this layer. In the calculation of an equilibrium geometry, we used 18 k points equivalent to a $6 \times 6 \times 1$ mesh of k points generated by the Monkhorst–Pack method [34]. To evaluate the stability of this graphene-like AIP layer, we calculated its cohesive energy E_c . We compared this energy with the value of E_c calculated for an AIP crystal. The cohesive energy of the AIP crystal is -8.57 eV/atom, which is consistent with both the experimental value of -8.41 eV/atom and other *ab initio* data [36]. The value of E_c calculated for a two-dimensional AIP graphene-like structure was -7.63 eV/atom, which is higher than E_c for the AIP crystal by 0.94 eV/atom. This difference between the cohesion energies of the crystalline and two-dimensional forms is also significant in comparison with analogous differences for GaN (0.36 eV/atom) [11] and AlN (0.68 eV/atom) [12] structures. Thus, we can conclude that the graphene-like AIP structure is less energetically stable than the AIP crystal. The calculated Al–P bond length in the two-dimensional structure was 2.30 Å, which is shorter than the corresponding value calculated for the crystal of AIP (2.34 Å).

At the next stage, we determined the strain energies E_{str} required for the formation of nanotube structures with different diameters from a corresponding flat prototype. This energy E_{str} can be calculated as the difference between the specific energies of AIP in a flat atomic layer and a nanotube. Figure 2 demonstrates the dependence of the strain energy E_{str} of AIP nanotubes

on the mean diameter D . It can be seen in Fig. 2 that the energy E_{str} decreases with increasing the diameter of the nanotubes. The best power approximation of these data was provided by $E_{\text{str}} \sim 10.71/D^{2.31}$ (dashed line in Fig. 2) for the armchair nanotubes and $E_{\text{str}} \sim 10.66/D^{1.46}$ (solid line in Fig. 2) for the zigzag nanotubes. It can be seen that these relationships deviate from a characteristic law of $1/D^2$; however, the numerical coefficients are nearly equal. This property indicates that the bending moduli of two types of AIP nanotubes are nearly identical.

The table summarizes the main parameters (diameter, Al–P bond length, and strain energy) of several AIP nanotubes. The tabulated results of the calculations indicate that the zigzag-type nanotubes exhibited somewhat lower energies (by approximately 0.005–0.01 eV/AIP) at equal nanotube diameters. This result is consistent with conclusions drawn for BN and GaN nanotubes [11, 35], in which the zigzag type is energetically the most favorable. Thus, we can conclude that the zigzag-type nanotubes composed of Group III and Group V elements are energetically preferable. However, this energy difference for AIP nanotubes is insignificant (~ 0.01 eV/AIP).

It is also of interest to compare the electronic structure of AIP nanotubes (quasi-one-dimensional systems) with the band structure of the AIP crystal. For this purpose, we calculated the electronic structure of an AIP crystal with the zinc-blende structure. The calculations demonstrated that this crystal is a semiconductor with a band gap equal to 1.54 eV and an indirect transition between the top of the valence band and the bottom of the conduction band. This value is lower than the experimental value of 2.45 eV by 0.91 eV. This is a well-known problem of the DFT method, which underestimates the energy gap E_g . The gap can be corrected by the addition of a quantity obtained by calculating an

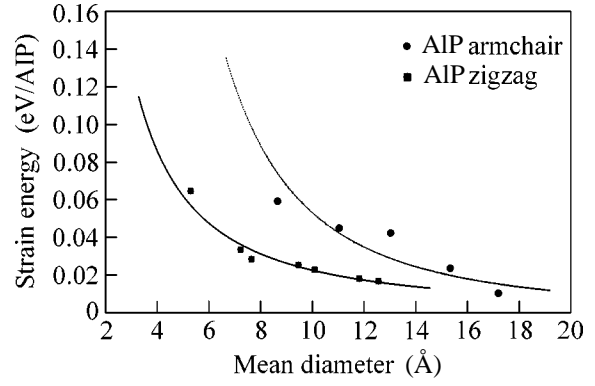


Fig. 2. Specific strain energy E_{str} of AIP nanotubes vs. the mean diameter D .

energy gap for known semiconductors to the calculated value of E_g and comparing this E_g with the experimental value [37]. Note that the value of E_g obtained by this method is an approximate value, which is close to the true value. The use of this method allowed us to considerably shorten the computation time, as compared with the quasiparticle GW approximation, which is more accurate but more resource-consuming [38]. In this case, this addition is 0.91 eV. Figure 3 shows the electronic densities of states and the electronic band structures of the nanotubes (a) (6,0) and (b) (4,4). It is seen in Fig. 3 that these structures are wide-band-gap semiconductors with band gaps of 1.77 and 2.48 eV (2.61 and 3.39 eV after corrections), respectively, with direct [for the AIP nanotube (6,0)] and indirect [for the AIP nanotube (4,4)] transitions between the top of the valence band and the bottom of the conduction band. The table also summarizes the energy gaps of AIP nanotubes depending on the nanotube diameters. As is seen in the table, the band gap of AIP nanotubes behaves

Main parameters (inner diameter D_{in} , outer diameter D_{out} , Al–P bond length, strain energy E_{str} , band gap E_g , and corrected band gap E_g^{cor}) of AIP nanotubes

Structure	D_{in} , Å	D_{out} , Å	Al–P bond length, Å	E_{str} , eV/AIP	E_g , eV	E_g^{cor} , eV
slab	–	–	2.30	0.00	2.82	3.73
(4, 0)	4.64	5.94	2.31	0.065	1.14	2.05
(6, 0)	7.06	8.21	2.30	0.017	1.77	2.68
(7, 0)	8.94	9.98	2.30	0.018	1.98	2.89
(8, 0)	9.56	10.62	2.30	0.023	2.02	2.93
(10, 0)	12.08	13.00	2.29	0.034	2.11	3.02
(4, 4)	8.08	9.24	2.30	0.013	2.48	3.39
(5, 5)	10.53	11.54	2.29	0.024	2.56	3.47
(6, 6)	12.11	13.52	2.29	0.044	2.63	3.54
(7, 7)	14.88	15.66	2.29	0.043	2.68	3.59
(8, 8)	16.94	17.43	2.29	0.059	2.70	3.61

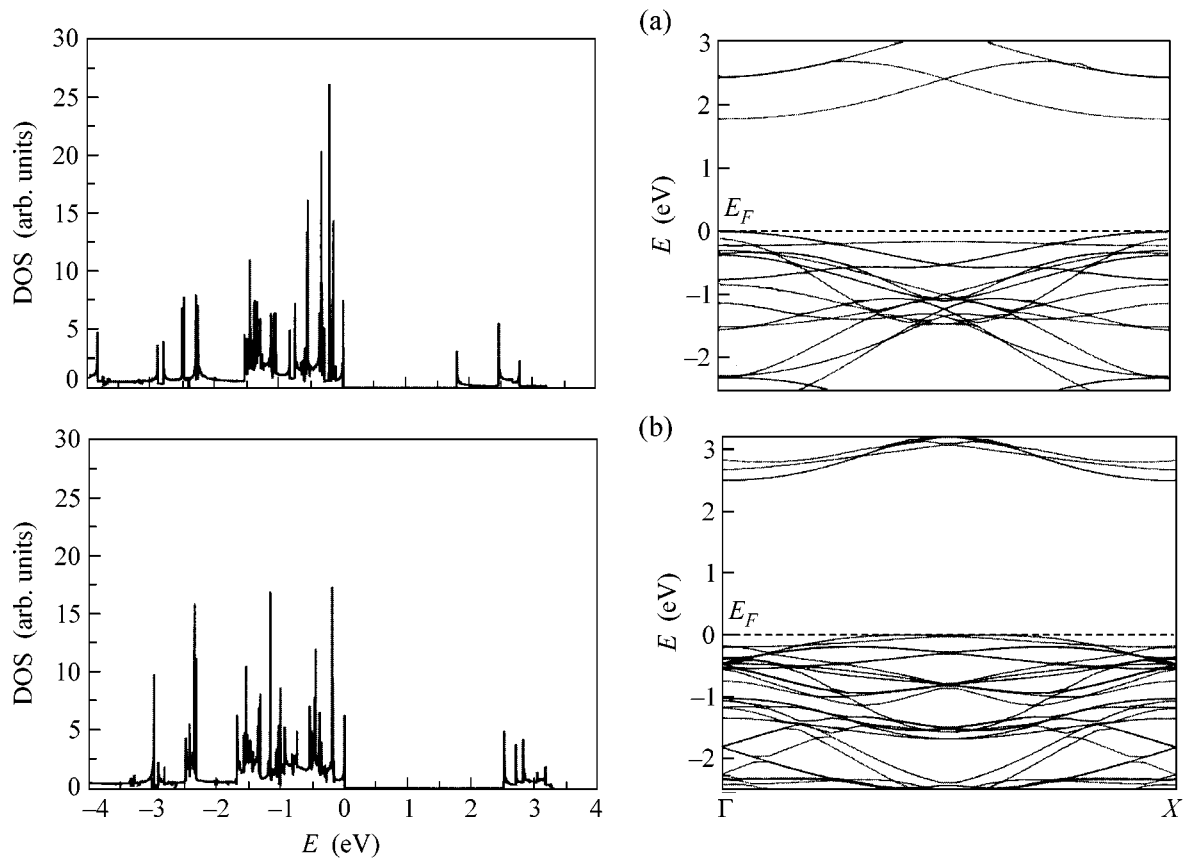


Fig. 3. Electronic density of states (DOS) and electronic band structure of (a) zigzag (6,0) or (b) armchair (4,4) AIP nanotubes. The Fermi level E_F was taken to be zero.

analogously to that of other nanotube structures. Namely, the band gap increases with the tube diameter, approaching the band gap of a flat layer. A detailed calculation of the electronic structure of AIP nanotubes demonstrated that they are wide-band-gap semiconductors and the zigzag and armchair types are characterized by direct and indirect transitions between the top of the valence band and the bottom of the conduction band, respectively. Note that this result is analogous to the results obtained for GaN [11] and AlN [12] nanotubes.

Thus, according to the *ab initio* calculations, we can conclude that AIP nanotubes are stable structures and a low strain energy E_{str} (about 0.1 eV) is required for the formation of these nanotubes. It is also evident that the electronic properties of AIP nanotubes and carbon nanotubes [22] are essentially different. For example, the energy gap E_g for the carbon nanotube (8,0) is about 0.8 eV, whereas E_g is 2.93 eV for the AIP nanotube (8,0). The energy gap E_g in AIP nanotubes is also smaller than E_g in BN nanotubes by approximately 2.2 eV. In other words, the AIP nanotubes proposed above are new nanotube materials with properties intermediate between carbon and BN nanotubes. The geometric structure of AIP nanotubes allowed us to con-

sider them as corrugated or composed of two sublattices of aluminum and phosphorus atoms, respectively. A structural deformation of these tubes can result in the appearance of an additional polarization of the entire structure. All of the above factors may be favorable for the use of AIP nanotubes in nanoelectronic devices.

We are grateful to Wu Rongqin for placing pseudopotentials at our disposal. The calculations were performed by S.V.L. at the Russian Joint Supercomputer Center of Russia and at the Computer Research Center, Moscow State University. This work was supported in part by the Russian Foundation for Basic Research (project nos. 04-03-96501 and 05-03-328876) and the Russian Academy of Sciences (program “Fundamental Problems of the Physics and Chemistry of Nanosized Systems and Materials”).

REFERENCES

1. S. Iijima, *Nature* **354**, 56 (1991).
2. M. S. Dresselhaus, G. Dresselhaus, and P. C. Eklund, *Science of Fullerenes and Carbon Nanotubes* (Academic, San Diego, 1996).

3. P. J. F. Harris, *Carbon Nanotubes and Related Structures: New Materials for the Twenty-first Century* (Cambridge Univ. Press, Cambridge, 1999; Tekhnosfera, Moscow, 2003).
4. R. Tenne, L. Margulis, M. Genut, and G. Hodes, *Nature* **360**, 444 (1992).
5. V. V. Pokropivny, *Powder Metall. Met. Ceram.* **40**, 485 (2001).
6. V. V. Pokropivny, *Powder Metall. Met. Ceram.* **40**, 582 (2001).
7. A. L. Ivanovskii, *Usp. Khim.* **71**, 203 (2002).
8. A. Rubio, J. L. Corkill, and M. L. Cohen, *Phys. Rev. B* **49**, 5081 (1994).
9. X. Blase, A. Rubio, S. G. Louie, and M. L. Cohen, *Europhys. Lett.* **28**, 335 (1994).
10. N. G. Chopra, R. J. Luyken, K. Cherry, *et al.*, *Science* **269**, 996 (1995).
11. S. M. Lee, Y. H. Lee, Y. G. Hwang, *et al.*, *Phys. Rev. B* **60**, 7788 (1999).
12. M. Zhao, Y. Xia, D. Zhang, and L. Mei, *Phys. Rev. B* **68**, 235415 (2003).
13. M. Menon, E. Richter, A. Mavrandonakis, *et al.*, *Phys. Rev. B* **69**, 115322 (2004).
14. Th. Kohler, Th. Frauenheim, Z. Hajnal, and G. Seifert, *Phys. Rev. B* **69**, 193403 (2004).
15. R. T. Senger, S. Dag, and S. Ciraci, *Phys. Rev. Lett.* **93**, 196807 (2004).
16. L. A. Chernozatonskii, *Pis'ma Zh. Éksp. Teor. Fiz.* **80**, 732 (2004) [*JETP Lett.* **80**, 628 (2004)].
17. D. Golberg, Y. Bando, W. Han, *et al.*, *Chem. Phys. Lett.* **308**, 337 (1999).
18. D. Golberg, Y. Bando, L. Bourgeois, *et al.*, *Appl. Phys. Lett.* **77**, 1979 (2000).
19. J. Goldberger, R. He, Y. Zhang, *et al.*, *Nature* **422**, 599 (2003).
20. Y. Oshima, A. Onga, and K. Takayanagi, *Phys. Rev. Lett.* **91**, 205503 (2003).
21. N. Hamada, S. Sawada, and A. Oshiyama, *Phys. Rev. Lett.* **68**, 1579 (1992).
22. R. Saito, M. Fujita, G. Dresselhaus, and M. S. Dresselhaus, *Phys. Rev. B* **46**, 1804 (1992).
23. P. Hohenberg and W. Kohn, *Phys. Rev.* **136**, 864 (1964).
24. X. Gonze, J.-M. Beuken, R. Caracas, *et al.*, *Comput. Mater. Sci.* **25**, 478 (2002).
25. S. Goedecker, *SIAM J. Sci. Comput. (USA)* **18**, 1605 (1997).
26. M. C. Payne, M. P. Teter, D. C. Allan, *et al.*, *Rev. Mod. Phys.* **64**, 1045 (1992).
27. X. Gonze, *Phys. Rev. B* **55**, 10 337 (1997).
28. J. P. Perdew, K. Burke, and M. Ernzerhof, *Phys. Rev. Lett.* **77**, 3865 (1996).
29. M. Fuchs and M. Scheffler, *Comput. Phys. Commun.* **119**, 67 (1999).
30. N. Troullier and J. L. Martins, *Phys. Rev. B* **43**, 1993 (1991).
31. L. Kleinman and D. M. Bylander, *Phys. Rev. Lett.* **48**, 1425 (1982).
32. S. S. Mitra and N. E. Massa, *Handbook on Semiconductors*, Ed. by W. Paul (North-Holland, Amsterdam, 1982), Vol. 1, p. 81.
33. H. B. Schlegel, *J. Comput. Chem.* **3**, 214 (1982).
34. H. J. Monkhorst and J. D. Pack, *Phys. Rev. B* **13**, 5188 (1976).
35. M. Menon and D. Srivastava, *Chem. Phys. Lett.* **307**, 407 (1999).
36. B. Paulus, P. Fulde, and H. Stoll, *Phys. Rev. B* **54**, 2556 (1996).
37. X. Blase, A. Rubio, S. G. Louie, and M. L. Cohen, *Phys. Rev. B* **51**, 6868 (1995).
38. W. G. Aulbur, L. Jonsson, and J. W. Wilkins, *Solid State Phys.* **54**, 1 (2000).

Translated by V. Makhlyarchuk

Low-Temperature Thermal Transport in Nanowires[†]

A. V. Zhukov^{1,2}, S. Yang², and J. Cao²

¹ *Department of Chemistry, University of Western Ontario, London, Ontario, N6A 5B7, Canada*

² *Department of Chemistry, Massachusetts Institute of Technology, Cambridge, MA 02139, USA*

e-mail: ozhukov@uwo.ca, jianshu@mit.edu

Received October 27, 2004; in final form, January 27, 2005

We propose a theory of low temperature thermal transport in nanowires in a regime in which competition between a phonon and flexural modes governs the relaxation processes. Starting with the standard kinetic equations for two different types of quasiparticles, we derive a general expression for the coefficient of thermal conductivity. The underlying physics of thermal conductance is completely determined by the corresponding relaxation times, which can be calculated directly for any dispersion of quasiparticles, depending on the size of a system. We show that, if the considered relaxation mechanism is dominant, then at small wire diameters the temperature dependence of thermal conductivity experiences a crossover from $T^{1/2}$ to T^3 -dependence. Quantitative analysis shows reasonable agreement with recent experimental results. © 2005 Pleiades Publishing, Inc.

PACS numbers: 63.20.Kr, 63.22.+m, 65.40.-b

Low-dimension materials have attracted considerable attention in recent years, particularly in view of their potential applications in electronic devices [1, 2]. Many theoretical and experimental studies of nanowires and nanotubes are centered on the properties of electronic transport. However, it is now realized that the thermal properties of nanomaterials are also important for applications [3–5]. It is of special interest to increase thermal conductance in micro- and nanodevices [1, 6, 7]. In this paper, we study thermal transport in nonmetallic systems, in which heat is transported by thermal excitations only. In addition to the practical importance of such studies, thermal transport in nanowires is interesting from the fundamental point of view. Recent theoretical [8] and experimental [9] findings proved the existence of a quantum of thermal conductance in ballistic regime, which is similar to a quantum of electronic conductance. The state of experimental and theoretical understanding of thermal transport in nanoscale systems is comprehensively discussed in review [10]. Recently, D. Li *et al.* [11] reported an accurate measurement of lattice thermal conductivity in silicon nanowires for a wide range of temperatures and wire diameters. They demonstrated a significant influence of the system size not only on the magnitude of the thermal conductivity coefficient, but also on its temperature dependence. It is well known that, for large enough diameters of the wire and diffusive phonon-boundary scattering, the thermal conductivity coefficient at low temperatures is proportional to T^3 . But for small values of the wire diameters, experiment [11] shows a clear crossover from cubic to near linear dependence on the temperature. In the present paper,

we consider one particular relaxation mechanism that can explain the observed crossover.

Recently, Mingo [12] carried out an accurate numerical study of the thermal conductance of silicon nanowires to explain the decrease of the thermal conductivity coefficient with wire diameter observed in the experiment. He assumed that all the effects can be explained by the reconstruction of the phonon dispersion, where realistic phonon modes obtained from MD simulations were applied to general expression of the thermal conductivity coefficient. His numerical analysis shows excellent quantitative agreement with experiment [11] for large enough diameters at high temperatures. As the system size becomes smaller, the approach fails to describe a sharp decrease of thermal conductance as well as qualitative change of its temperature dependence. This is likely because Matheissen's rule has been used for evaluation of the phonon lifetime, which has rather restricted range of applicability (see, e.g., [13] and references therein).

As was noted in [14], a decrease of the temperature increases the characteristic phonon wavelength and reduces the scattering probability at the boundary surface. This leads to a modification of the phonon spectrum. For ideal wires, this is represented by a set of branches with energies proportional to a one-dimensional (1D) momentum directed along the wire. Thus, the standard theory of thermal conductance in dielectrics and semiconductors has to be modified to account for low dimensionality effects as well as phonon spectrum modification at low temperatures. Thus, to understand thoroughly the physical processes occurring inside the nanowires with decreasing sizes, we need an analytical theory to account for different mechanisms

[†]This article was submitted by the authors in English.

explicitly, such as dispersion reconstruction and restricted geometry.

To approach the problem, we consider sufficiently low temperatures in which the quasiparticle states of “acoustic” branches are thermally populated ($\epsilon \rightarrow 0$ when $p \rightarrow 0$). The corresponding acoustic branches have the following dispersion relations [14, 15]:

$$\epsilon_1 = u_1 p_1, \quad \epsilon_2 = u_2 a p_2^2, \quad (1)$$

where ϵ_i stands for the energy of a quasiparticle, p_i is the corresponding momentum, a is the wire diameter, and u_1 and u_2 are the characteristic velocities. The first expression in Eq. (1) is the phonon dispersion, and the second expression is the dispersion of the flexural mode. The nature of flexural modes comes from the fact they are analogous to the bending modes of classical elasticity theory or to the antisymmetric Lamb waves of a free plate [16]. The appearance of such a mode is just a direct consequence of restricted geometry, and under some conditions it can be considered as the only size effect in thermal transport properties. Strictly speaking, there are two modes for each type of dispersion, but we do not account for them separately since their contributions are qualitatively the same. Consequently, we need to solve the kinetic problem for a two-component gas of quasiparticles. It is well known [13, 17–20] that using a simple Callaway formula to estimate the thermal conductivity coefficient in two-component systems sometimes leads to serious confusions. Simple summation of the relaxation rates, as is done in the majority of theoretical works, is questionable under many physical conditions. The dependence of the kinetic coefficients on different relaxation times is much more complicated in reality. An accurate method for calculation of the diffusion coefficient in a two-component gas of quasiparticles was proposed in [20]. Here, we extend this formalism to the thermal conductance problem. To start with, we consider a system of two types of quasiparticles. Their kinetics is described by equations for corresponding distribution functions f_i :

$$v_i \frac{\partial f_i}{\partial z} = \sum_{j=1}^2 C_{ij}(f_i, f_j) + C_{i3}(f_i), \quad i = 1, 2, \quad (2)$$

where $C_{ij}(f_i, f_j)$ is the collision integral of thermal excitations and $C_{i3}(f_i)$ is the collision integral describing the scattering processes between quasiparticles and scatterers; $v_i = \partial \epsilon_i / \partial p_i$ is the group velocity of the corresponding thermal excitation. The main purpose of our theory is to obtain analytic expressions of thermal conductance, which are applicable to quasiparticles with arbitrary dispersion relations. In other words, the explicit dispersion relations in Eq. (1) are needed only at the last stage when calculating corresponding relaxation times and thermodynamic quantities. As usual, we seek a perturbative solution of system (2) in the form

$$f_i = f_i^{(0)} + \delta f_i, \quad (3)$$

where $f_i^{(0)}$ is the local equilibrium Bose-function and $\delta f_i \ll f_i^{(0)}$ represents a small deviation from the equilibrium. The perturbation term can be conveniently chosen to be $\delta f_i = -g_i \partial f_i^{(0)} / \partial \epsilon_i$ with g_i the new target functions. After the standard linearization procedure, Eq. (2) can be written in the following matrix form:

$$|\phi_\kappa\rangle \frac{1}{T} \frac{\partial T}{\partial z} = \hat{\mathcal{C}} |g\rangle, \quad (4)$$

where

$$|\phi_\kappa\rangle = \begin{pmatrix} \epsilon_1 v_1 \\ \epsilon_2 v_2 \end{pmatrix}, \quad |g\rangle = \begin{pmatrix} g_1 \\ g_2 \end{pmatrix}.$$

The two-dimensional (2D) collision matrix $\hat{\mathcal{C}}$ can be decomposed into a sum of three terms, corresponding to different relaxation mechanisms— $\hat{\mathcal{C}} = \hat{\mathcal{F}} + \hat{\mathcal{S}} + \hat{\mathcal{U}}$ —where $\hat{\mathcal{F}}$, with matrix elements $\mathcal{F}_{ij} = C_{ik} \delta_{ij} + C_{ij}(1 - \delta_{ij})$ ($k \neq i$), describes the relaxation due to interaction between quasiparticles of different types; $\hat{\mathcal{S}}$ ($\mathcal{S}_{ij} = C_{ii} \delta_{ij}$) describes collisions between identical quasiparticles; and $\hat{\mathcal{U}}$ ($\mathcal{U}_{ij} = C_{i3} \delta_{ij}$) describes all the other relaxation mechanisms, including scattering on defects, boundaries, umklapp processes, etc. Here, C_{ij} represent *linearized* collision operators [20].

Let us define the scalar product of two-dimensional bra- and ket-vectors as follows [20]:

$$\langle \phi | \chi \rangle = \sum_{k=1,2} (\phi_k | \chi_k) = - \sum_{k=1,2} \int \phi_k^* \chi_k \frac{\partial f_k^{(0)}}{\partial \epsilon_k} d\Gamma_k, \quad (5)$$

where $(\phi_k |$ and $|\chi_k)$ are the correspondent one-component vectors and $d\Gamma$ is the element of phase volume.

Under this condition, the collision operator $\hat{\mathcal{C}}$ becomes hermitian. System (4) is a system of nonuniform linear integral equations. According to the general theory of integral equations, the target solution $|g\rangle$ must be orthogonal to the solution of corresponding uniform equations $\hat{\mathcal{C}} |\phi_{\text{uni}}\rangle$. It is therefore convenient to write the formal solution of (4) so that the orthogonality condition ($\langle g | \phi_{\text{uni}} \rangle$) is imposed explicitly in the solution. For this purpose we define the projection operator $\hat{\mathcal{P}}_n$ onto the subspace orthogonal to the vector $|\phi_{\text{uni}}\rangle$, $\hat{\mathcal{P}}_n = 1 - \hat{\mathcal{P}}_c$, $\hat{\mathcal{P}}_c = |\phi_{\text{uni}}\rangle \langle \phi_{\text{uni}}|$. As a result, the formal solution of system (4) can be written in the form

$$|g\rangle = \hat{\mathcal{P}}_n (\hat{\mathcal{C}}^{-1}) \hat{\mathcal{P}}_n |\phi_\kappa\rangle \frac{1}{T} \frac{\partial T}{\partial z}. \quad (6)$$

The heat flux density due to thermal excitations of different types is given by the expression $Q = \sum_{k=1,2} \int \epsilon_k v_k f_k d\Gamma_k$. Using relation (3) and the definition of scalar product (5), Q can be rewritten as $Q = \langle \phi_k | g \rangle$. On the other hand, the effective thermal conductivity coefficient is defined by the relation $Q = -\kappa_{\text{eff}} \partial T / \partial z$. Comparing the above two expressions for Q and using formal solution (6), we obtain

$$\kappa_{\text{eff}} = -\frac{1}{T} \langle \phi_k | \hat{\mathcal{C}}^{-1} | \phi_k \rangle. \quad (7)$$

To derive an exact and analytical expression for thermal conductivity coefficient (7), it is necessary to introduce a complete set of orthonormal 2D vectors $|\psi_n\rangle$ ($n = 1, 2, 3, \dots$) belonging to an infinite-dimensional Hilbert space with scalar product (5). In principle, the particular choice of the basis is not essential, but for convenience of calculations it is useful to specify at least four of them. It is convenient to choose the first of them as corresponding to the total momentum of quasiparticles and the second as orthogonal, but still linear in momentum [20]:

$$|\psi_1\rangle = \frac{1}{\sqrt{\rho}} \begin{pmatrix} p_1 \\ p_2 \end{pmatrix}, \quad |\psi_2\rangle = \frac{1}{\sqrt{\rho p_1 p_2}} \begin{pmatrix} \rho_2 p_1 \\ -\rho_1 p_2 \end{pmatrix}, \quad (8)$$

where $\rho_i = (p_i | p_i)$ is the normal density of the i th component, $\rho = \rho_1 + \rho_2$. The third and the fourth vectors correspond to the energy flux,

$$|\psi_3\rangle = \frac{1}{\mathcal{N}_{\kappa 1}} \begin{pmatrix} \Psi_{\kappa 1} \\ 0 \end{pmatrix}, \quad |\psi_4\rangle = \frac{1}{\mathcal{N}_{\kappa 2}} \begin{pmatrix} 0 \\ \Psi_{\kappa 2} \end{pmatrix}, \quad (9)$$

where

$$\Psi_{\kappa j} = \frac{1}{\sqrt{T}} \left(\epsilon_j v_j - \frac{S_j T}{\rho_j} p_j \right), \quad (10)$$

and $\mathcal{N}_{\kappa j} = \sqrt{\langle \Psi_{\kappa j} | \Psi_{\kappa j} \rangle}$ is the corresponding normalization coefficient. The partial entropy of quasiparticle subsystem S_j in Eq. (10) is given by the relation

$$S_j = \frac{1}{T} (\epsilon_j v_j | p_j). \quad (11)$$

Formally, the kinetic problem of a two-component quasiparticles system can be solved in the above basis set. The inversion of the operator matrix $\hat{\mathcal{C}}$ in Eq. (7) is similar to the procedure described in [20]. The final result contains infinite-dimensional nondiagonal matrices. To obtain closed form expressions, we must use some approximations, a correct τ -approximation [19] or Kihara approximation [20–23]. In some physical situations, we are able to obtain closed analytical expressions. It is rigorously proved in [20] that, in the case of quasi-equilibrium within each subsystem of quasiparti-

cles, the corresponding transport coefficient can be obtained in close analytical form. This is a reliable approximation when the low temperature relaxation is mainly governed by defect scattering processes. The approximation formally implies that all the matrix elements of matrix $\hat{\mathcal{C}}$ in Eq. (7) tend to infinity. The thermal conductivity coefficient in this case can be obtained in the form $\kappa_{\text{eff}} = \kappa_F + \kappa_D$. Here we separate the flux part of thermal conductivity coefficient $\kappa_F = \tau_F S^2 T / \rho$ with $S = S_1 + S_2$, which approaches infinity when the quasiparticles do not interact with scatterers, and the diffusive part $\kappa_D = \tau_D (S_1 T / \rho_1 - S_2 T / \rho_2)^2 \rho_1 \rho_2 / T \rho$. The corresponding relaxation times are given by

$$\tau_D = \left\{ \frac{\rho_1}{\rho} \tau_{23}^{-1} + \frac{\rho_2}{\rho} \tau_{13}^{-1} + \tau_{12}^{-1} + \tau_{21}^{-1} \right\}^{-1}, \quad (12)$$

and

$$\tau_F = \tau_D \left(\frac{S_1}{S} \tau_{23}^{-1} + \frac{S_2}{S} \tau_{13}^{-1} + \tau_{12}^{-1} + \tau_{21}^{-1} \right)^2 \times (\tau_{13}^{-1} \tau_{23}^{-1} + \tau_{12}^{-1} \tau_{23}^{-1} + \tau_{21}^{-1} \tau_{13}^{-1})^{-1}. \quad (13)$$

Relaxation times contained in formulas (12) and (13) are defined by

$$\tau_{kj}^{-1} = \frac{1}{\rho_k} (p_j | C_{kj} | p_j). \quad (14)$$

We emphasize that these are not actual scattering times, which are momentum dependent, but relaxation times associated with the corresponding scattering mechanisms. Once we obtain the particular scattering rate $v_{kj}(p_k)$ from standard scattering theory, we can replace the true collision operator C_k with $v_{kj}(p_k)$, so that the corresponding relaxation time can be calculated by

$$\tau_{kj}^{-1} = \rho_k^{-1} \int p_k^2 v_{kj}(p_k) \frac{\partial f_k^{(0)}}{\partial \epsilon_k} d\Gamma_k. \quad (15)$$

As can be seen from the derived formulas, the coefficient of thermal conductivity contains different relaxation times in a rather nontrivial combination. If one component (say set $S_2 = 0, \rho_2 = 0$) drops out, we recover the usual result, $\kappa_F^{(1)} = \tau_{13} S_1^2 T / \rho_1$. For phonons with linear dispersion $\epsilon = vp$, κ_F reduces to the well-known result $\kappa_F^{\text{ph}} = C_{\text{ph}} v^2 \tau_{13} / 3$, where $C_{\text{ph}} = 3S_{\text{ph}}$ is the heat capacity of phonon gas.

The main advantage of our approach is its universality. In fact, up to this point we have not restricted ourselves to any particular dimensionality of the system or any quasiparticles dispersion. All the necessary information is contained in the corresponding relaxation times and thermodynamic quantities. This formalism allows us to analyze contributions from different relaxation mechanisms to the total thermal conductivity

coefficient. Given the dispersion relations of quasiparticles, we can easily calculate all the quantities contained in (12) and (13).

With Eqs. (12) and (13), we are able to address the competition between relaxation processes of the flexural and phonon modes. Glavin [14] noted that such a competition can be essential at extremely low temperatures if the dominant relaxation mechanism is elastic scattering on defects, where, he argued, the thermal conductivity coefficient would scale as $T^{1/2}$. Our approach allows us to study this competition comprehensively. In particular, we predict a strong dependence of the temperature scaling exponent on the wire diameter. The standard Fermi golden rule approach [14] gives the momentum dependent scattering rates for different

modes $v_{13} = W_{13} \frac{p^{1/2}}{u_1 a^{3/2}}$, $v_{23} = W_{23} \frac{1}{pu_2 a^3}$, where W_{kj} are

the corresponding scattering amplitudes, which depend on the physical properties of particular material. Using Eq. (15), it is easy to show that the corresponding relaxation times scale as

$$\tau_{13}^{-1} \propto a^{-3/2} T^{1/2}, \quad \tau_{23}^{-1} \propto a^{-5/2} T^{-1/2}. \quad (16)$$

Different temperature dependences of relaxation times lead to a strong competition between two physically different mechanisms of thermal conductivity—flux and diffusive. The dominance of one over the other strongly depends on the wire diameter at a given temperature. To make some specific conclusions, let us summarize the approximations done and specify the range of validity of the proposed theory. We consider a situation in which thermal excitations are multiply scattered elastically while being transferred through the wire, so that other scattering mechanisms are strongly suppressed by interaction with defects. Only for this case were we able to drop relaxation within each subsystem of identical quasiparticles to obtain closed expressions (12) and (13). The influence of the boundary is accounted for in the dispersion of the flexural mode and in the dimensionality of the system. The range of temperature is supposed to satisfy the relation $T < \Delta\epsilon$, where $\Delta\epsilon \sim 1/a$ is the characteristic value of the frequency gap between the adjacent phonon branches. For a larger temperature, we cannot use acoustic modes (1) only, but need to account for higher branches.

In Fig. 1, we compare our theoretical results with the experimental data from [11]. We have chosen the unknown parameters $W_{13} = 1.2 \times 10^{-44} \text{ m}^5 \text{ s}^{-4}$ and $W_{23} = 0.9 \times 10^{-44} \text{ m}^5 \text{ s}^{-4}$ to fit data for $a = 22 \text{ nm}$. Deviations from the experimental data for large diameters and temperatures show the restriction of the applicability of our initial approximations. They arise from the Debye approximation and simplified dispersion expression. Additionally, when the diameter of the wire increases, the mechanism we consider becomes less dominant. To be more precise, we need to include higher excitation branches as well as other relaxation mechanisms. How-

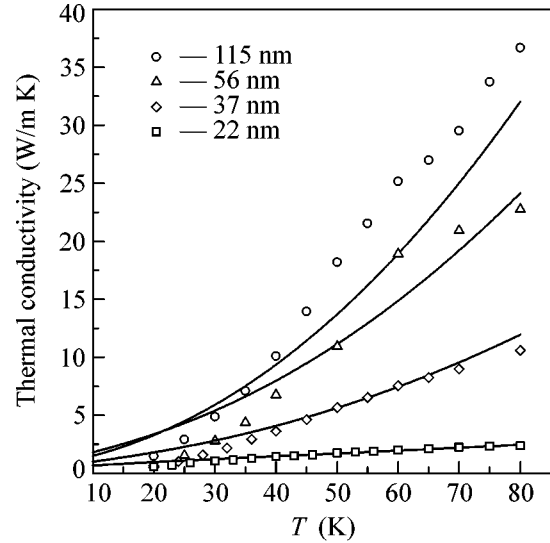


Fig. 1. Thermal conductivity coefficient calculated from Eqs. (12) and (13) for different values of nanowire diameter. Experimented data are from [11].

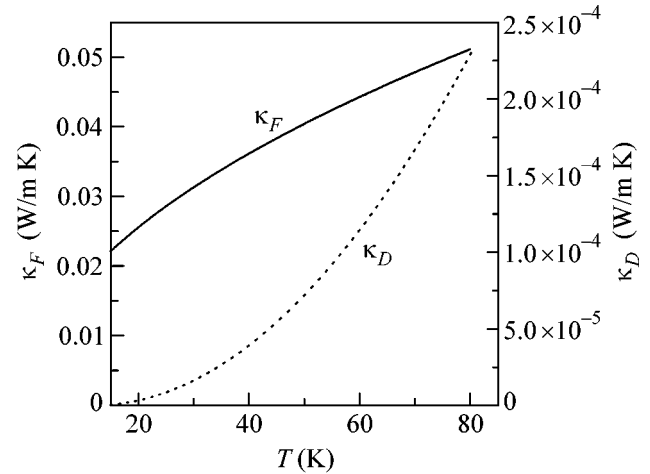


Fig. 2. Comparative contribution from flux and diffusive parts of thermal conductivity for a 2-nm wire.

ever, our approach allows us to understand the physics of the processes in the region under consideration. It is clear that the observed crossover is the result of competition between $\kappa_F \propto T^{1/2}$ and $\kappa_D \propto T^3$. For smaller diameters, κ_F is strongly dominant in a wide range of temperatures as shown on Fig. 2 for wire diameter $a = 2 \text{ nm}$. Figure 3 demonstrates a complete crossover from $T^{1/2}$ to T^3 dependence for a nanowire of $a = 30 \text{ nm}$. It can be seen that the T dependence between 20 and 40 K is nearly linear, which was observed in experiment [11]. It should be noted that T^3 dependence of κ_D cannot be interpreted by simple analogy with the bulk case. It comes not from a specific heat directly, but from differ-

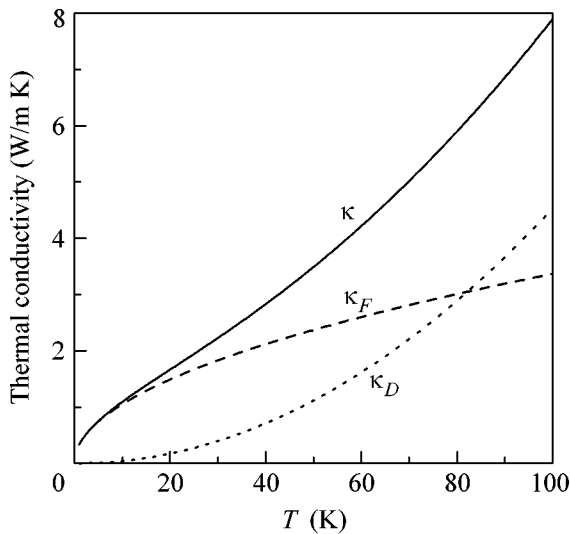


Fig. 3. Crossover from $T^{1/2}$ - to T^3 -dependence of κ_{eff} for a 30-nm wire.

ent sources, including competition of the relaxation times in Eqs. (12) and (13).

In summary, we derived the general analytical expressions (12) and (13) to explicitly calculate the contributions of different scattering mechanisms to the total relaxation of the system. The simple expressions clarify the essential effects leading to the observed behavior of the thermal conductivity coefficient. It is clear that the particular dispersion laws (and their reconstruction) affect scattering rates and thermodynamic quantities. Restricted geometry and low dimensionality lead to additional scattering mechanisms. Note the information about dimensionality is naturally included in the particular form of phase space element $d\Gamma_i$. Such a formalism helps to distinguish effects from different scattering mechanisms. When applied to a regime in which phonon modes compete with flexural ones, our theory agrees favorably with the available experimental data. Furthermore, we showed that the thermal conductivity coefficient changes from approximately $T^{1/2}$ -dependence to T^3 -dependence with increasing temperature. In view of our theoretical results, it will be useful to investigate smaller diameters or lower temperatures with fixed diameters in experiment to better reveal the crossover from T^3 - to $T^{1/2}$ -dependence.

We would like to thank Prof. Peidong Yang and Dr. Deyu Li for providing us with the experimental

data. This research is supported by the NSF Career Award, grant no. Che-0093210. J.C. is a recipient of the Camille Dreyfus Teacher-Scholar Award.

REFERENCES

1. M. A. Ratner, B. Davis, M. Kemp, *et al.*, Ann. (N.Y.) Acad. Sci. **852**, 22 (1998).
2. V. Pouthier, J. C. Light, and C. Girardet, J. Chem. Phys. **114**, 4955 (2001).
3. D. M. Leitner and P. G. Wolynes, Phys. Rev. E **61**, 2902 (2000).
4. A. Buldum, D. M. Leitner, and S. Ciraci, Europhys. Lett. **47**, 208 (1999).
5. L. Hui, B. L. Wang, J. L. Wang, and G. H. Wang, J. Chem. Phys. **120**, 3431 (2004).
6. Y. Cui, Z. Zhong, D. Wang, *et al.*, Nano Lett. **3**, 149 (2003).
7. P. Poncharal, C. Berger, Y. Yi, *et al.*, J. Phys. Chem. B **106**, 12 104 (2002).
8. L. G. C. Rego and G. Kirczenow, Phys. Rev. Lett. **81**, 232 (1998).
9. H. Schwab, E. A. Henriksen, J. M. Worlock, and M. L. Roukes, Nature **404**, 974 (2000).
10. D. G. Cahill, W. K. Ford, K. E. Goodson, *et al.*, Appl. Phys. Lett. **83**, 2934 (2003).
11. D. Li, Y. Wu, P. Kim, *et al.*, Appl. Phys. Lett. **83**, 2934 (2003).
12. N. Mingo, Phys. Rev. B **68**, 113308 (2003).
13. I. N. Adamenko, K. E. Nemchenko, A. V. Zhukov, *et al.*, J. Low Temp. Phys. **111**, 145 (1998).
14. B. A. Glavin, Phys. Rev. Lett. **86**, 4318 (2001).
15. N. Nishiguchi, Y. Ando, and M. N. Wybourne, J. Phys.: Condens. Matter **9**, 5751 (1997).
16. B. A. Auld, *Acoustic Fields and Waves in Solids* (Wiley, New York, 1973).
17. I. N. Adamenko, A. V. Zhukov, and K. E. Nemchenko, Fiz. Nizk. Temp. **22**, 1470 (1996) [Low Temp. Phys. **22**, 1117 (1996)].
18. I. N. Adamenko and K. E. Nemchenko, Fiz. Nizk. Temp. **22**, 995 (1996) [Low Temp. Phys. **22**, 759 (1996)].
19. I. N. Adamenko, K. E. Nemchenko, and A. V. Zhukov, J. Low Temp. Phys. **111**, 387 (1998).
20. A. V. Zhukov, Phys. Rev. E **66**, 041208 (2002).
21. L. Hui, F. Pederiva, G. H. Wang, and B. L. Wang, J. Chem. Phys. **119**, 9771 (2003).
22. T. Kihara, *Imperfect Gases* (Asakusa Bookstore, Tokyo, 1949).
23. E. A. Mason, J. Chem. Phys. **27**, 782 (1957).

Quantum Teleportation of Entanglement Using Four-Particle Entangled States[†]

S. A. Podoshvedov

School of Computational Sciences, Korea Institute for Advanced Study, Seoul, 130-722 South Korea

e-mail: podoshvedov@mail.ru

Received December 2, 2004; in final form, January 12, 2005

We present a model to realise a probabilistic quantum teleportation of two-particle mode entangled state through the four-photon quantum channel. Four modes of the two-photon mode entangled state are directly transferred to other spatial four modes of the quantum channel with success probability of 50%. The quantum protocol operates in space of photon number states. A Bell state measurement with four beam splitters and four pairs of detectors in the teleportation protocol is accomplished in the fourfold coincidence basis. © 2005 Pleiades Publishing, Inc.

PACS numbers: 03.65.Ud

Quantum teleportation, proposed by Bennett *et al.* [1], is the process that transmits an unknown two-state particle from a sender (Alice) to a receiver (Bob) via a quantum channel with help of sending some classical information to Bob. In original scheme [1], such a quantum channel has been represented by a Bell maximally entangled state or Einstein–Podolsky–Rosen (EPR) pair. Experimental realization of the quantum teleportation protocol by a partial set of Bell measurements has been performed in [2] with success probability of 50%. The main difficulty with any optical approach is that nonlinear interactions between individual photons are required in order to implement the quantum teleportation protocol that operates with 100% efficiency [3]. The Bell-state measurement being inherently nonlinear is required for the 100% teleportation [4].

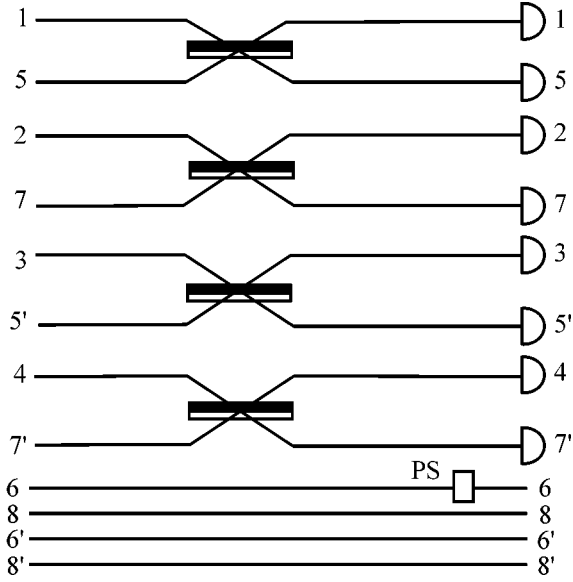
Quantum teleportation of a qubit occupying only one optical mode via one-photon quantum channel was studied in [5]. Experimental realisation of the quantum teleportation of one mode qubit through the one-photon quantum channel is reported in [6]. Problems of quantum teleportation by employing Greenberger–Horne–Zeilinger (GHZ) quantum channel [7] have been studied in [8]. More general questions of quantum teleportation of two qubits involving noisy quantum channels are involved in [9]. One should be noted the work [10], in which quantum teleportation protocol of N —particle entangled state via $N + 1$ —particle quantum channel has been developed.

As pointed out by Bennett *et al.* [1] in their original proposal for quantum teleportation, entanglement can be transferred through teleportation of two modes one of the particles forming the entangled state. This

method, known as entanglement swapping [11], provides only partial teleportation of entanglement. We propose an alternative method in which the two-photon mode entangled state is directly transferred from one place to another. We use four-photon quantum channel to perform the teleportation protocol for the two-photon mode entangled state unlike [8–10]. We make use of the number state representation to perform the total teleportation of the two-photon mode entangled state (all four modes of the state are teleported). One should be noted, it was recently recognised in [12] that spatial encoding is easier, for example, to manipulate and construct universal quantum gates unlike the standard method for encoding qubits in optics in which polarization degrees of freedom of single photon are used. The source of the mode entanglement may consist of two non-collinear degenerated on frequency spontaneous parametric down converters with type-I phase matching (SPDCI) [13]. Quantum teleportation utilizing such four-photon quantum channel is not required special detectors distinguishing between one- and two-photon number states. The teleportation scheme of the entangled state through the four-photon quantum channel may be really performed in practice unlike teleportation schemes based on the GHZ quantum channel [8–10].

We employ setup shown in figure for the teleportation of entanglement. As in the standard teleportation scheme [1], our scheme (figure) consists of three distinct parts: the source station that generates a quantum channel (it is not shown in figure), Alice's station where a Bell state measurement is performed and its result is sent away through the classical communication channel, and Bob's station where the signal from Alice is read and a suitable unitary transformation with output

[†]This article was submitted by the author in English.



The experimental scheme realizes quantum state teleportation of unknown two-photon qubit by the four-photon quantum channel (1). White side of the beam splitter indicates the surface from which a sign change in exiting mode occurs upon reflection. The use of this beam splitter phase convention is convenient but not essential. PS means π -phase shifter in the output sixth mode. Bob's modes are shown at lower part.

state is performed. The four-photon mode entangled state

$$|\Xi_1^{(56785'6'7'8')}\rangle = \frac{1}{\sqrt{2}} \{ |11110000\rangle + |00001111\rangle \}_{56785'6'7'8'} \quad (1)$$

is utilized as a quantum channel which is shared by Alice (modes 5, 7, 5' and 7' in figure belong to Alice) and Bob (modes 6, 8, 6' and 8' in figure). Here, the numbers in the subscripts of the states (Eq. (1)) are referred to the optical modes of the photons [14]. For example, the state $|11110000\rangle_{56785'6'7'8'}$ in Eq. (1) is a tensor product of one-photon number states where the modes 5, 6, 7, and 8 are occupied by four photons while other residual modes 5', 6', 7' and 8' have zero photons. An unknown two-photon mode entangled state $|\Psi_1^{(1234)}\rangle = \{ \alpha|100\rangle + \beta|0011\rangle \}_{1234}$ with amplitudes α and β satisfying condition $|\alpha|^2 + |\beta|^2 = 1$ must be teleported to Bob. According to figure, the first, second, third, and fourth modes of the teleported state $|\Psi_1^{(1234)}\rangle$ are mixed with fifth, seventh, fifth prime, and seventh prime modes of the quantum channel (figure). Then, the input tensor product of six photons is given by

$$|\Psi_1^{(1234)}\rangle |\Xi_1^{(56785'6'7'8')}\rangle$$

$$= \frac{1}{2} \{ |\Xi_1^{(1257345'7')}\rangle \times \{ \alpha|1100\rangle + \beta|0011\rangle \}_{686'8'} + |\Xi_2^{(1257345'7')}\rangle \{ \alpha|1100\rangle - \beta|0011\rangle \}_{686'8'} + |\Xi_3^{(1257345'7')}\rangle \times \{ \alpha|0011\rangle + \beta|1100\rangle \}_{686'8'} + |\Xi_4^{(1257345'7')}\rangle \{ \alpha|0011\rangle - \beta|1100\rangle \}_{686'8'} \}, \quad (2a)$$

where we introduce the following four-photon mode entangled states

$$|\Xi_1^{(1257345'7')}\rangle = \frac{1}{\sqrt{2}} \{ |11110000\rangle + |00001111\rangle \}_{1257345'7'}, \quad (2b)$$

$$|\Xi_2^{(1257345'7')}\rangle = \frac{1}{\sqrt{2}} \{ |11110000\rangle - |00001111\rangle \}_{1257345'7'}, \quad (2c)$$

$$|\Xi_3^{(1257345'7')}\rangle = \frac{1}{\sqrt{2}} \{ |11000011\rangle + |00111100\rangle \}_{1257345'7'}, \quad (2d)$$

$$|\Xi_4^{(1257345'7')}\rangle = \frac{1}{\sqrt{2}} \{ |11000011\rangle - |00111100\rangle \}_{1257345'7'}. \quad (2e)$$

The states in the modes 6, 8, 6' and 8' is the teleported state while the states $|\Xi_i^{(1257345'7')}\rangle$ ($i = 1-4$) of the ancillary photons must be subjected to the Bell state measurement to end up the teleportation protocol [1]. Straightforward calculations based on the quantum theory of the beam splitter yield the following outcomes of the states (2b)–(2e)

$$|\Xi_1^{(1257345'7')}\rangle \rightarrow \frac{1}{2\sqrt{2}} \{ |22000000\rangle + |00220000\rangle - |20020000\rangle - |02200000\rangle + |00002200\rangle + |00000022\rangle - |00002002\rangle - |00000220\rangle \}_{1257345'7'}, \quad (3a)$$

$$|\Xi_2^{(1257345'7')}\rangle \rightarrow \frac{1}{2\sqrt{2}} \{ |22000000\rangle + |00220000\rangle - |20020000\rangle - |02200000\rangle + |00002200\rangle - |00000022\rangle + |00002002\rangle + |00000220\rangle \}_{1257345'7'}, \quad (3b)$$

$$|\Xi_3^{(1257345'7')}\rangle \rightarrow \frac{1}{2\sqrt{2}} \{ |11001100\rangle + |11000011\rangle + |00111100\rangle + |00110011\rangle - |10011001\rangle \} \quad (3c)$$

$$\begin{aligned}
 & - |10010110\rangle - |01101001\rangle - |011001110\rangle \}_{1257345'7}, \\
 & |\Xi_4^{(1257345'7)}\rangle \longrightarrow -\frac{1}{2\sqrt{2}} \{ |11001001\rangle + |11000110\rangle \\
 & \quad + |00111001\rangle + |00110110\rangle - |10011100\rangle \quad (3d) \\
 & - |10010011\rangle - |01101100\rangle - |01100011\rangle \}_{1257345'7}.
 \end{aligned}$$

We have four different outcomes that can be grouped into two separate groups, namely, first group involves the outcomes characterized by simultaneous clicks in two different detectors (two bits of information Eqs. (3a), (3b)). The states $|\Xi_1^{(1257345'7)}\rangle$ and $|\Xi_2^{(1257345'7)}\rangle$ (first group) result in the outcomes different only by sign from each other. Thus, the teleportation protocol in figure fails when two detectors simultaneously register four photons as the outcomes of the first group (Eqs. (3a), (3b)) are not distinguishable from each other. Unlike the outcomes of the first group, a Bell state measurement of the states of the second group $|\Xi_3^{(1257345'7)}\rangle$ and $|\Xi_4^{(1257345'7)}\rangle$ projects the states on coincidence registration of four photons in four detectors (four bits, Eqs. (3c), (3d)). It is easy to check the outcomes (3c), (3d) are distinguishable from each other. Thus, when two pairs of detectors register a particular combination of four coincidences, Alice knows which state ($|\Xi_3^{(1257345'7)}\rangle$ or $|\Xi_4^{(1257345'7)}\rangle$) correspond to it and, consequently, which state Bob has in his hands and Alice must inform him about it using classical communication [1].

To end up the teleportation protocol, one should define what state is considered to be successfully teleported. Let us consider the quantum teleportation performance to be successful if the following state $\{\alpha|0011\rangle + \beta|1100\rangle\}_{686'8}$ occurs at Bob's station. If Bob is informed about outcome corresponding to the state $|\Xi_3^{(1257345'7)}\rangle$, he must do nothing. Other possible case corresponds to the outcomes following from the input state $|\Xi_4^{(1257345'7)}\rangle$. To restore the teleported state in the case, Bob must apply corresponding unitary transformations in one of the output modes. In our case, it is sufficient to make use of the π -phase shifter, for example, in the mode 6 to restore the teleported state. Since the states forming second group represents one second of the entire initial photon state (2a), the success probability for the entanglement teleportation using the quantum channel (1) is 50% also as in original proposal [1].

One should say some words about a possibility to generate quantum channel (1) for the quantum teleportation. From the "no cloning theorem" [15], we know the conversion $(\alpha|0\rangle + \beta|1\rangle) \longrightarrow (\alpha|0\rangle + \beta|1\rangle)(\alpha|0\rangle + \beta|1\rangle)$ is forbidden while the following operation $(\alpha|0\rangle + \beta|1\rangle) \longrightarrow (\alpha|00\rangle + \beta|11\rangle)$ is allowed. To construct the quantum channel (1), we must make use of a quantum encoder operating on the mode entangled states [13] and whose output in a probabilistic way $(\alpha|00\rangle +$

$\beta|11\rangle) \longrightarrow (\alpha|0000\rangle + \beta|1111\rangle)$ will be given by the state (1) in the case of quantum optics.

In conclusion, we have proposed a method to realize a probabilistic quantum teleportation of two-photon mode entangled state through the four-photon quantum channel (1). This method is based only on a few linear optics elements, namely four balanced beam splitters, eight photodetectors and postselection. The maximum success probability of the teleportation protocol is 50%. To achieve the quantum teleportation protocol, fourfold coincidences are required to be performed that are fully available with the present technology.

REFERENCES

1. C. Bennett, G. Brassard, C. Crepeau, *et al.*, Phys. Rev. Lett. **70**, 1895 (1993).
2. D. Bouwmeester, J. W. Pan, K. Mattle, *et al.*, Nature **390**, 575 (1997); D. Boschi, S. Branca, F. De Martini, *et al.*, Phys. Rev. Lett. **80**, 1121 (1998).
3. L. Vaidman and N. Yoran, Phys. Rev. A **59**, 116 (1999); N. Lutkenhaus, J. Calsamiglia, and K. A. Suominen, Phys. Rev. A **59**, 3295 (1999).
4. Y. H. Kim, S. P. Kulik, and Y. H. Shih, Phys. Rev. Lett. **86**, 1370 (2001).
5. H. W. Lee and J. Kim, Phys. Rev. A **63**, 012305 (2000).
6. E. Lombardi, F. Sciarrino, S. Popescu, and F. De Martini, Phys. Rev. Lett. **88**, 070402 (2002); S. Giacomini, F. Sciarrino, E. Lombardi, and F. De Martini, Phys. Rev. A **66**, 030302(R) (2002); D. Fattal, E. Diamanti, K. Inoue, and Y. Yamamoto, Phys. Rev. Lett. **92**, 037904 (2004).
7. D. M. Greenberger, M. A. Horne, A. Shimony, and A. Zeilinger, Am. J. Phys. **58**, 1131 (1990); N. D. Mermin, Phys. Today **43**, 9 (1990).
8. V. N. Gorvachev and A. I. Trubilko, JETP **91**, 894 (2000); B. S. Shi, Y. K. Jiang, and G. C. Guo, Phys. Lett. A **268**, 161 (2000); K. H. Song and W. J. Zhang, Opt. Commun. **195**, 211 (2001); A. Karlsson and M. Bourennane, Phys. Rev. A **58**, 4394 (1998).
9. M. Ikram, S. Y. Zhu, and S. Zubairy, Phys. Rev. A **62**, 022307 (2000); J. Lee and M. S. Kim, Phys. Rev. Lett. **84**, 4236 (2000); J. Lee, H. Min, and S. D. Oh, Phys. Rev. A **66**, 052318 (2002).
10. H. W. Lee, Phys. Rev. A **64**, 014302 (2001).
11. M. Zukowski, A. Zeilinger, M. A. Horne, and A. K. Ekert, Phys. Rev. Lett. **71**, 4287 (1993); J. W. Pan, D. Bouwmeester, H. Weinfurter, and A. Zeilinger, Phys. Rev. Lett. **80**, 3891 (1998).
12. E. Knill, R. Laflamme, and G. J. Milburn, Nature **409**, 46 (2001); T. C. Ralph, A. G. White, W. J. Munro, and G. J. Milburn, Phys. Rev. A **65**, 012314 (2001); S. A. Podoshvedov, J. Opt. B **6**, 549 (2004).
13. S. A. Podoshvedov, J. W. Noh, and K. S. Kim, Opt. Commun. **232**, 357 (2004).
14. M. Nielsen and I. L. Chuang, *Quantum Computation and Quantum Information* (Cambridge Univ. Press, Cambridge, 2000).
15. W. K. Wootters and W. H. Zurek, Nature **299**, 802 (1982).